Thèse n° 9698

Investigation of thermoelectric nanomaterials

Présentée le 29 août 2023

Faculté des sciences et techniques de l'ingénieur
Groupe SCI STI SM
Programme doctoral en science et génie des matériaux

pour l'obtention du grade de Docteur ès Sciences

par

David Thomas OSENBERG

Acceptée sur proposition du jury

Prof. D. Grundler, président du jury
Dr. S. Mischler, Dr L. V. S. Philippe, directeurs de thèse
Prof. M. M. Rojo, rapporteur
Dr P. Schmutz, rapporteur
Prof. J.-M. Sallese, rapporteur

École
polytechnique
fédérale
de Lausanne

2023

Acknowledgements

In light of the difficulties encountered during the thesis, like COVID restrictions and more significantly sickness and loss of several family members, I first thank God for the physical and mental health required to complete the thesis.

I am also grateful to my PhD supervisors Laetitia Philippe and Stefano Mischler, who always were approachable and helpful and gave me the opportunity to join the group and work in their laboratories. In this regard I also thank Johann Michler for letting me join the laboratory. I appreciate that he together with the EPFL doctoral school allowed me to take leave when it was needed.

Thanks also go to several colleagues from the Electrochemistry group at Empa - as the saying goes, a problem shared is a problem halved.

Finally I am also grateful to several family members for their support. While a PhD thesis is the work of a single person, it can not be accomplished without some level of sacrifice by the people closest.

Abstract

Thermoelectric conversion remains an active research field in light of its potential to enhance energy efficiency by waste heat recovery in a noise and wear-free manner.

Nanostructuring is responsible for most of the recently reported improvements of the figure of merit. Measuring thermoelectric properties of such materials on the microscale is advantageous. But although elaborate microdevices for complete thermoelectric characterization have been fabricated, a demanding transfer of the samples onto these devices is generally required and establishing sufficient electrical contact is challenging in this case. Therefore considerable effort was made first to develop a complete and transfer free in-plane characterization method for samples obtained by deposition processes. The accuracy of the method was verified by numerical studies closely mimicking the actual measurement process, comparison to measurements on simultaneously deposited reference samples and results from literature.

The developed devices were then applied to samples of interest, i.e. thin films, bismuth rich deposits and composition modulated multilayers, resulting in improvements compared to as-deposited bulk samples in some cases. First attempts at fabricating bismuth telluride - polypyrrole multilayers by electrodeposition are also presented. Based on modeling of the electronic properties of multilayers, upon further refinement, improved conversion efficiency in these structures is expected due to quantum confinement effects.

Modeling results of size effects on the lattice thermal conductivity are also discussed and a two-band model describing the bulk electronic properties of bismuth telluride is used to determine the level of doping.

Contents

Acknowledgements i

Abstract ii

List of Figures iv

List of Tables x

1 Introduction 1

1.1 Research goals 2

1.2 Thesis outline 3

2 Literature review 3

2.1 Modeling thermoelectric properties 3

2.1.1 The Callaway model 7

2.1.2 Boundary scattering in thin films 11

2.2 Multilayers 12

2.2.1 Electric properties 12

2.3 Strategies of efficiency enhancement 17

2.4 Nanostructuring 18

2.5 Electrodeposition 21

2.6 Effect of annealing 24

2.7 Measurement techniques 25

3 Materials and methods 33

3.1 Microfabrication of measurement devices 33

3.1.1 First Design 33

3.1.2 Improved Design 35

3.2 Setup and reference sample preparation 40

3.3 Numerical modeling 41

4 Electrochemical deposition and structural analysis of uniform films 43

4.1 Electrodeposition of bismuth telluride 43

4.2 Structural analysis by x-ray diffraction 45

5 Design and improvement of measurement devices for in-plane characterization 49

5.1 Measurement of the thermoelectric properties by self-heating methods 49

5.1.1 Feasibility study of in-plane characterization of supported films 49

5.1.2 Harman-Cahn measurements 53

5.1.3 Cross-plane transport 56

5.2 First attempts on large suspended samples 59

5.3 First application of microdevices 65

5.3.1 Finite element modeling 69

5.3.2 Device validation by measurements 72

5.4 Improvement of measurement devices for thermoelectric characterization . . . 79

5.4.1 FEM modeling of the improved design 80

5.5 Measurement setup 83

5.6 Further modifications for measurement on highly resistive samples 84

6 Towards nanostructured materials 88

6.1 Thermopower of bismuth-rich bismuth telluride 89

6.2 Composition modulated bismuth telluride multilayers 90

6.3 Measurements on thin supported films 93

6.4 Bismuth telluride / polypyrrole multilayers 94

7 Conclusion 99

8 References 100

9 Curriculum Vitae

List of Figures

2.1 Phonon life times based on analytic expressions compared to Rojo et al.'s numerical results (zig-zag lines) for the longitudinal and transverse acoustic branches in the (110) direction. The major difference is the high normal scattering rate derived from the analytic expressions. 9

2.2 Obtained bulk thermal conductivity along the bisectrix and the trigonal directions. 10

2.3 Size dependence of the lattice thermal conductivity together with some experimental results. 11

2.4 Conductivity reduction in thin films assuming diffuse scattering according to the Fuchs-Sondheimer equation. 12

2.5 Density of states in superlattices of varying peridod d and equal well and barrier width, with the well material's conduction band edge as reference. The 3D density of states is also depicted. 14

2.6 The figure of merit is plotted as a function of the Fermi level (relative to the conduction band edge in the well material) (a). For the superlattice equal well and barrier widths of 5 nm were assumed. Figure (b) shows the figure of merit of a free standing film of varying thickness compared to the figure of merit of a superlattice of equal well and barrier width and a conduction band offset or barrier height of 1.7 eV. 16

2.7 The figure of merit in relation to the bulk value is plotted for varying well widths and potential barriers. 17

2.8 Ideal band diagram of a Sb_2Te_3/Bi_2Te_3 superlattice. Red features indicate the ideal band diagram in a $Bi_{2+x}Te_{3-x}$ / Te superlattice. Adapted from [1] . 21

2.9 The expected film thickness is plotted as a function of the binary alloy's composition. 24

3.1 Optical microscope images of the microdevices at different stages of the fabrication process, namely (a) after the first lithography and etching of the exposed metals, two of the notches have been circled, (b) after anisotropic wet etching of the underlying silicon and the second lithography and finally (c) after electroplating into the prepared molds and stripping the photoresist. The final steps are etching of supporting silicon dioxide and exposed metals to obtain free-standing samples. 34

3.2 Excerpt of the final mask layout. 37

3.3 Schematic illustrating the fabrication process of the improved microdevices. . 39

3.4 Photograph of the measurement device. The sample is placed on the indium foil in the center of the sample holder (a) onto which it is pressed by spring loaded clamps (b) to minimize thermal contact resistance between sample holder and die. The radiation shield on the right-hand side is finally placed over the die and screwed on the base plate. 40

3.5 SEM image of a completed microdevice with electrodeposited bismuth telluride (a) together with an image of the finite element model (b). The surface temperature in K is indicated by a color map. SEM images of the nickel (c) and bismuth (d) sample are also displayed. 42

4.1 The composition of the obtained deposits mainly according to XRF is presented as a function of applied potential (a) and current density (b) 43

4.2 Presented are thickness profiles, derived from series of SEM images, of a selection of samples deposited at different potentials, temperatures and in horizontal or vertical electrode configuration. 44

4.3 Texture Harris coefficient of the (110) reflection as a function of the applied current density. The texture coefficient 0 in spite of a large current density was obtained from a sample deposited under forced convection. 46

4.4 Hexagonal lattice parameters obtained from the determined Bragg angles using Bragg's law. (a) shows the a-axis parameter and (b) the c-axis parameter. 47

4.5 The XRD patterns obtained from annealed and as-deposited samples transferred to an electrically insulating substrate (i.e. from the sample's underside) are displayed (a). The Williamson-Hall plots based on XRD patterns of samples transferred to an electrically insulating substrate (b) and untransferred ones (c) both annealed and as deposited. All indices refer to the hexagonal representation of the rhombohedral lattice (based on JCPDS No. 15-0863). 48

5.1 Schematic of one of the considered supported sample configurations (a). Comparison of solutions for the temperature profile based on the analytical model and the finite element method for the case of a 0.5 µm thick and 1 cm long sample supported on a 1 mm thick polymer layer (b) 51

5.2 The average sample temperature increase is plotted as a function of its inverse thermal conductivity. The slope of this line is related to the sensitivity of the method. 52

5.3 (a) Sketch of the setup analyzed by Harman and Cahn. Their results are accurate under the condition that Lead 1 and 2 are thermoelectrically equal. Subscripts c and h represent cold and hot junctions respectively. (b) Exemplary temperature profile that might be observed in case of positive Ss and current direction as in (a), assuming that the leads have a negligible Seebeck coefficient. 54

5.4 (a) Developed measurement setup with a ca. 30 µm thick sample mounted on suspended platinum resistance thermometers. Electrical four point contact to the sample was established by soldering copper wires to the ends. (b) A radiation shield thermally anchored to the heater is designed to avoid the temperature excursions displayed in (c) which are based on FEM results. . . 55

5.5 Sketch of the case encountered experimentally in the cross-plane case. 56

5.6 (a) Thermal resistance model accounting for the non-zero thermal resistance of the substrate. (b) Temperature excursion from the bulk of the substrate as a function of sample diameter 58

5.7 Schematic of proposed cross-plane devices for the measurement of thermoelectric properties (a), the thickness of the sample is exaggerated for clarity. Not shown is the thermometer used to measure the temperature of the top side of the electrode. 59

5.8 Schematic of the measurement setup for samples suspended between PRTs. . 62

5.9 Measured thermal conductance of the wires supporting the left and right half of the wires supporting the suspended setup, according to the superscripts, and the thermal conductance of the sample. 63

5.10 a) The measured temperatures and sample resistance as a function of the alternating current applied through the sample. b) The transient response of the system, i.e. again temperatures and voltage, after interrupting the DC-current are plotted. The voltage is related to the temperature by the Seebeck effect, c) The second method of measuring the thermopower is to us one of the PRTs as a heater and measure the induced voltage along the sample (the open circuit potential). 64

5.11 a) The measured electrical conductivity is plotted as a function of the substrate temperature. b) The thermopower as a function of temperature by both of the measurement methods. c) The determined thermal conductivity as a function of temperature with and without correction for radiation flux. d) The obtained figure of merit. 65

5.12 Schematic of the device for the in-plane measurement of thermoelectric properties (a). The inset is a close-up of a cross-section view of the supported central electrode. (b) Equivalent circuit of the device modeling the electrical properties including the voltage sources. The heating current source is assumed to be isolated from ground. 66

5.13 The computed sample resistance as a function of the applied power including the line of best fit (a). From the slope and sample dimensions the thermal conductivity can be obtained, the relative error is plotted as a function of oxide and metal film thickness (b). The relative error of the measured resistivity is displayed again as a function of oxide and metal film thickness (c). 70

5.14 Relative error of the thermopower as a function of metal and oxide film thickness (a). Relative deviation of the determined temperature excursion from the average temperature excursion of the supported segment (b). 71

5.15 Relative error of the thermal conductivity measurement (crosses) and the thermopower measurement (circles) as a function of the sample's thermal and electrical conductance. The dashed black curve connects points for which thermal and electrical conductance are coupled and thus provides an estimate of the film thickness dependence of the error. 72

5.16 Plot of the measurement results of all thermoelectric properties. 77

5.17 The Seebeck coefficient, Lorenz number and electrical resistivity are computed for bismuth telluride as a function of the Fermi level based on a two-band effective mass model, as described in Section 2.1. 78

5.18 As in case of the original design the relative errors of the thermoelectric properties and the temperature difference, (a) to (d), are determined as a function of certain design parameters, namely the width of the electrodes and the thickness of the underlying oxide, by FEM. A graphical representation of one solution indicating temperature by a color map is also shown (e). 82

5.19 Schematic of the measurement setup, except for the temperature control system. The NI 9263 and NI 9219 out- and input modules are used to carry out pseudo-4-point measurements, while the function generator is used to apply heating current to the electrodes. The electromechanical relay allows selecting which electrode is heated. 86

5.20 Equivalent circuit representing a part of the devices before contact to the substrate of the electrodes was eliminated (a). Resistor R_s represents the sample. (b) is a micrograph of the devices before the discussed design modification. The gold layer covers the entire through-holes. Figure (c) is a micrograph of the templates after the design was changed. After this change back side etching completely isolates the electrodes from each other. Earlier gold bridges remained at the edges of the through-holes that had to be broken manually. 87

6.1 SEM image of the nickel sample used to verify the measurement method (a). The measurement results are compared to literature, taken from [2]. 89

6.2 Measured Seebeck coefficient of the bismuth rich sample. 90

6.3 Example of an SEM cross section of an electrodeposited multilayered reference sample (a). The layered structure is revealed by a contrast in the secondary electron signal. 91

6.4 The Seebeck coefficient (a) resistivity (b) and thermal conductivity (c) of a multilayer. 92

6.5 Micrograph of a supported Bi_2Te_3 thin film (a). The measured thermopower is displayed in (b). 94

6.6 Band diagram around a bismuth telluride / polypyrrole heterojunction, taken from [3]. 95
6.7 Cyclic voltamograms in aqueous solutions of pyrrole at varying concentration of hydroquinone (a). The voltamograms in the bismuth telluride bath and in an electrolyte with added pyrrole and hydroquinone. 96
6.8 The deposition potential applied and the current during electroplating of bismuth telluride / polypyrrole multilayers (a). The deposition steps are charge controlled (b). (c) and (d) are SEM images of the obtained deposits. . 98
6.9 Wide shot SEM image (a) of a multilayer from a pyrrole and Bi(III), Te(IV) containing electrolyte and the corresponding close-up (b). 99

List of Tables

2.1 Overview of different methods used to measure the thermal conductivity. . . 28

1 Introduction

Based on the second law of thermodynamics most processes produce a significant amount of waste heat. Converting this heat directly to electrical energy enhances the efficiency of these processes with the benefit of not creating additional noise and wear since moving parts are not required. The direct conversion to electrical energy requires that a temperature gradient gives rise to a gradient of the electrical potential. This is the case in most conductors since charge carriers can be thermally excited. The converse effect that electrical currents contribute to the heat transfer can be used for refrigeration, which can be applied for instance to the thermal management of circuits, which is becoming more important in light of the progressing miniaturization and thus increasing power density in electronic components.

The coefficient of performance or efficiency is defined as the ratio of extracted power to the expenditure of energy. In case of thermoelectric generators the extracted power is the power delivered to the load, in case of refrigerators it is the heat flux from the source. In both cases it can be shown that the maximum efficiency depends only on the temperature of the reservoirs and the dimensionless figure of merit, $zT_\mathrm{m} = \frac{S^2\sigma}{\kappa}T_\mathrm{m}$. Here S is the thermopower or Seebeck coefficient, σ the electrical conductivity, κ the thermal conductivity and T_m the mean temperature. The maximum efficiency monotonically increases with the figure of merit and reaches the Carnot efficiency in the limit $zT_\mathrm{m} \to \infty$. This explains why research in thermoelectric conversion revolves around the problem of enhancing the thermoelectric figure of merit. The figure of merit is intuitive: The Seebeck coefficient determines the magnitude of the electromotive force and with decreasing electrical conductivity an increasing amount of the obtained power would be converted to heat again (Joule heating) and thus both quantities have to be maximized. The thermal conductivity κ, which is the conductivity when no electrical current is flowing, on the other hand causes conduction of heat without conversion and thus has to be minimized. Maximizing the figure of merit is challenging. The thermopower of a material depends on the asymmetry of the differential electrical conductivity around the Fermi level. The asymmetry of the differential conductivity is mainly controlled by the density of states. In metals the Fermi level is usually far from the band edge, and thus the change in the density of states within the interval $k_\mathrm{B}T$ around the Fermi level is small, leading to a nearly constant differential conductivity in this interval. This explains why the thermopower of most metals is on the order of microvolts per Kelvin

only.

In semiconductors the Fermi level can be close to the band edge, which means that the change in the density of states in an interval $k_\mathrm{B}T$ around the Fermi level can be significant, leading to a high thermopower on the order of $100\,\mu\mathrm{V/K}$. This is why in the solid state only semiconductors or semimetals are considered as thermoelectric generators. However as the Fermi level moves into the band gap the electrical conductivity drops, and thus maximizing the so called power factor $S^2\sigma$, where S denotes the Seebeck coefficient and σ the electrical conductivity, is a trade-off. The maximum is typically attained when the Fermi level is about $k_\mathrm{B}T$ from the band edge inside the respectice band. The thermal conductivity is composed of contributions from the charge carriers and the crystal lattice, $\kappa = \kappa_e + \kappa_l$. The electric contribution increases with the carrier concentration and thus with the electrical conductivity. In fact metals obey the Wiedemann-Franz law which states that $\kappa_e = L_0\sigma T$, where L_0, the Lorentz number, equals $2.44 \cdot 10^{-8}\,\mathrm{W\Omega K^{-2}}$. Degenerate semiconductors also obey this law. Thus the electronic contribution cannot be decreased without affecting σ. There is however the potential to decrease the phononic contribution to κ without as much impact on the charge carriers, as explained below. The electronic properties are mainly governed by the density of states, which provides additional opportunities of enhancing thermoelectric properties such as band structure engineering and nanostructuring.

1.1 Research goals

As will be discussed, material improvements by nanostructuring have mostly been due to suppression of the lattice thermal conductivity, but these are limited. Significant improvements by additional exploitation of quantum confinement effects have been predicted but rarely demonstrated. Moreover obtaining a compact material that could be more easily integrated into a device than nanowires for instance is desirable. Electroplating is cost-effective and energy-efficient relative to other fabrication methods and nanostructured deposits, in particular multilayers, can be obtained even without templates by modulating process parameters such as the deposition potential.

Therefore the scientific objectives are firstly to understand the relevant size effects for the material of choice, namely bismuth telluride, which is of interest due to already good thermoelectric properties near room temperature in the bulk. This should provide insight

into the miniaturization requirements. Secondly, to master the electrodeposition of bulk and then micro-structured thermoelectric materials and simultaneously to develop an accurate and reliable thermoelectric characterization method tailored to deposited materials, which, as will be pointed out, is lacking. The latter is a prerequisite to materials engineering. Measuring the thermoelectric properties and the thermal conductivity in particular can be challenging. This is especially true when samples obtained by deposition processes on the micro-scale are considered, to which conventional methods are not applicable.

1.2 Thesis outline

Thus much effort was first made to develop an accurate and reliable characterization method, these efforts are outlined in Chapter 5. An overview of the potential improvements by nanostructuring is given in Chapter 2, including specifically reduction of the thermal conductivity, Subsection 2.1, and increase of the power factor in multilayers, Subsection 2.2. The other available measurement methods are discussed in Subsection 2.7, explaining why a method tailored to deposited samples is desirable. Fabrication of the microdevices is described in Chapter 3. The application of these devices to modified materials is discussed in Chapter 6.

2 Literature review

2.1 Modeling thermoelectric properties

The equilibrium distributions of charge carriers obeying Fermi-Dirac statistics and phonons obeying Bose-Einstein statistics can be derived from statistical thermodynamics. Net transport of energy or matter however requires departure from the equilibrium state and thus the question of modeling transport in systems which have been perturbed from equilibrium arises. A commonly used technique is the Boltzmann transport equation (BTE) describing the non-equilibrium distribution of classical particles under application of external forces or other imposed gradients. The statistical nature of this approach is its main advantage over other methods like molecular dynamics, since the amount of particles to be accounted for is on the order of the number of atoms involved. While numerical methods have been applied, analytical solution is possible under certain simplifying

conditions.

It should be noted that the BTE is derived from classical physics, however modifications accounting for quantum mechanical effects can be made, for instance by assuming non-classical equilibrium distributions or adapting the density of states to even consider quantum confinement. Effects that can not easily be accounted for are those due to the wave nature of the particles, like interference and tunneling. Thus one of the criteria for applying the BTE is for the characteristic length scale to be significantly greater than the coherence length of the particles or interfaces to be rough, which introduce coherence destroying randomness.

The BTE reads $\frac{\partial f}{\partial t} + \mathbf{v}\nabla_{\mathbf{r}} f + \frac{\mathbf{F}}{m}\nabla_{\mathbf{v}} f = \left(\frac{\partial f}{\partial t}\right)_c$, where the right-hand side is a scattering term. Complex integral expressions for the scattering term can be derived for the respective scattering processes, but the resulting integral-differential equation is difficult to solve. Thus the scattering integral is typically approximated by a term proportional to the deviation of the distribution function from the equilibrium distribution f_0. In this so called relaxation time approximation the BTE reads $\frac{\partial f}{\partial t} + \mathbf{v}\nabla_{\mathbf{r}} f + \frac{\mathbf{F}}{m}\nabla_{\mathbf{v}} f = -\frac{f-f_0}{\tau(\mathbf{r},\mathbf{v})}$.

Defining the deviation function $g = f - f_0$, the BTE can be reformulated as $\frac{\partial g}{\partial t} + \frac{\partial f_0}{\partial t} + \mathbf{v}\nabla_{\mathbf{r}} g + \mathbf{v}\nabla_{\mathbf{r}} f_0 + \frac{\mathbf{F}}{m}\nabla_{\mathbf{v}} g + \frac{\mathbf{F}}{m}\nabla_{\mathbf{v}} f_0 = -\frac{g}{\tau}$. In order to derive transport laws in absence of size or interface dependent scattering, the BTE can be further simplified by ignoring the time dependence and assuming that the derivatives of g are negligible compared to those of f_0 [4], i.e.

$$g = -\tau(\mathbf{v}\nabla_{\mathbf{r}} f_0 + \frac{\mathbf{F}}{m}\nabla_{\mathbf{v}} f_0). \tag{1}$$

Once the non-equilibrium distribution function has been determined, the flux (heat flux, current density etc.) can be obtained by integration over the phase space. The electrical current density is for instance given by $j_e = -e\int_0^\infty v_x D(E) g \mathrm{d}E$.

In the case of charge carriers the equilibrium distribution function is the Fermi-Dirac distribution, $f_0 = (\exp(\frac{E-E_f}{k_B T}) + 1)^{-1}$. Because $\frac{\partial f_0}{\partial T} = -\frac{E-E_f}{T}\frac{\partial f_0}{\partial E}$ and $\frac{\partial f_0}{\partial E_f} = -\frac{\partial f_0}{\partial E}$, $\frac{\partial f_0}{\partial x} = \frac{\partial f_0}{\partial T}\frac{\partial T}{\partial x} + \frac{\partial f_0}{\partial E}\frac{\partial (E-E_f)}{\partial x} = \frac{\partial f_0}{\partial E}(\frac{\partial (E-E_f)}{\partial x} - \frac{E-E_f}{T}\frac{\partial T}{\partial x})$ and $\frac{\partial f_0}{\partial v_x} = m v_x \frac{\partial f_0}{\partial E}$. The current density is then computed by inserting in the equation for the current density, $j_e = -e\int v_x^2 \tau(\frac{\partial (E_f - E)}{\partial x} + \frac{E-E_f}{T}\frac{\partial T}{\partial x} + eE_x)\frac{\partial f_0}{\partial E} D(E)\mathrm{d}E = -\frac{e^2}{3}\int v^2\tau(-\frac{\partial \Phi}{\partial x} + \frac{E-E_f}{eT}\frac{\partial T}{\partial x})\frac{\partial f_0}{\partial E} D(E)\mathrm{d}E$, where Φ is the electrochemical potential which is the sum of the electrostatic and chemical potential and the factor $1/3$ stems from averaging v_x^2 over a unit sphere assuming isotropic motion. When

no temperature gradient is present, $j_e = -\sigma \frac{\partial \Phi}{\partial x}$ and thus $\sigma = -\frac{e^2}{3} \int v^2 \tau \frac{\partial f_0}{\partial E} D(E) \mathrm{d}E$. When no current is flowing, the Seebeck coefficient $S = \frac{-\partial \Phi / \partial x}{\partial T / \partial x}$ and thus $S = \frac{e}{3T} \int v^2 \tau (E - E_f) \partial_E f_0 D(E) \mathrm{d}E / \sigma$ [4]. The magnitude of this expression depends on the asymmetry of $v^2 \tau D(E)$ around the Fermi level. This explains why degenerate semiconductors and metals tend to have small Seebeck coefficients on the order of µV/K, as as the slope of the density of states is $\propto \sqrt{E}^{-1}$ and therefore decreases for energies further in the band. It also illustrates why nanostructuring can improve the Seebeck coefficient, as it introduces discontinuities in the density of states, provided the Fermi level can be adapted to be within $k_B T$ of these features.

The lattice thermal conductivity is obtained by a similar approach, where $g = -\tau v_x \frac{\partial f_0}{\partial x} = -\tau v_x \frac{\partial f_0}{\partial T} \frac{\partial T}{\partial x}$ is used. From the displaced distribution the heat flux can be obtained as $-\frac{dT}{dx} \int_0^{\omega_{max}} v^2 \tau \frac{df_0}{dT} \hbar \omega D(\omega) \mathrm{d}\omega / 3$, where the factor 1/3 as above stems from averaging v_x^2. Often the phonon group velocity $d\omega/dk$ is assumed to be constant, i.e. a linear dispersion is assumed which is accurate for acoustic phonon branches close to the origin of the Brillouin zone. In contrast to the case of charge carriers the integration has to be limited for phonons. In case of charge carriers the integral is limited by the derivative of the Fermi-Dirac distribution. Phonons generally carry by orders of magnitude lower energy than electrons. Thus the distribution function for the phonons, which approximates the one for fermions above the Fermi level, can be significantly greater than zero for phonons of all energies at room temperature, while this is true only for a limited window in case of the charge carriers.

In case parabolic approximation of valence and conductance band edges is feasible, i.e. the effective mass approximation, which is the case for many bulk semiconductors, the thermoelectric properties can be further simplified. It can be easily shown that the density of states in this case is $D(E) = \frac{8\sqrt{2}\pi m^{1.5}}{h^3} \sqrt{E - E_c}$ for the conduction band and likewise for the valence band, where m is the effective mass. Assuming that the relaxation time is $\tau_0 (E - E_c)^{-0.5}$, which is usually the case when acoustic phonon scattering is dominant, the conductivity due to electrons can be expressed as $\sigma_n = \frac{16\sqrt{2}\pi e^2}{3h^3} \sqrt{m_n} \tau_{0,n} k_B T F_0(\eta_n)$, where $F_k(\eta) = \int_0^\infty \xi^k (\exp(\xi - \eta) + 1)^{-1} \mathrm{d}\xi$ and η_n is the reduced Fermi level, i.e. $E_f/(k_B T)$ with E_f relative to the conduction band edge. The expression can be derived from the equation above by integration by parts. The expression for holes is similar, i.e. $\sigma_p = \frac{16\sqrt{2}\pi e^2}{3h^3} \sqrt{m_p} \tau_{0,p} k_B T F_0(\eta_p)$, where $\eta_p = -(\eta_n + \frac{E_g}{k_B T})$ and E_g the band gap at temperature T. Again by integration by parts the expression for the Seebeck coefficient can be evaluated,

$S_n = -\frac{k_B}{e}(\frac{2F_1(\eta_n)}{F_0(n_n)} - \eta_n)$, and similarly for holes [5]. The complete electrical conductivity and Seebeck coefficient are then $\sigma = \sigma_n + \sigma_p$ and $S = \frac{S_n\sigma_n + S_p\sigma_p}{\sigma_n + \sigma_p}$ respectively. The final important electronic property is the Lorenz number L, where LT is equal to the ratio of electronic thermal and electrical conductivity. In case of metals and degenerate semiconductors it is usually equal to $\frac{\pi^2 k_B^2}{3e^2}$. Generally it can be expressed as $L = L_n + L_p + L_{pn} = \frac{\kappa_n + \kappa_p + \kappa_{np}}{\sigma T}$. Here κ_n and κ_p denote heat conduction by charge carriers even in absence of the Peltier effect, by diffusion of hot carriers. The term κ_{np} on the other hand depends on the Peltier effect and requires both types of charge carriers to contribute and is thus referred to as the bipolar contribution:

When a temperature gradient is applied to a thermoelectric material under open circuit conditions, an electrical current induced by the Peltier effect is soon prevented by a potential difference, which is precisely the thermovoltage. A current of electrons and holes can however flow without violating the open circuit condition, i.e. the net current remains zero. This can occur in a narrow band gap material. On the heated side electron hole pairs are generated by thermal excitation. These are driven towards the cold side by the Peltier effect where they recombine, transferring their excitation energy in addition to their excess kinetic energy to the lattice. The contribution to heat transfer can be quantified by treating the contributions of holes and electrons to the transport properties separately. From $j_{n,p} = -\sigma_{n,p}(\partial_x V + S_{n,p}\partial_x T)$ and by imposing the open circuit condition $j_n + j_p = 0$ one obtains $j_n(\frac{1}{\sigma_n} + \frac{1}{\sigma_p}) = \frac{j_n}{\sigma_n} - \frac{j_p}{\sigma_p} = (-S_n + S_p)\partial_x T$. Then the total heat current again under the open circuit condition $h_n + h_p = (S_p - S_n)Tj_n - (\kappa_n + \kappa_p)\partial_x T$ and from this by inserting $\kappa_e = -\frac{h_n + h_p}{\partial_x T} = \kappa_n + \kappa_p + \frac{\sigma_n\sigma_p}{\sigma_n + \sigma_p}(S_p - S_n)^2 T$, where again κ_e is the complete electronic contribution to the thermal conductivity [5]. The last term is similar to the contribution to the thermal conductivity due to the Peltier effect under the zero field or short circuit condition, i.e. $\sigma S^2 T$. The contribution above is indeed due to the Peltier effect, but in this case it is present even under the open circuit condition as the presence of both types of carriers ensures zero net current. If any of the charge carrier contributions is insignificant so is the bipolar contribution. In the case of intrinsic conduction the magnitude of the bipolar contribution can be estimated by approximating the thermopower. This can be achieved by approximating the Fermi-Dirac distribution by the Maxwell-Boltzmann distribution, which is appropriate when $E - E_f \gg k_B T$. Further assuming again that scattering of charge carriers by acoustic phonons is dominant, the thermopower evaluates to $S_{n,p} = \frac{k_B}{e}(\frac{E_f - E_{c,v}}{k_B T} \mp$

2), and thus $S_p - S_n = \frac{k_B}{e}(\frac{E_g}{k_B T} + 4)$. The Lorenz number in the intrinsic case and ignoring bipolar conduction is equal to $2(\frac{k_B}{e})^2$ instead of $\frac{\pi^2}{3}(\frac{k_B}{e})^2$ in the degenerate case. The ratio of the complete electronic thermal conductivity to the normal electronic conductivity, $\kappa_e/\kappa_{e,norm}$, can then be evaluated considering that $\kappa_{e,norm} = LT(\sigma_n+\sigma_p)$, namely $\frac{\kappa_e}{\kappa_{e,norm}} = \frac{LT(\sigma_n+\sigma_p)+\frac{\sigma_n\sigma_p}{\sigma_n+\sigma_p}(S_p-S_n)^2T}{LT(\sigma_n+\sigma_p)} = 1 + \frac{(S_p-S_n)^2T}{4LT} = 1 + \frac{1}{8}(\frac{E_g}{k_B T} + 4)^2$, where additionally $\sigma_n = \sigma_p$ was assumed. Considering that the band gap of bismuth telluride is 0.13 eV, $\frac{\kappa_e}{\kappa_{e,norm}} \approx 11.2$ at 300 K and still 8.0 at 400 K, revealing that the effect of bipolar heat conduction has to be considered when nearly intrinsic samples are investigated. The electronic contribution is usually more substantial at elevated temperatures as both hole and electron density increase with temperature and the Fermi level shifts further into the band gap.

Thus Seebeck coefficient and Lorenz number can be modeled as a function of Fermi level provided the band gap and the mobility and effective mass ratios of the material are known. In the degenerate case the Seebeck coefficient and the Lorenz number are only functions of the reduced Fermi level. In the vicinity of the band gap these properties also depend on the ratio of electron to hole conduction. This in turn is equal to $\frac{\mu_p}{\mu_n}(\frac{m_p}{m_n})^{1.5}\frac{F_{0.5}(\eta_p)}{F_{0.5}(\eta_n)}$.

2.1.1 The Callaway model

As mentioned above the thermal conductivity of semiconductors has contributions from lattice vibrations and the charge carriers. It is important to understand how nanostructuring impacts the former. A starting point for modeling the thermal conductivity is the well known Debye model. It can be derived from the steady state Boltzmann transport equation in the relaxation time approximation, which, as stated above reads $f - f_0 = -\tau_r v_x \frac{\partial f_0}{\partial T}\frac{\partial T}{\partial x}$, where τ_r is the phonon scattering relaxation time for all resistive processes, i.e. Umklapp scattering, isotope or impurity scattering and boundary scattering. Assuming independence, the scattering rates are typically added according to Mathiessen's rule. There is an other type of scattering process not yet considered, which is normal scattering. In such processes the crystal momentum is conserved and thus they cannot be assumed to contribute to the relaxation to the equilibrium Planck distribution. Instead the Callaway model assumes that these processes lead to relaxation to a displaced phonon distribution $f(\vec{\lambda})$, thus $\frac{f-f_0}{\tau_r} + \frac{f-f(\vec{\lambda})}{\tau_N} = -v_x\frac{\partial f_0}{\partial T}\frac{\partial T}{\partial x}$.

Then with Debye's approximations of neglecting the optical branches, isotropy and a constant group velocity, i.e. a linear dispersion, one arrives at the following expression for

the lattice thermal conductivity [6]:

$$\kappa = \frac{k_B}{2\pi^2 v_g}\left(\frac{k_B T}{\hbar}\right)^3 \left[\int_0^{\theta_D/T} \tau_c \frac{x^4 e^x}{(e^x-1)^2}\mathrm{d}x + \frac{\left(\int_0^{\theta_D/T} \frac{\tau_c}{\tau_N}\frac{x^4 e^x}{(e^x-1)^2}\mathrm{d}x\right)^2}{\int_0^{\theta_D/T} \frac{\tau_c}{\tau_N \tau_r}\frac{x^4 e^x}{(e^x-1)^2}\mathrm{d}x}\right], \tag{2}$$

where $\tau_c^{-1} = \tau_r^{-1} + \tau_N^{-1}$. If one assumes $\tau_N^{-1} \to 0$ one obtains Debye's expression for the thermal conductivity, which is the first term in the expression above except with τ_r instead of τ_c. Thus the second integral term is sometimes referred to as a correction. Following Morelli and Heremans [7] one can make the additional assumptions that the Debye temperature and the scattering rates depend on the phonon mode and thus $\kappa = \frac{1}{3}(\kappa_L + 2\kappa_T)$. Analytic expressions for all scattering rates were derived dependent mainly on the Debye temperature, the Grüneisen parameter, the phonon group velocity, the mean atomic mass, the mean atomic volume and the mass-fluctuation scattering parameter. The latter accounts for isolated defects differing in mass from the host atoms. The two most uncertain parameters in this list are the Grüneisen parameter and the Debye temperature and thus often used as fit parameters. The former can depend on the frequency and in case of the latter it would be incorrect to use the value derived from the specific heat, since this includes contributions from all phonon branches. Following Morelli one can derive the Debye temperature in this context from the maximum phonon frequency at the Brillouin zone boundary through $\theta_D = \hbar\omega_{max}/k_B$.

The boundary scattering rate is assumed to be proportional to v/d, where d is a characteristic length, and thus assumed to be independent of phonon frequency. In case of nanowires τ_b^{-1} is actually equal to v/D, where D is the nanowire diameter, assuming diffuse scattering. In case of thin films the boundary scattering rate for a film of equal thickness is smaller, as expected. There seems to be uncertainty with regard to the correct expression for boundary scattering in case of thin films but typically a value around $v/(2.5h)$ is used, where h is the film thickness. The boundary scattering term is questionable in any case, since it affects all phonons, not just those near the boundaries. A more rigorous approach is to compute Sondheimer's conductivity reduction function for each phonon mode and include the modified relaxation time in Equation (2), however in general the deviation to simply applying Mathiessen's rule is small 2.1.2.

The relaxation times obtained by the above mentioned analytic expressions can be

compared to those computed by Rojo et al. [8] based on first principles calculations of the interatomic force constants.

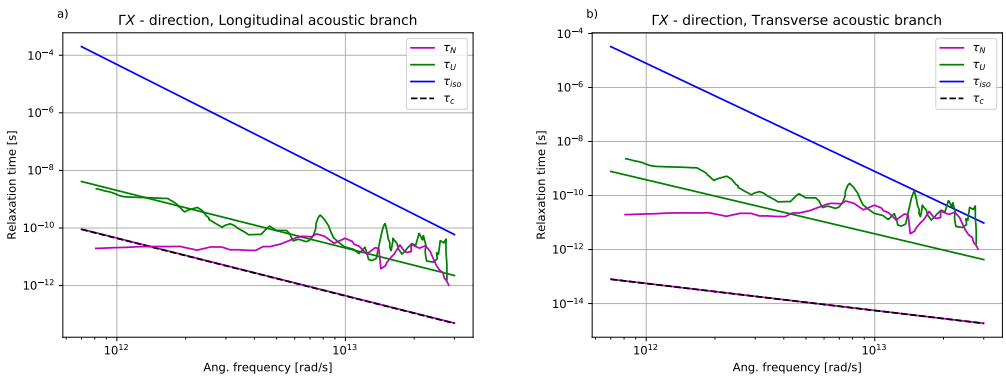

Figure 2.1: Phonon life times based on analytic expressions compared to Rojo et al.'s numerical results (zig-zag lines) for the longitudinal and transverse acoustic branches in the (110) direction. The major difference is the high normal scattering rate derived from the analytic expressions.

While the analytic expression for Umklapp scattering apparently agrees well with the numerical result at least for the longitudinal acoustic (LA) branch, the normal scattering rate is much greater than the one based on the numerical result. The impurity scattering rate is based on isotope abundances, however impurity densities greater than this can be expected due to the process. Stocheometric deviations can possibly also be modeled by assuming higher impurity scattering rates.

In any case the analytical results indicate that normal scattering processes dominate all others for all wavelengths and the numerical results at least confirm that they contribute significantly, especially for long wavelengths. This means that the second integral term in Equation (2) cannot be ignored.

Figure 2.2 displays the obtained bulk thermal conductivities in both the binary and the trigonal (perpendicular to basal plane, ΓZ-direction) direction. While the thermal conductivity in the binary direction agrees well with most reported experimental values (about $1.7\,\mathrm{Wm^{-1}K^{-1}}$at 300 K), the conductivity in the trigonal direction is slightly underestimated (around $0.6\,\mathrm{Wm^{-1}K^{-1}}$ at 300 K)

The model can finally be used to compute the size dependence which enters the expression for the thermal conductivity (Equation (3)) in the form of boundary scattering. As mentioned above this is not the only size effect that affects the thermal conductivity.

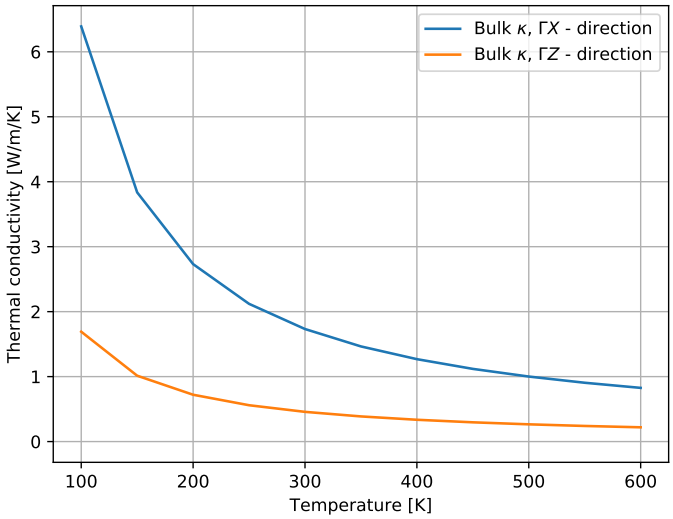

Figure 2.2: Obtained bulk thermal conductivity along the bisectrix and the trigonal directions.

Once the characteristic length approaches the lattice parameters, changes in the phonon dispersion have to be accounted for.

Based on Figure 2.3 achieving a decrease of the thermal conductivity by 50% requires nanowires of diameters about 40 nm in the ΓX- direction. This size dependence is much weaker than the one Rojo et al. predict. According to their modeling diameters about 160 nm would suffice. Most other reported modeling efforts seem to indicate a weaker size dependence.

It should be noted that while temperature and size dependence of the bismuth telluride's lattice thermal conductivity are apparently replicated well by the model due to Morelli and Heremans described above, the mean free path is overpredicted by an order of magnitude. The mean free path at room temperature should be around 1 nm [9, 10] and therefore the model needs to be applied with caution.

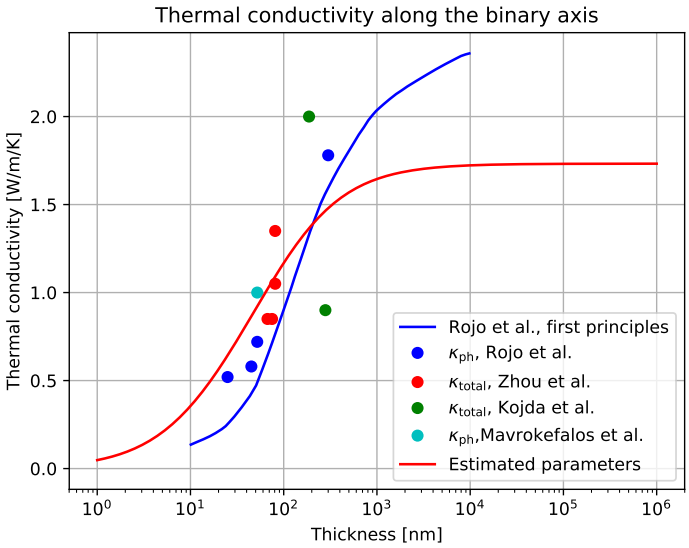

Figure 2.3: Size dependence of the lattice thermal conductivity together with some experimental results.

2.1.2 Boundary scattering in thin films

In case scattering at boundaries has to be accounted for, ignoring the derivatives of g would be incorrect. Considering the case of a thin film normal to the y-axis and a temperature gradient along the x-axis, without loss of generality, the BTE would read $v_x \partial_x f_0 + v_y \partial_y g + F_x/m \partial_{v_x} f_0 = -g/\tau$. The challenge in solving this equation is determining the boundary condition. One can distinguish specular reflection, which occurs when the boundary is smooth in comparison to the carrier wavelengths, and diffuse scattering in case of a rough interface. In case of free standing films the former preserves the momentum and energy of the carriers and thus it can be shown that the conductivity does not deviate from that of the bulk material's. Resistance is however introduced by random scattering at diffuse interfaces. The specularity parameter p, which is the fraction of specularly reflected carriers, has been introduced to describe transport at intermediates to the limiting cases $p = 0$ (diffuse scattering) and $p = 1$ (specular scattering). When the so called gray medium approximation is applied, i.e. the mean free path Λ is energy independent, one arrives at the Fuchs-Sondheimer solution [4]. The conductivity reduction assuming diffuse scattering is plotted below.

The linearized version of this equation has been used to experimentally determine the

electron mean free path in bismuth telluride. The equation reads $\rho_f = \rho_g(1 + \frac{3}{8}(1-p)\frac{\Lambda_g}{t})$ [11], where t is the film thickness and ρ_g and Λ_g are the resistivity and mean free path in an infinitely thick film of equivalent grain size. Several authors then derive the mean free path Λ_g from the slope of the thickness dependent resistivity, finding large mean free paths greater than 500 nm at room temperature. The problem with this approach is the assumption that the microstructure of each thin film is the same, which is very unlikely. Based on estimates from the measured mobility and Seebeck coefficient values between 21 and 60 nm are estimated ([10] and supporting information of [12]).

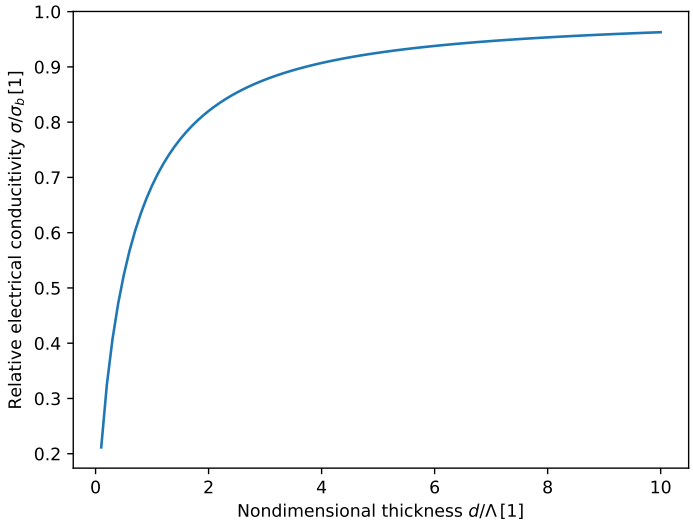

Figure 2.4: Conductivity reduction in thin films assuming diffuse scattering according to the Fuchs-Sondheimer equation.

2.2 Multilayers

2.2.1 Electric properties

While phonon scattering at interfaces in layered structures tends to improve thermoelectric performance, scattering of charge carriers at interfaces can negatively impact the electrical conductivity and thermopower. Apart from these classical size effects however electronic properties can be positively affected by quantum size effects, as quantum confinement can cause a deviation from the 3D band structure. Hicks and Dresselhaus first discussed this effect for free standing thin bismuth telluride films [13], i.e. in other words for quantum

well structures with infinitely high potential barriers, finding that the figure of merit increases monotonically with decreasing film thickness, exceeding the bulk value below about 9 nm. Device integration of thin films is however not straightforward, a more feasible implementation are layered structures with finite band offsets. To gain understanding of the electronic properties of these structures the so called effective mass approximation can be applied, in which charge carriers in the periodic crystal potential are described as free carriers of a particular effective mass. The treatment as free particles clearly simplifies computing the effects of long range perturbations to the potential, as observed in a superlattice. Further simplification by ignoring coupling between multiple bands yields Kronig-Penney type models. In the simplest case effective mass differences, lattice constant offests (and therefore strain effects), work function offsets causing band bending due to charge transfer between the layers and the non-parabolicity of the bands are ignored. Particularly the latter is problematic in case of large conduction band offsets discussed in the following since parabolicity and thereby the assumption of constant effective mass is only valid close to the band edge. Also in case of indirect band gap semiconductors like Bi_2Te_3 the valley degeneracies are partially lifted by quantum confinement, as its effect on the bands depends on the effective mass, which in case of Bi_2Te_3 is anisotropic. This implies that the electrical transport properties could be overestimated when multiplied by the bulk valley degeneracy ($N_v = 6$).

In any case the oversimplified Kronig-Penney model can provide some qualitative understanding on the size dependence, and will therefore be discussed in the following. The time independent Schrödinger equation is solved in the well (ψ_1, width a) and barrier domain (ψ_2, width b). Continuity of the wave function and its derivative provides two boundary conditions. Applying Bloch's theorem for periodic potentials produces $\psi_3(z) = \psi_1(z-d)e^{ik_z d}$, where $d = a + b$ is the superlattice period, based on which two more boundary conditions complete a set of linear equations, which gives rise to the dispersion relation: $k_z = d^{-1} \arccos\left(\frac{k_{2i}^2 - k_1^2}{2k_1 k_{2i}} \sinh(k_{2i}b)\sin(k_1 a) + \cosh(k_{2i}b)\cos(k_1 a)\right)$, where $k_1 = \hbar^{-1}\sqrt{2m^* E_z}$ and $k_{2i} = \hbar^{-1}\sqrt{2m^*(V - E_z)}$, where V is the conduction band offset. Solutions only exist for certain energies and therefore minibands arise. The 3D density of states can then be computed as $D(E) = \frac{1}{4\pi^3}\sum_m \int\int \delta(E - E_{z,m}(k_z) - \frac{\hbar^2 k_\perp^2}{2m^*})\mathrm{d}^2 k_\perp \mathrm{d}k_z$, where $k_\perp$ denotes the wave vector in lattice planes and the summation is over all minibands

below or containing E. Then changing to polar coordinates

$$
\begin{aligned}
D(E) &= \frac{1}{2\pi^2} \sum_{m=1}^{n} \int\int \delta(E - E_{z,m}(k_z) - \frac{\hbar^2 k_\perp^2}{2m^*}) k_\perp \mathrm{d}k_\perp \mathrm{d}k_z \\
&= \frac{m^*}{2\pi^2\hbar^2} \sum_{m=1}^{n} \int\int \frac{\delta(k_\perp - \sqrt{\frac{2m^*}{\hbar^2}(E - E_{z,m}(k_z))})}{\sqrt{\frac{2m^*}{\hbar^2}(E - E_{z,m}(k_z))}} k_\perp \mathrm{d}k_\perp \mathrm{d}k_z \\
&= \frac{m^*}{2\pi^2\hbar^2} \left(\int_{-k_z(E)}^{k_z(E)} \mathrm{d}k_z + (n-1)\frac{2\pi}{d} \right) \\
&= \frac{m^*}{\pi^2\hbar^2} k_z(E) + (n-1)\frac{\pi}{d}.
\end{aligned}
$$

This allows plotting the density of states for the example of equal barrier and well width together with the 3D density of states for comparison, cf. Figure 2.5.

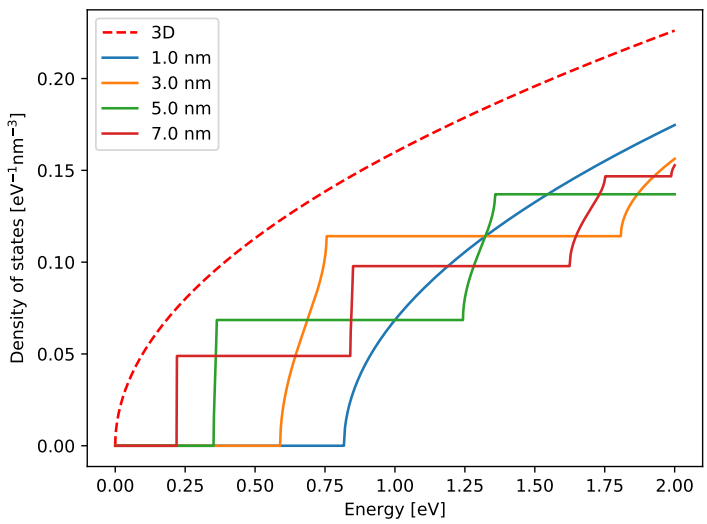

Figure 2.5: Density of states in superlattices of varying peridod d and equal well and barrier width, with the well material's conduction band edge as reference. The 3D density of states is also depicted.

Finally the thermoelectric properties can be computed, assuming a phonon thermal conductivity of $1.5\,\mathrm{Wm^{-1}K^{-1}}$. The figure of merit strongly depends on the Fermi level, as the electrical transport properties do, as demonstrated in Figure 2.6a. The local maxima in the figure of merit as a function of Fermi level are caused by the discontinuities or at least sharp changes of the density of states, around which as stated above the Seebeck coefficient

increases. The global maximum is usually achieved around the first miniband (closest to the band edge), as the thermopower decrease and the increase of the electrical contribution to the thermal conductivity dominate the monotonically increasing electrical conductivity. To adequately compare the figures of merit of different structures, zT is evaluated for each structure at the Fermi level at which its maximum is attained. This Fermi level depends on the superlattice properties and typically increases as the well width decreases and the first miniband energy consequently increases. In Figure 2.6b the figure of merit is plotted for a superlattice in the limit of infinitely high and narrow barrier layers, which describes a free standing film and also a superlattice with equal well and barrier width and a barrier of 1.7 eV. In both cases the values are normalized to the computed figure of merit of the bulk material (0.54 at 300K). Clearly the confinement effect is much less pronounced in case of the superlattice, as can be expected. While the figure of merit of the free standing film exceeds the bulk value at a thickness about 9 nm, the same occurs in case of the superlattice only at well widths below 7 nm, depending on the ratio of well and barrier layer. Moreover the increase is not monotonic with decreasing well width. Below certain well widths, again dependent on the well/barrier ratio, the figure of merit decreases. The reason is that the confinement effects eventually decrease with the barrier width. Consistent with this the zT maximum is reached at smaller well widths, when the relative barrier width is larger, i.e. confinement can be sustained for smaller superlattice periods as the barrier to well width ratio increases. On the other hand at larger well widths superlattices with smaller relative barrier widths have a larger figure of merit and match the bulk value sooner, which is due to the higher proportion of well material which increases the overall density of states.

Finally the influence of the barrier height was studied.

In agreement with expectation more substantial enhancements compared to the bulk material are achieved at greater barrier heights. At potential barriers less than 0.1 eV the figure of merit can be barely enhanced irrespective of layer thickness due to the weak confinement.

The study of in-plane properties of superlattices reveals that the enhancement of in-plane thermoelectric properties in theses structures is feasible, but requires well thicknesses under 7 nm. Moreover it motivates experimental investigation of high band offset superlattices, as enhancement of the thermoelectric properties is expected to be most pronounced in this case.

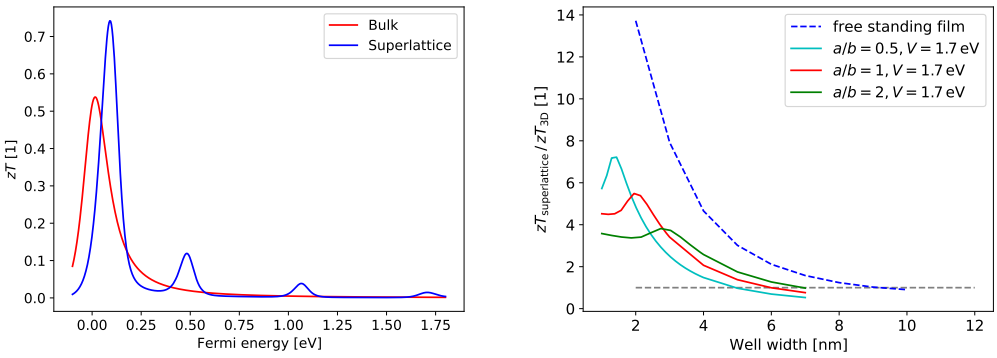

Figure 2.6: The figure of merit is plotted as a function of the Fermi level (relative to the conduction band edge in the well material) (a). For the superlattice equal well and barrier widths of 5 nm were assumed. Figure (b) shows the figure of merit of a free standing film of varying thickness compared to the figure of merit of a superlattice of equal well and barrier width and a conduction band offset or barrier height of 1.7 eV.

While the discussion above only relates to transport along the layer planes, similar enhancements can be achieved cross-plane. In this case only states within the minibands can contribute to transport.

The lattice thermal conductivity of multilayers has not been covered. However Chen et al. [14] showed that in case of diffuse scattering the thermal conductivity reduction in multilayers can be described by the conductivity reduction by boundary scattering in free standing films discussed in Subsection 2.1.2. This indicates that thermal conductivity reduction below that of an equivalent solid solution is feasible.

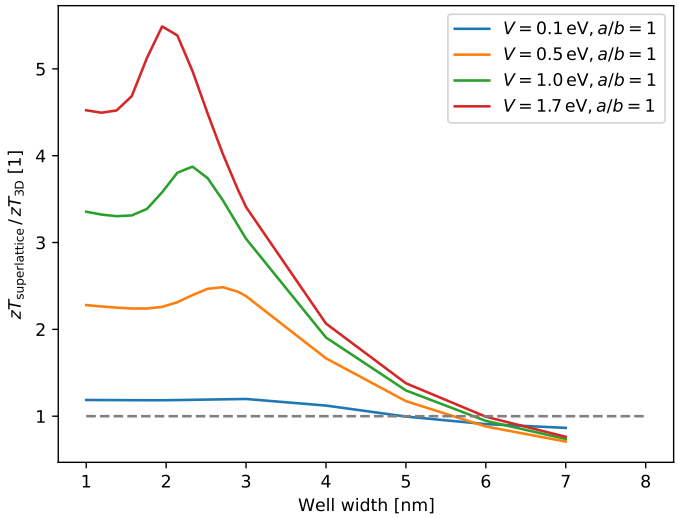

Figure 2.7: The figure of merit in relation to the bulk value is plotted for varying well widths and potential barriers.

2.3 Strategies of efficiency enhancement

Several different kinds of attempts to enhance the conversion efficiency have been made. Most improvements are a results of one or a combination of the following strategies: band structure engineering, alloying and nanostructuring [15, 16]. Band structure engineering can significantly increase the density of states at certain energies and thus lead to significant improvements in the power factor. One important example of this is the introduction of resonant levels by doping. Conventional doping introduces states that lie within the band gap, just below the conduction or above the valence band. In contrast to this case resonant levels lie within the respective bands and this causes an increase in the density of states within the respective band and a strong energy dependence. Examples are thallium in the valence band of PbTe and tin in the valence band of Bi_2Te_3 [17].

Complex material systems have been created by alloying to realize the concept of the phonon glass electron crystal, i.e. to decrease the thermal conductivity without affecting the electrical conductivity. Examples are skutterudites and clathrates. In these materials weakly bound atoms within the lattice perform a rattling motion and therefore are effective phonon scatterers, while simultaneously acting as dopants in some cases [15, 16].

2.4 Nanostructuring

Most of the recent advancements in the field of thermoelectricity can be attributed to nanostructuring [18]. An important theoretical result derived by Bergman and Levy [19] regarding two-component, isotropic composites is that their effective figure of merit can never exceed the largest value of figure of merit of any of the components, in the absence of size and interface effects. It demonstrates that improvement of a material's thermoelectric conversion efficiency by nanostructuring can only be achieved due to exploitation of size effects.

Dresselhaus and Hicks first reported in 1994 that the figure of merit can exceed that of the bulk material significantly in lower dimensional materials like quantum wells or nanowires once the density of states is altered by quantum confinement [13]. Quantum confinement leads to sharp features like steps or peaks in the density of states, which increases the thermopower if the Fermi level is tuned correctly. However to observe quantum confinement the dimensions have to approach the electron wavelength which means that critical dimensions on the order of nanometers are required.

There is an other effect with less stringent demands on size, which is responsible for most of the reported zT enhancements due to nanostructuring. This is the decrease of the lattice thermal conductivity without much impact on the electrical conductivity. As was stated above, phonons of a wide range of wavelengths generally contribute to heat transfer, whereas charge carriers all have energies close to the Fermi level, where the only free states are. Even though the phonon density of states is approximately proportional to ω^2, which means that there are more phonons of shorter wavelength, these carriers are also more significantly affected by phonon-phonon scattering, which means that phonons of all wavelengths contribute about equally. This explains why boundary scattering at scales much larger than the phonon mean free path can significantly reduce the thermal conductivity, without affecting as much the electrical conductivity and this in spite of the fact that charge carrier mean free paths can be larger than phonon mean free paths. Boundary scattering of the phonons is however once again not the only effect leading to a decrease of k_l. As the diameter of nanowires for instance decreases, the phonon dispersion departs from that of the bulk material, typically leading to lower group velocities and even energy gaps [20].

One typical route to obtain nanostructures is the growth of nanowires, which is often

applied since it can be relatively simple, especially when a vapor-liquid-solid method or structure-directing polymers are used. Templates can be obtained by ion track etching of polycarbonate membranes [21, 22, 23] or anodization of aluminium [24, 25, 8].

The disadvantage of nanowire arrays as thermoelectric generators is that they are fragile without a supporting matrix and a supporting material usually lowers the efficiency, since it possesses a finite thermal conductivity but does not contribute to the conversion in general. Moreover high fill factors have to be achieved in order to obtain the desired currents.

Thus several techniques have also been applied to obtain 3D nanostructured materials. These include hot pressing of nanoparticles obtained by a hydrothermal method [26], spark plasma sintering [27] of nanowires and even drop casting of PEDOT:PSS passivated nanorods [28]. In addition to methods starting from nanoparticles or -wires, deposition into 3D templates [29] or inclusion of nanoparticles [30] has been used more recently.

The remarkable figure of merit of 2.4 at room temperature was achieved in a Bi_2Te_3/Sb_2Te_3 superlattice grown by metallorganic CVD by Venkatasubramanian and others in 1997 [1]. They consisted of alternating layers of the two named materials and the superlattice period was varied from 2 to about 20 nm. The main reason for the enhanced zT in these structures is not quantum confinement, which is expected to be negligible, but rather the decrease of the lattice thermal conductivity. The improvement in zT was moreover determined for the cross-plane direction. The lattice thermal conductivity of the superlattices becomes comparable to that of the solid solution alloy at periods around 12 nm and continues to drop as the period is decreased until it reaches a minimum for a period around 5 nm. At this thickness κ_{ph} of the solid solution exceeds that of the superlattice by a factor of 2.2. Interestingly the lattice thermal conductivity increases again as the thickness is decreased even further until it approaches the solid solution value at periods smaller than 2 nm. Venkatasubramanian et al. suggested that once the periods falls below the minimum repeat distance, which in the Bi_2Te_3 system is the thickness of a quintuple layer ($\approx 1\,\mathrm{nm}$), it can be thought of rather as an ordered alloy than a superlattice. Simkin and Mahan showed that the phonon dispersion in superlattices significantly deviates from the bulk [31]. Decreasing the superlattice period eventually decreases the amount of band folding and thus an increase of κ_{ph} can be expected. The mentioned increase was not observed experimentally in several other superlattices. It was however demonstrated that the disagreement can be explained by interfacial roughness [32], as it can dominate the

band folding effect.

Apart from enhanced phonon scattering, superlattices can have improved electrical transport properties even in absence of strong quantum confinement. Higher average carrier energies in the lower band gap material can cause a decrease of impurity scattering and therefore higher mobilities while the Seebeck coefficient can be enhanced due to low energy carrier filtering.

The reported high figure of merit is due in part to the observed disappearance of the electrical conductivity anisotropy at small periods, which is about 2.5 for hole conduction and is not well understood [33]. Attempts to reproduce the outstanding results by methods other than MOCVD, namely molecular beam epitaxy (MBE) or sputtering have failed. Either electrical (sputtering) or thermal transport properties (MBE) could not be matched [34]. Fabrication of superlattices by electroplating can be achieved by exploiting the potential dependence of the composition when depositing alloys. In all cases of electrochemically grown superlattices thermoelectric characterizations have not been reported [35, 36, 37]. For the bath described later the growth rate at 0°C is just about 3.5 nm/min without forced convection. It is thus feasible to deposit superlattices by pulsed deposition. As Te is the more noble compound layers of nearly pure Te can be deposited by raising the potential. Thus superlattices of the Bi_2Te_3/Te t ype or such in which the alternating layers consist of Bi rich and more stochiometric Bi_2Te_3 could be grown.

Superlattices of the $Bi_{2+x}Te_{3-x}$ / Te kind are anticipated to have improved thermoelectric properties mainly due to the high acoustic mismatch between the layers, caused by the significantly greater atomic mass of Bi compared to Te. This is expected to suppress the phonon thermal conductivity, particularly cross-plane. The higher band gap offset (cf. Figure 2.8) could facilitate the achievement of confinement effects, however the significant differences in electron affinity between bismuth telluride and tellurium (about 3 eV) will likely cause a broken-gap multilayer with significant band bending, which could dominate any improvements by quantum confinement.

Thus an other multilayer consisting of bismuth telluride and polypyrrole, a conductive polymer, was also considered, for which observation of quantum size effects is expected to be more likely.

Electrochemical methods allow template assisted growth and this means that well defined 3D structures can be fabricated. More precise control of the architecture allows a systematic

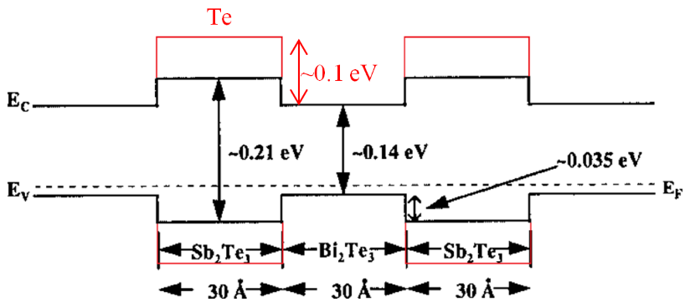

Figure 2.8: Ideal band diagram of a Sb_2Te_3/Bi_2Te_3 superlattice. Red features indicate the ideal band diagram in a $Bi_{2+x}Te_{3-x}$ / Te superlattice. Adapted from [1]

study of the size dependence of thermoelectric transport in 3D materials that has not been conducted to date.

2.5 Electrodeposition

Electrodeposition is the process of obtaining a solid deposit from charge transfer to ionic species in an electrolyte by application of a voltage between two electrodes immersed in the electrolyte. Usually the deposit is obtained on the cathode by reduction of cations while charge neutrality is maintained by an oxidation reaction on the anode. The latter can involve the oxidation of anions in the electrolyte or oxidation of the anode itself.

The potential of the cathode or anode is usually determined relative to a third so called reference electrode, instead of only considering the voltage between cathode and anode. The reason for this is that a potential difference between the bulk of the electrolyte and any electrode develops, which depends on the electrode, the electrolyte and also any applied potentials. The reason according to Stern's model is the formation of a double layer, known as Helmholtz double layer, adjacent to the electrode, the inner of which consists of oriented solvent dipoles and some absorbed ions and an outer Helmholtz plane consisting of solvated ions. Outside the double layer the potential relaxes to the bulk value within a diffuse so called Gouy-Chapman layer. This potential difference is for instance also relevant to the stability of colloidal suspensions (zeta potential).

The reference electrode is not exempt from this effect, but the unmeasurable absolute electrode potential of a reference electrode is required to be a constant. This is usually achieved by comparison to the standard potential of a charge transfer reaction under controlled conditions. One traditionally important example is the standard hydrogen

electrode, whose potential is determined by the standard potential of the hydrogen oxidation reaction under normal conditions (0 V by definition). Other reference electrodes based on other redox systems have been developed. Generally the reference electrode can be thought of as a half cell of well defined potential. Contact to the external electrolyte is established by a salt bridge, typically a porous glass frit.

A potentiostat or galvanostat is used to control the three-electrode cell. In the former case a potential is applied between anode (also referred to as counter electrode assuming the desired product is obtained from a cathodic reaction) and cathode (also referred to as working electrode in case the deposit results from a cathodic reaction) such that the desired voltage between reference and working electrode is reached, the cell current can be recorded during the experiment. In the latter case a constant current is applied and the voltage between reference and working electrode recorded. Particularly in the case that a voltage is applied good electrical contact between the potentiostat and the working electrode needs to be established, since Ohmic drop can cause a smaller than expected effective voltage to be applied when current is flowing otherwise.

Depending on the deposition conditions and electrolyte properties various effects can limit the current when an overvoltage is applied. Conductivity could be the limiting factor in an electrolyte of low concentration. This can be a disadvantage when homogeneous deposits are sought, as the deposition rate will vary depending on the field strength which matters particularly when the anode and cathode area differ significantly. In case of a small cathode area the field line density is significantly greater at the edges compared to the center of the cathode area resulting in higher deposition rates at the edges. A low concentration can be desirable for instance when expensive materials are used. By increasing the conductivity with a supporting electrolyte containing species that are not electroactive within the deposition potential range, Ohmic drop within the electrolyte and migration limited deposition can often be avoided. If this is not feasible so called thief electrodes are placed around areas of interest to avoid the effect of field concentration at edges.

Most desirable in terms of achieving homogeneous plating is the reaction rate limited current. In this case the current as a function of overpotential can often be described by the Butler Volmer equation, which predicts linear dependence for small overpotentials and exponential dependence for larger ones. When the overpotential is increased further diffusion limited deposition can occur. This is usually also inevitable when the electroactive

species has a low concentration. While migration limited current can be avoided by using a supporting electrolyte, as stated above, diffusion limitation can hardly be avoided in this case. Forced convection can be applied, but particularly in case deposition into microstructured templates involving small cavities is carried out, diffusion limitation is likely inevitable.

Diffusion limitation can be undesireable as it causes enhanced current density around protrusions on the deposited film further enhancing the growth of these protrusions, thus leading to rough and potentially even dendritic deposits.

The electrodeposition of semiconductor compounds can be challenging for several reasons. High resistivity can cause increasing Ohmic drop within the deposit and depositing compounds requires the components to have similar standard potentials. Co-deposition from aqueous electrolytes becomes impossible when the difference in standard potentials exceeds the window of the electrochemical stability of water, i.e. 1.23 V. In many cases however compound electrodeposition can be carried out at potentials more positive than the deposition potential of the less noble element, which is referred to as induced co-deposition. Electroplating, when applicable, is cost-effective and energy-efficient relative to other fabrication methods. Moreover nanostructured deposits can be obtained even without templates by modulating process parameters such as the deposition potential.

Generally the deposited moles can be related to the charge by the Faraday constant F which is the charge per mole of elementary charges, i.e. $F = N_A e \approx 96485\,\mathrm{C\,mol^{-1}}$, where N_A is the Avogadro constant. If z denotes the number of elementary charges which need to be transferred to obtain one unit of the product, the moles obtained when the charge Q is deposited at a current efficiency of 100 % is $\frac{Q}{zF}$. In practice the current efficiency is usually lower due to side reactions. With a current efficiency of η the (average) thickness of the deposit d can be determined as follows:

$$d = \frac{\eta Q V_m}{zFA} = \frac{\eta Q M}{zFA\rho}, \tag{3}$$

where V_m denotes the molar volume, A the area of the working electrode, M the molar mass of the deposited compound and ρ its density. In case of bismuth telluride, considering its molar mass of $800.76\,\mathrm{g\,mol^{-1}}$, density of $7.7\,\mathrm{g\,cm^{-3}}$ and that $z = 18$ electrons are required to reduce one unit, a thickness per charge density of $0.599\,\mathrm{\mu m\,cm^2 C^{-1}}$ is expected. Assuming

that the alloy's density as a function of composition can be described by Vegard's law, the expected rate can be computed for any composition, cf. Figure 2.9. The main cause for the thickness increase as the bismuth content increases is that 4 moles of electrons are required for the reduction of every mole of Te(IV) ions, whereas two are required for every mole of Bi(III).

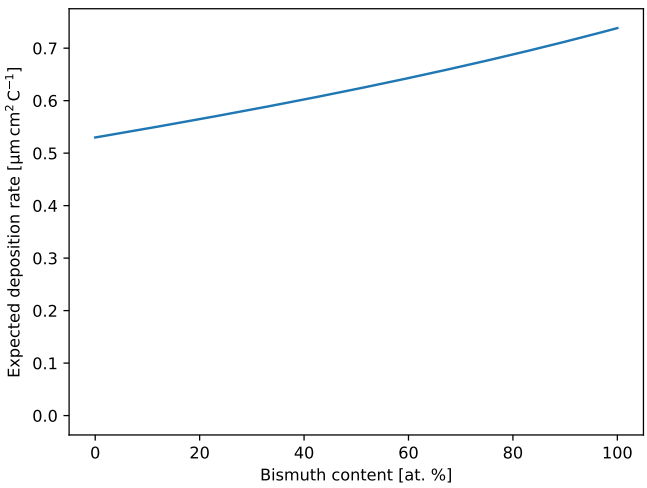

Figure 2.9: The expected film thickness is plotted as a function of the binary alloy's composition.

2.6 Effect of annealing

Regarding Bi_2Te_3 obtained by electrodeposition a full thermoelectric characterization, i.e. at least measurement of electrical and thermal conductivity and the thermopower, is often not carried out. In case the power factor was determined typically thermopowers $|S| < 100\,\mu\mathrm{V/K}$ are observed in as-deposited samples. As mentioned above, the thermopower is very sensitive to the carrier density and thus the dopant concentration. Low thermopower can be caused by a low dopant concentration on the one hand (in fact intrinsic semiconductors have thermopowers close to zero) or the opposite case [10], as further discussed in Subsection 5.3.2. Since a low dopant concentration typically also leads to a low electrical conductivity, discerning between the two cases is possible by measuring both S and σ. In electrodeposited samples typically excessive doping is found to be responsible. Annealing was found to improve the power factor significantly. In few cases an increase of both thermopower and

resistivity was observed, which is consistent with a decrease in the carrier density [38]. In most cases however $|S|$ and σ were found to increase [39, 40, 41]. This can be explained by an increase in the charge carrier mobility due to decreasing defect density, which dominates a likely also occurring decrease of the carrier density. Significant grain growth is generally already observed at temperatures around 250 °C, excessive heating should be avoided since tellurium is known to evaporate. For the same reason care has to be taken when annealing superlattices, in order to avoid interdiffusion.

Moreover pulsed plating was found to result in larger grain sizes, lower roughness and improved thermoelectric properties (higher $|S|$and σ) [41, 39, 42], with the exception of [43]. During the off-time it is ensured that no deposition occurs, i.e. no current flows, which allows ions depleted during the on-times to be replenished. In the latter study pulsed plating resulted in decreased power factors, which might be due to equal on- and off-times. Most other studies find enhanced properties at $t_{off}/t_{on} > 1$.

2.7 Measurement techniques

As stated above, a full characterization of a thermoelectric material requires at least the measurement of thermopower S and electrical and thermal conductivity, σ and κ respectively. The electrical conductivity can in many cases simply be determined by the well known 4 point probe technique. The measurement of the thermopower is similar in that it requires measurement of the voltage drop along the sample induced by a temperature gradient. Both quantities can be measured while the sample is supported on an electrical insulator, at least in the in-plane direction. Since thermal insulators of similar quality as electrical insulators do not exist, determining the thermal conductivity is more complicated. Several methods have been developed. Generally the thermal conductivity (in general a second-rank tensor) relates the heat flux to the temperature gradient, i.e. $\mathbf{q} = -\kappa\nabla T$ which is Fourier's law. Thus to determine κ, measurement of temperature differences and heat flux is required regardless of the specific method used. In case of thermoelectric materials it is important to note that κ is the thermal conductivity at zero current, since an electrical current, that would be induced if the sample is short circuited for instance, contributes to the heat transfer.

In many cases obtaining nanostructured thermoelectric materials that can undergo

conventional thermoelectric characterization methods is not feasible. This particularly applies to deposition based fabrication methods, namely electrochemical [30, 29] and physical [44, 45, 34] or chemical [46] vapor deposition. Typically these processes are limited to the deposition of films on the order of micrometers. For microscale samples different characterization methods have been developed. Few allow the measurement of all required material properties on the same sample and even fewer along the same orientation. The latter can be important as many thermoelectric materials exhibit anisotropy [47]. Films obtained by deposition processes typically have low aspect ratios. Therefore the term "cross-plane" is used to refer to measurements in the growth direction, while "in-plane" is used to refer to measurements orthogonal to the growth direction.

Based on how the sample is heated and its temperature measured optical and electrical methods can be distinguished (or in rare cases combinations), cf. Table 2.1. In case of anisotropic materials care has to be taken to measure heat transfer in a specific direction. This is typically not the case if the heat source approximates a point source and the sample is a supported bulk sample. This case arises for instance when a Scanning Thermal Microscope (SThM) or Micro-Raman spectroscopy, briefly discussed in the following, is applied. Oriented measurements can still be achieved under certain conditions, such as that the film is much thinner than the laser spot or tip radius and is supported on a much more conductive substrate (cross-plane) or the substrate is a thermal isolator (in-plane). The latter case can be achieved by measuring on suspended samples [48].

Several other techniques require the deposition of auxiliary thin films. The 3ω-method was developed by Cahill and Pohl in 1987 [49, 50] to study the temperature dependent thermal conductivity of dielectric films. It exploits the temperature dependence of the electrical resistance. When an AC current of angular frequency ω is applied to a heater, the heating power and thereby the temperature excursion has a component oscillating at a frequency of 2ω, under the condition that the period of the heating current exceeds the thermal time constant. Thus the resistance R of the heater is a constant with a small contribution oscillating at 2ω. Consequently the voltage $R \cdot I$ is a superposition of the sinusoidal voltage at ω and a by orders of magnitude smaller contribution at 3ω. The amplitude of the 3ω-signal is inversely proportional to the thermal conductivity of the surrounding material. As indicated above, if the width of the heating line is significantly greater than the underlying's film thickness and it is supported on a highly conductive substrate, the assumption of 1D

cross-plane transport can be made. But the 3ω-method has also been applied to suspended films, in which case 1D in-plane transport measurements can be obtained if the width of the suspended segment is much greater than the film thickness. The advantage of the 3ω-method is that very precise measurements can be achieved by lock-in amplification. The main disadvantage of the approach is that cross-plane measurement on an electrically conductive sample requires electrical insulation of heater and sample which is often achieved by deposition of a thin dielectric layer, which can potentially obstruct measurement of the other thermoelectric properties. It should also be noted that the 3ω-method has also been applied directly to suspended wires, in which case it is used as a self-heating method, which will be discussed further below. This approach is in principle similar to the one primarily used in the present studies.

An other method requiring deposition of an auxiliary layer is time domain thermoreflectance (TDTR), deposition of a metallic layer is used to measure the reflectivity changes induced via the piezo-optic effect. A pump laser heats the metallic pad, while the change of its reflectivity is monitored by a probe laser beam. The temperature can be derived from reflectivity changes, as a temperature increase induces strain which in turn causes changes to the refractive index and thus the reflectivity.

A technique loosely related in that the heat source is again a laser beam is the laser flash method. The time required for a temperature rise to occur on the back side of the sample is related to the thermal diffusivity and can be measured in contact using a thermocouple or without contact by an infrared detector or TDTR. The method is usually applied to bulk samples (thickness on the order of mm) due to the timescale. For instance in case of a 1 µm thick sample of bismuth telluride the time to half maximum would be about 0.1 µs, too fast for an infrared detector. Thus for thin films the method is usually combined with TDTR.

TDTR, the 3ω-method and laser flash analysis have in common that a transient effect, i.e. heat diffusion, is investigated, which does not only depend on the thermal conductivity but rather the thermal diffusivity, i.e. density and specific heat in addition to the thermal conductivity. In case of the 3ω method these dependencies can be eliminated by measuring at a range of frequencies, but in general knowledge of these additional, potentially uncertain material properties is required in case transient methods are applied.

The Micro-Raman method is interesting as it is a non-contact method of determining the thermal conductivity without the requirement of auxiliary films. It relies on shifts of

peaks in the Raman spectrum induced by temperature excursions. In case of Bi_2Te_3 the shifts are caused by the lattice expansion. The sample is locally heated by a laser beam focused onto the sample through a microscope. The temperature of the heated spot is determined from the peak shift. This temperature depends on the absorbed power and the thermal conductivity of the sample, in addition to dimensional properties. While elegant, the problem with this approach is that these peak shifts are not very sensitive to temperature, for instance $-0.014\,\mathrm{cm}^{-1}/\mathrm{K}$ at a FWHM of about $10\,\mathrm{cm}^{-1}$ in case of Bi_2Te_3 [51]. This means that significant temperature excursions of about 60 K are required. Moreover there is the problem of determining the absorbed power and the spot size.

The photoacoustic method relies on periodic heating of the sample by a laser and measuring the acoustic response with a microphone. The amplitude and phase shift are used to derive the thermal conductivity. The disadvantage of this method is the complexity of the model and the amount of thermal and optical material properties of the sample and substrate required.

	In-plane	Cross-plane
Electrical	Suspended PRTs	
	Self-heating	
	3ω method	
	3ω-Scanning thermal microscopy	
Optical		Photoacoustic
		Laserflash
	Micro-Raman	
	TDTR	

Table 2.1: Overview of different methods used to measure the thermal conductivity.

All those approaches in which the only heat source is the electrical current through the sample (via Joule heating or the Peltier effect) can be described as self-heating methods. The advantage of these methods (and purely electrical methods in general) is that they only require measurements of voltages and currents, which means that they can more easily be performed in vacuum avoiding convection cooling. Since they are more direct and straightforward than other methods, they moreover require fewer material properties and simpler models can be used to derive the thermal conductivity if the samples are suspended. The disadvantage of these methods is that obtaining suspended samples can be cumbersome. In case the method used involves using the sample itself as a resistance thermometer, a way to control the sample temperature needs to be established and calibration measurements

need to be performed.

In case of exclusively in-plane measurements it is usually necessary to release samples from the substrate, as the substrate can thermally short circuit the samples. In 2001 a suspended microbridge device for the measurement of the thermoelectric properties of carbon nanotubes was designed [52] by Li Shi. Since then devices of this kind have been used for thermoelectric characterization of diverse materials [53, 10, 54]. The measurement device is composed of two microscale islands consisting of a dielectric material (usually silicon oxide or nitride) approximately measuring 20 by 20 µm, each supported only by beams of high aspect ratio, to achieve thermal isolation. The sample is placed between these islands, forming the only bridge between them in some cases. Meandering platinum traces serving as heaters and platinum resistance thermometers (PRTs) simultaneously are patterned on both suspended platforms. The measurement principle is to first determine the combined thermal conductance of the supporting beams K_b per platform (assumed to be equal for both sides) from the heating power and the resulting temperature rise on both sides, i.e. $K_b = (P_l + P_h)/(\Delta T_h + \Delta T_s)$, where the subscript h denotes the heated and s the sensing side and P_l is the Joule heat generated within a single beam. The thermal conductance of the sample suspended between the islands, K_s, can then be determined from $K_s(\Delta T_h - \Delta T_s) = K_b \Delta T_s$. This expression is based on the observation that heat conducted through the sample from the heated side to the sensing one is equal to the heat conducted from the sensing side to the substrate through the supporting beams in steady state. The main underlying assumption is that heat is exclusively conducted through the sample and the supporting beams. This means that other modes of heat transfer, namely convection and radiation, have to be suppressed. Conduction can be avoided by carrying out the measurements in vacuum.

Generally radiative heat transfer has to be accounted for whenever it becomes significant relative to heat conduction, which is for instance the case when thermoelectric materials of inherently low thermal conductivity are investigated. The importance of radiative heat transfer, i.e. the ratio of radiative to conductive heat transfer, can be approximated as $\frac{L^2(t^{-1}+w^{-1})\sigma\varepsilon\bar{T}^3}{\kappa}$, where L,w and t are length, width and thickness of a suspended sample, ε its emissivity and $\bar{T}$ its average temperature, as will be further analyzed in Section 5.2. This is the case as radiative heat transfer is approximately $2\sigma\varepsilon(t+w)\bar{T}^3\Delta T$ and conduction $\kappa\Delta T wt/L$. The dependence on L^2 reveals why samples on the microscale are preferable when films are investigated. The ratio also depends on the third power of the average

temperature, which becomes important when measurements at temperatures significantly different from room temperature are performed. A radiation shield thermally anchored to the sample holder can mitigate this problem, which together with microscale dimensions ensures that radiative heat transfer can be ignored.

Various configurations involving micro-bridge devices have been implemented. They can be considered one of the most accurate, precise and comprehensive characterization methods. The disadvantages are the complex fabrication process which requires patterning of the PRTs and electrodes usually by electron beam lithography or at least a wafer stepper as in [55], since conventional lithography can hardly meet the requirement of sub-micron resolution, and patterning of the underlying dielectric layer by photolithography and reactive ion etching (RIE). The process of transferring the sample onto the measurement device is also complex and tedious, usually requiring a micromanipulator. And when the sample is drop cast onto the devices, for instance a nanowire suspension, or consists of an entire film, for example graphene, additional steps are required: Either a third lithography is required to remove excess parts of the sample to avoid shorting of the PRTs by the sample or the PRTs have to be electrically insulated for instance by depositing an oxide layer. In the latter case lithography can nevertheless not be avoided as windows in the passivating film need to be opened to allow for electrical contact to the sample. Establishing contact to the sample can also be challenging. This can be vital as often a pseudo 4-probe measurement is employed to measure the sample's electrical conductance, in which case the series electrical contact resistance contribution is included in the measurement value. The thermal contact resistance can also be significant for transferred samples. Attempts to determine the contact resistance by using the Seebeck effect to determine the temperature difference between pairs of outer and inner electrodes were made by Pettes et al. (see supporting information of [12]). To decrease contact resistance focused ion beam deposition into the contact area can be used to reduce contact resistances as it can not only increase the contact area but also break through the native oxide layer covering many semiconductors. The disadvantage is that this can cause defects in the sample and therefore change sample properties at least in the contact region. The complexity of the fabrication usually involving three lithography steps and of the sample transfer process and the post transfer treatment are the main disadvantages of this approach. Particularly in the case that samples are obtained by deposition, which can be usually carried out selectively on areas of interest by masking the remaining area, it

is desirable to develop measurement devices on which samples can be directly deposited, without the need for sample transfer.

To address this problem, a micro-bridge approach specifically designed for the in-plane characterization of electrodeposited samples was recently proposed by Barati et al [56]. The method is based on patterning a seed layer (Cr-Au) to form a bridge over a through-hole in the wafer. Initially the seed layer is supported by a silicon nitride film covering the through-hole. Four PRTs and one central heater are deposited across the seed layer by a lift-off process. The heater is isolated by ALD of silicon oxide, but the oxide is selectively removed from the PRTs and seed layer. Photolithography is then applied once more to create templates for electroplating on the seed layer. Electrodeposition of the sample onto the bridge is then carried out. Subsequently the underlying nitride layer covering the through-holes is etched from the back side and after this the seed layer can be removed by wet etching. Measurement of the sample's electrical conductance is straightforwardly accomplished by the 4 point probe method. The thermal conductance is measured by applying a heating current to the central electrode while simultaneously measuring the voltage drop and thus the temperature increase a the center. The heating power P is approximated by the product of heating current and voltage. The ratio of the heat conducted from the sample by the PRTs to the heat conducted through the sample is assumed to be negligible, and therefore the conductance is derived from $K_s \Delta T = P$. The assumption of ignoring heat conduction by the PRTs is only valid under the condition that the product of the sample's thermal conductivity and thickness exceed a lower limit. The platinum leads have a thickness of 150 nm and are 2 µm wide and platinum has a thermal conductivity of about $40\,\mathrm{Wm^{-1}K^{-1}}$. Therefore samples of several microns thickness need to be generally deposited on the seed layer. The authors study a cobalt-nickel alloy sample with the significant thermal conductivity of about $60\,\mathrm{Wm^{-1}K^{-1}}$ and a thickness of 6 µm. Under these conditions the expected systematic error lies below 4%. To not exceed 10%, the product of sample thickness and thermal conductivity has to exceed $180\,\mu\mathrm{W/K}$. So a sample of thermal conductivity $2\,\mathrm{Wm^{-1}K^{-1}}$ would have to be 90 µm thick. This is unreasonable and would violate the assumption of 1D transport. At a thickness of 6 µm the relative measurement error would be 475% according to the authors (see Table 2 of supporting information of [56]). Moreover the measurement of the Seebeck coefficient is questionable: The Seebeck voltage is measured using two of the PRTs while the central electrode is heated. According

to the authors these PRTs are also used to measure the temperatures. The PRTs are however clearly in electrical contact with the sample, and therefore the PRTs' resistance is necessarily altered by the parallel conduction path through the sample. The authors do not address this fact to the best of our knowledge. Resistance thermometry could in principle be carried out with a PRT shorted by the sample, but the temperature coefficient would be influenced by the sample and deviate from that of platinum. We acknowledge that the steps taken by the authors toward in-plane thermoelectric characterization of electrodeposited samples are interesting, but that the method as presented is unsuitable for samples of inherently low thermal conductivity and device preparation involves an extraordinarily tedious fabrication process, considering that it requires applying photolithography five times on the whole.

Therefore microdevices designed for the in-plane thermoelectric characterization of samples obtained by deposition processes, electroplating in particular, were developed. The thermal conductivity is measured by a self-heating approach introduced in 2009 [57, 58], while an additional electrode is used for the measurement of the thermopower. Thus all the three thermoelectric parameters are determined and the advantages of this method are the comparatively simple fabrication process, avoiding sample transfer and its negative consequences and accurate measurements over a wide range of thermoelectric sample properties. The developed method is validated by numerical modeling, comparison to results from literature and to measurements on reference samples.

In conclusion nanostructuring is in general a promising approach to enhance the figure of merit but also specifically in the bismuth-tellurium system, which we focused on due to its good bulk thermoelectric properties near room temperature. In case of bismuth telluride notable suppression of the thermal lattice conductivity can be observed for characteristic lengths lower than 100 nm, yet truly significant improvement due to quantum confinement can be expected at length scales below 10 nm.

While various measurement methods have been developed, the only comprehensive ones applicable to samples on the microscale require a complex fabrication and sample transfer process. This emphasizes the need for such a characterization method tailored to deposited samples and explains why much effort went into its development as outlined in the following.

3 Materials and methods

3.1 Microfabrication of measurement devices

3.1.1 First Design

The fabrication of the microdevices begins with the thermal oxidation of ⟨100⟩ silicon wafers. These were purchased from the Center of MicroNanotechnology, Lausanne. Electron-beam evaporation was then employed to deposit 5 nm Cr / 1 µm Au films, using an Alliance-Concept EVA760. Photolithography was applied to pattern the underlying metal films and oxide by etching, see Figure 3.1a. The oxide/metal films then serve as mask for the anisotropic etching of the underlying silicon. A potassium hydroxide solution was chosen as the etchant due to its low toxicity and high ⟨110⟩, ⟨100⟩ selectivity. During this process the metal/oxide layer is partially suspended, namely the areas onto which the sample is subsequently deposited (see Figure 3.1b and also 5.12a). The central segment is still supported after the etching process because its edges are aligned with ⟨110⟩. The notches in the design (see Figure 3.1a) have the purpose to facilitate undercutting. The suspended supports of the samples were deliberately designed to be much wider than the sample. This prevents deposition at the edge of the support to be joined with the sample due to overgrowth during the following electroplating. After silicon etching a second lithography is carried out to obtain templates for electroforming. Spin coating and the subsequent softbaking, which this involves, are critical steps in the process flow. The resin can collect in the pits that have been etched into the wafer or cover them, trapping air. In these cases bubbles can form as the solvent evaporates or the volume of the trapped air expands while softbaking. After softbaking the hardened bubbles usually cause the affected templates to be deformed in the critical suspended areas, possibly in part due to refraction by the deformed structures during exposure. Different attempts were made to prevent bubble formation. Introducing a relaxation time between spin coating and soft baking and gradual ramp heating during the softbake did not prove to be effective in this regard. The method finally applied was to pour a solvent of low vapor pressure, propylene glycol methyl ether acetate (PGMEA), over the wafer and then removing solvent from the wafer surface using a nitrogen gun prior to spin coating. Due to the low vapor pressure solvent remains in the pits even after treatment with the nitrogen gun for some time, as was confirmed

by microscopy. Shortly after the solvent treatment photoresist is applied and spin coating carried out. During softbaking bubble formation was prevented in case of nearly all devices. The disadvantage of this approach is that the resist thickness varies in the vicinity of the pits. This only is an issue if the intended sample thickness exceeds that of the resist.

After carrying out the electrodeposition, the photoresist is stripped and the oxide on the back side of the suspended structures is etched using buffered hydrofluoric acid. Subsequently the exposed metals on the top and back sides are etched, which leaves a sample with two freely suspended branches, concluding the fabrication. Figure 3.5a is a SEM image of a completed device. Electrodeposition of the various materials used for

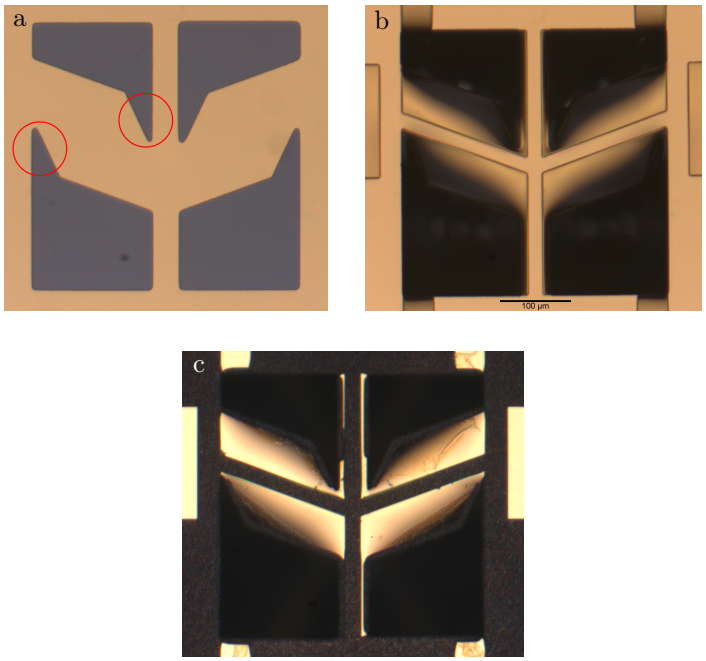

Figure 3.1: Optical microscope images of the microdevices at different stages of the fabrication process, namely (a) after the first lithography and etching of the exposed metals, two of the notches have been circled, (b) after anisotropic wet etching of the underlying silicon and the second lithography and finally (c) after electroplating into the prepared molds and stripping the photoresist. The final steps are etching of supporting silicon dioxide and exposed metals to obtain free-standing samples.

device validation is discussed in Chapter 4. In case of Bi_2Te_3 a film of thickness 2.05 µm with a root mean square (rms) roughness of about 100 nm was deposited, in case of bismuth 1 ± 0.27 µm and in case of Ni 74 ± 13 nm. Reasons for reducing the thickness of the in particular electrically more conductive Bi and Ni samples are stated in Sec. 5.3.2.

3.1.2 Improved Design

As discussed in Section 5.4, a design based on samples suspended over through-holes is superior to the original one for several reasons. Reliable fabrication of the improved devices requires using double side polished wafers. In this case it begins with 380 µm thick wafers on which wet thermal oxidation to a thickness of 1 µm had already been performed. On the front side 5 nm Cr and 1000 nm Au are sputter deposited at room temperature after brief in situ oxygen plasma cleaning. On the back side 5 nm Cr and 200 nm Au are deposited. The Cr/Au layer on the back side serves as the mask for wet etching the through-holes. Various silicon wet etchants have been applied and investigated. In the present application high selectivity of etching in the $\langle 100 \rangle$ direction with respect to $\langle 111 \rangle$ and SiO_2 is desirable. Etchants such as ethylenediamine pyrocatechol (EDP) and tetramethylammonium hydroxide (TMAH) and also ammonium hydroxide have superior selectivity with regard to silicon dioxide compared to potassium hydroxide. However potassium hydroxide has the lowest $\langle 111 \rangle$-etch rate by comparison and low toxicity unlike EDP and TMAH and is easier to handle than ammonium hydroxide which decomposes. With the etch parameters applied the oxide layer alone would be completely stripped by KOH before etching of the through-holes is completed. While several authors report a $\langle 111 \rangle / \langle 100 \rangle$ etch rate ratio of just 1.3 % [59] to 1.7 % [60], our results are in better agreement with Price et al. who find about 2.9 % [61]. The ratio depends on concentration and temperature among other parameters. It decreases with increasing temperature, however the SiO_2/ $\langle 100 \rangle$ ratio increases. The absolute rate is approximated by the Arrhenius equation, therefore, to minimize the etch duration but also avoid excessive undercut in the oxide the etching was carried out at 80 °C in a 30 % KOH solution.

While the $\langle 111 \rangle$-etch rate is low, it has to be taken into account. To achieve samples of a certain length, the dimension of the through-holes needs to be controlled. This is moreover important as it determines the width of the heating electrodes. The following relation between the width of the window on the back side w_b and the sample length L was derived: $L = w_b - 2\tan(\alpha) \times 378.7\mu\text{m} + 2\mu\text{m} + 2 \times 12.7\mu\text{m} \pm 2\tan(\alpha) \times 5\mu\text{m} \pm 20\mu\text{m}$ where the added or subtracted terms in order are due to the taper (378.7 µm is the silicon thickness after subtraction of the material consumed during oxidation), the undercut while etching the oxide, the undercut due to KOH etching of $\{111\}$ faces, the thickness variation of the wafer and finally an additional term accounting for uncertainty due to potential variation in

etch duration and rate, in each of the processes. The angle α, approximately 54.74°, is the taper angle and $\tan(\alpha) = \sqrt{2}$. Rearranging yields $w_b = L + (508 \pm 27)$µm. The electrodes on the front side were designed to be 30 µm each. Thus even when the hole is 27 µm wider on the front side, the heating electrodes would still be nearly 17 µm wide, provided front and back side features are well aligned. Hole widths outside the determined interval were never observed.

One more aspect to be addressed is the alignment of features on the back and front sides of the wafer. After etching through-holes into the wafer from the back side they are still covered by the oxide and metal films on the front side and are not always visible. They become discernible in some cases for samples corresponding to samples longer than 100 µm. In such cases the oxide/gold film can buckle. Special mask aligners allowing back side alignment have been developed. While such a device would be available in external clean rooms, an alternative approach, namely to etch alignment marks through the wafer was taken. The oxide/metal films covering theses holes were selectively removed from the back, making them visible on the front. The back side mask is the area shaded gray in Figure 3.2. The colored areas are exposed and, since a negative resist is used, are protected by resist post exposure. Apart from he through-holes in the center of the 1 by 1 cm chips one of the two the alignment marks is visible as well as white lines at the boundaries of the chip. These are intended to etch groves into the wafers, which later facilitate separating the chips by cleaving.

The first step in the process flow is to glue the front side of the wafer to a carrier wafer with hot glue easily soluble in acetone. The purpose is to protect the front side from contact with various surfaces. Photolithography was then carried out using the low viscosity version (115 cps) of MicroChemical's AZ 15nXT negative photoresist (nominal thickness 4 µm under applied process parameters). Care was taken during mask layout to facilitate aligning the flat of the wafer with the design. This is required as the edges of the holes are parallel or orthogonal to the flat by nature of anisotropic silicon etching. After spin coating, exposure and development the sample was cleaned using oxygen plasma, as organic residue was in some cases discovered on unexposed areas. Subsequently the exposed gold and underlying oxide is etched (Figure 3.3b).

The etch through the silicon substrate (Figure 3.3c) is then performed with a 30 % KOH solution at 80°C in a watch glass covered beaker to prevent evaporation. Stirring does

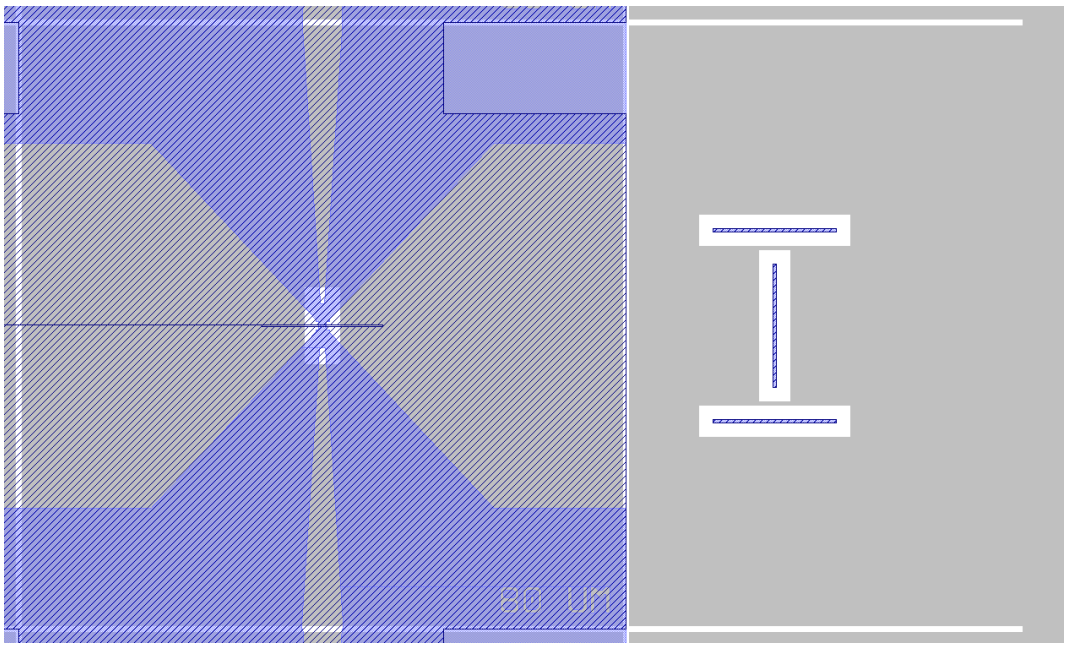

Figure 3.2: Excerpt of the final mask layout. All filled areas are exposed and thus remain covered by photoresist post development. The feature on the right-hand side is one of the two alignment marks, the square shaped area (1 by 1 cm) on the left-hand side represents one of the microdevices. The gray area is taken from the back side mask layout. The The purple area represents the electrode layer on the front side. The hatched area is exposed during the final photolithography. During this step the template for electroplating is formed. The only exposed gold remaining after this step is the sample mould at the center of the chip and the area in the top right-hand corner which is used to make electrical contact to the chip for electrodeposition.

not seem to be important, as pronounced diffusion effects are not expected [61]. Minor inhomogeneities in the etch rate but not critical ones were observed. The completion of the etching process can be discerned as gas evolution within the pits ceases. After etch completion the metal/oxide layer covering the trenches corresponding to the alignment marks are etched from the back side by dispensing drops of the respective etchants into them. Light falling through the holes marks successful completion of the etch. After cleaning of the front surface in a piranha solution photolithography is carried out on the front side to pattern the gold layer (Figure 3.3d). The purple layer in Figure 3.2 serves this purpose. In this case the more viscous version of the resist (450 cps) is used, to obtain a thicker resist layer (nominally 8 µm). In case a thin layer is applied and after oxygen plasma treatment partial failure of the masking layer was once observed after gold etching. While in case of etching gold on the back side exposure to the gold etchant for about 20 s is sufficient, gold on the

front side needs to be exposed for at least 2 min due to the greater thickness. Apparently the etchant was able to penetrate the mask and moderately affect the surface, applying the more viscous resist prevents this.

Finally the wafer is once again cleaned and a final lithography is carried out to obtain templates for the deposition process (Figure 3.3e). One of these is represented by the hatched area in Figure 3.2. The only openings in the resist layer are a trench in the center intended for sample deposition and an opening in the top right-hand corner which facilitates establishing electrical contact to the gold layer required for electrodeposition. This is accomplished using copper tape and patches of silver paint bridging the copper-gold boundary to decrease contact resistance.

After electroplating (Figure 3.3f) tape adhesive residue is first removed using cotton swabs soaked in acetone since it is not completely dissolved by the later applied solvents and can thus contaminate the sample. Remaining photoresist is then stripped in MicroChemical's trademarked TechniStrip NI555 at 80°C. Based on the safety data sheet the main ingredient is the solvent di(propylene glycol) methyl ether with a small amount oxalic acid (less than 2.5%). Finally to release the sample etching of the silicon dioxide, chromium adhesion layer and gold is etched from the back side (Figure 3.3g). As for the alignment marks light from an LED falling through the through holes marks the completion of the gold etch thus preventing overetching. The etching process is terminated by careful rinsing with DI water. Finally the chip is carefully rinsed with ethanol and left to dry. Water is replaced by ethanol before drying since the latter has a significantly lower surface tension, which reduces the likelihood of the sample's destruction by capillary forces, an effect sometimes referred to as stiction.

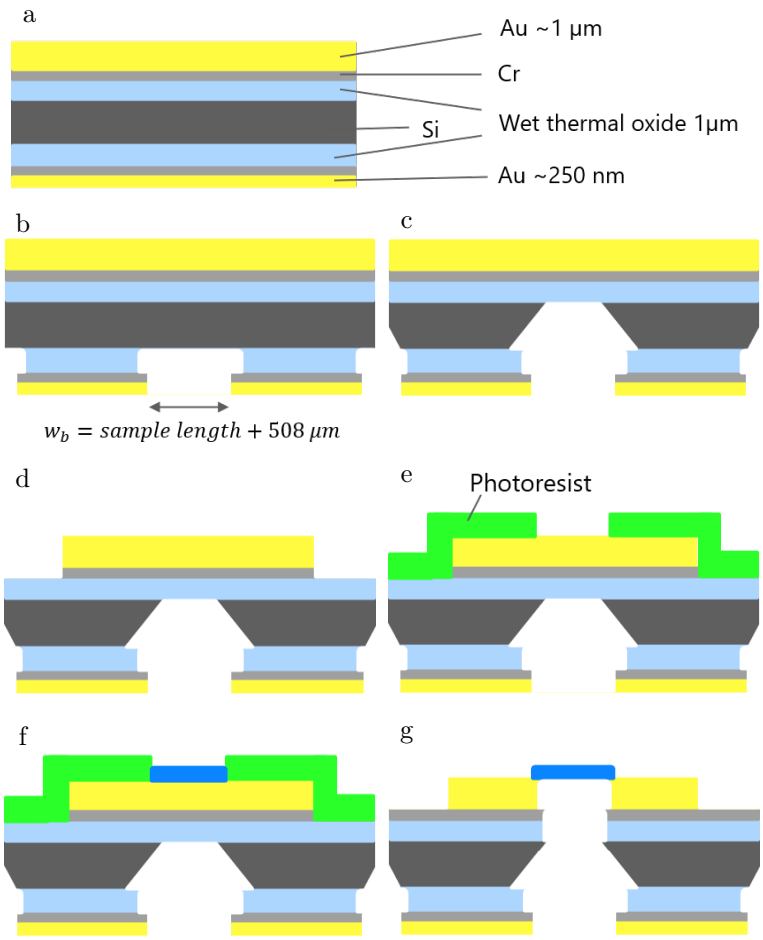

Figure 3.3: Not-to-scale schematic illustrating the fabrication process of the improved microdevices. First steps are the wet thermal oxidization and metallization of the double side polished wafers (a), followed by the first lithography required to etch windows into the metal and oxide films on the back side (b). The underlying exposed silicon is then etched, which creates through-holes (c). After cleaning a second photolithography step is applied on the front side followed again by chemical metal etching to pattern the electrodes (d). A third lithography is then applied to obtain templates for electroplating (e). The samples can be electrodeposited into these (f) and finally sample release is achieved by resist stripping and etching of the oxide and metal films from the back side, which completes the fabrication.

3.2 Setup and reference sample preparation

All measurements on the microdevices were carried out in a self-made setup in high vacuum to avoid convective heat transfer. It is built up on a heated base plate, which consists of a meander-shaped, insulated nichrome wire clamped between two copper plates. The sample holder, a smaller copper plate, is screw mounted on the base plate. Leads (Ø 1 mm), which are used to establish contact to the chip, are clamped between base plate and sample holder. This ensures that the leads are at the same temperature as the sample holder preventing heat conduction from the chip through the leads. Since a ground fault occurred later electrical insulation of the leads was improved by oxide coated silicon chips and holding them in place with thermally conductive epoxy, which maintains good thermal conductance. A platinum resistance thermometer was also glued to the substrate holder with thermally conductive epoxy, which is used to control the sample holder's temperature to mK precision by PI control.

A radiation shield, i.e. a copper enclosure at least 3 mm strong is mounted to the base plate to minimize radiation heat transfer to the wall of the chamber. Applying thermal paste ensures good thermal conductance. Originally contact between the chips containing the microdevices and the sample holder was also established by thermal grease. Thermal grease can however be pressed through the chip through-holes of the modified design and contact the sample, thwarting useful measurements. Moreover it can fail at cryogenic temperatures. Instead indium foil was finally used for this purpose, onto which the chips were pressed by a spring loaded fixture, see Figure 3.4.

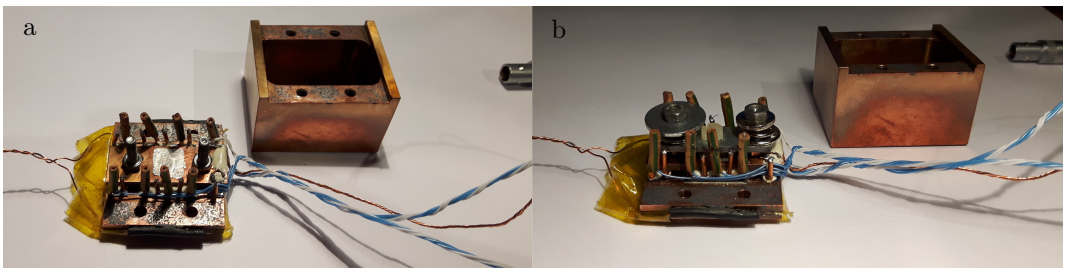

Figure 3.4: Photograph of the measurement device. The sample is placed on the indium foil in the center of the sample holder (a) onto which it is pressed by spring loaded clamps (b) to minimize thermal contact resistance between sample holder and die. The radiation shield on the right-hand side is finally placed over the die and screwed on the base plate.

Apart from numerical studies and comparison to literature the approach was validated

by comparison to measurements on reference samples in case of thermopower. These were deposited together with the studied microdevices, i.e. the reference samples were deposited simultaneously in the same electrochemical cell and at the same potential as the microdevices. For the reference samples the substrate consisted of silicon wafers spin coated with a thin film of PMMA. Gold was sputtered onto these as a seed layer. After electrodeposition pieces of glass slides were glued to the deposit using epoxy. As the adhesion between gold and PMMA is much weaker than the adhesion between epoxy and the sample, the samples could be easily mechanically detached from the substrate. Any residual PMMA was removed with acetone and the seed layer was etched using a potassium iodide solution. Measurements of the thermopower of these samples were performed in a self-built setup and also with a commercial device (Linseis LSR-3). The self-built setup consisted of two resistance wires embedded in two copper block. The temperature of each block was determined by platinum resistance thermometers. Bi-directional temperatures gradients were obtained by applying heating currents to each coil separately. Each end of the reference sample was clamped to one of the blocks and the electrical potential difference measured by thin Cu wires (50 µm diameter) soldered to the samples. As all other measurements, the reference measurements were carried out in vacuum and thermal grease was applied to avoid unwanted temperature gradients between the copper blocks and the sample ends.

3.3 Numerical modeling

Most characterization methods, particularly for microscale samples, are subject to some degree to systematic errors. In this context finite element analysis is a useful tool to estimate the significance of these errors. The modeling efforts, using COMSOL Multiphysics, were based on mimicking as closely as possible the fabricated devices and the measurement process, see Figure 3.5b. The material and dimensional properties were obtained either from the supplier (thickness of wafer and wet thermal oxide), previous measurements (thermoelectric properties and temperature coefficient of resistance of bismuth telluride) and literature (electrical conductivity of gold and specific heat and density of all materials, relevant only for transient studies) or were inferred (thermal conductivity of gold based on the Wiedemann-Franz law). All the material and dimensional properties except for the electrical resistivity of the sample were assumed to be constants. A linear temperature

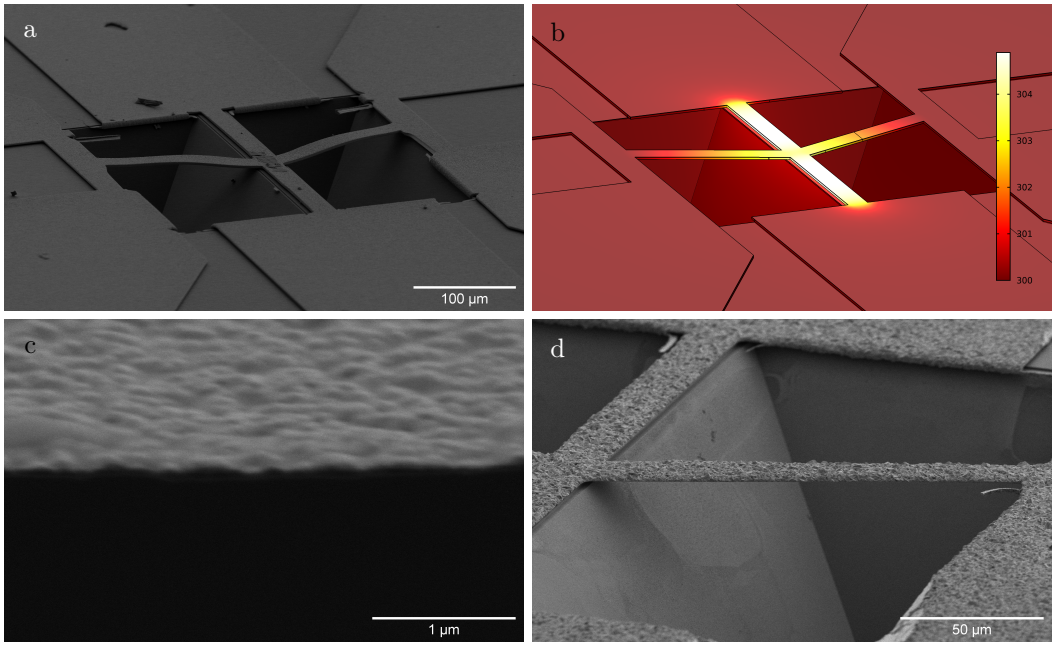

Figure 3.5: SEM image of a completed microdevice with electrodeposited bismuth telluride (a) together with an image of the finite element model (b). The surface temperature in K is indicated by a color map. SEM images of the nickel (c) and bismuth (d) sample are also displayed.

dependence of the electrical resistivity, i.e. $\rho_s(x) = \rho_{s,0}(1 + \alpha(T(x) - T_0))$, was assumed, which is reasonable if the temperature excursions are small. Here α is the temperature coefficient of resistance and $\rho_{s,0}$ the resistivity at T_0 (i.e. the substrate temperature). The potential difference between the ends of the sample was determined as a function of various applied currents through the sample and positive, null and negative heating currents. The value of the heating current was chosen to generate temperature excursions of the junction between sample and electrode of about 5 K (between 100 and 350 mA in magnitude). Other studied parameters included sample properties and also the thickness of the gold and oxide layers. The applied heating current was adjusted as a function of the latter parameters to maintain the temperature excursion at 5 K. Based on the applied currents and the computed voltages the thermoelectric properties of the samples were obtained in the same way as from the measurements, except that means of sweeps performed at positive and negative direct heating currents I_h were computed instead of applying alternating currents. A steady state frequency domain study does not seem feasible since constant currents have to be simultaneously applied and a transient model would significantly increase the computation time.

4 Electrochemical deposition and structural analysis of uniform films

All depositions were carried out in a three-electrode cell with a platinized titanium mesh counter electrode and a 3M Ag/AgCl reference electrode at room temperature in all discussed cases. In case of Bi_2Te_3 the electroplating bath consisted of 10 mM Te(IV), 7.5 mM Bi(III) in 1 M nitric acid as supporting electrolyte [62] and deposition was carried out at 40 mV against 3M Ag/AgCl at room temperature. Bismuth was also deposited from 1 M nitric acid containing 0.1 M Bi(III) [63] and deposition was carried out at $-40\,\mathrm{mV}$ against 3M Ag/AgCl at room temperature. Finally Ni was deposited from a 1.9 M solution of nickel sulfate at $-1\,\mathrm{V}$ against 3M Ag/AgCl at room temperature. The reason for using nickel sulfate instead of nickel sulfamate is that the latter can lead to enhanced co-deposition of sulfur, which reduces internal stress [64] but negatively affects the electrical conductivity of the Ni deposits.

4.1 Electrodeposition of bismuth telluride

In case of bismuth telluride the influence of potential, temperature, concentration and pH on the composition, morphology and texture was studied, mainly by SEM, EDX, XRF and XRD.

As tellurium is more noble than bismuth and thus has a higher standard potential one expects the tellurium content in the deposits to increase for more positive potentials. This was indeed observed (cf. Figure 4.1).

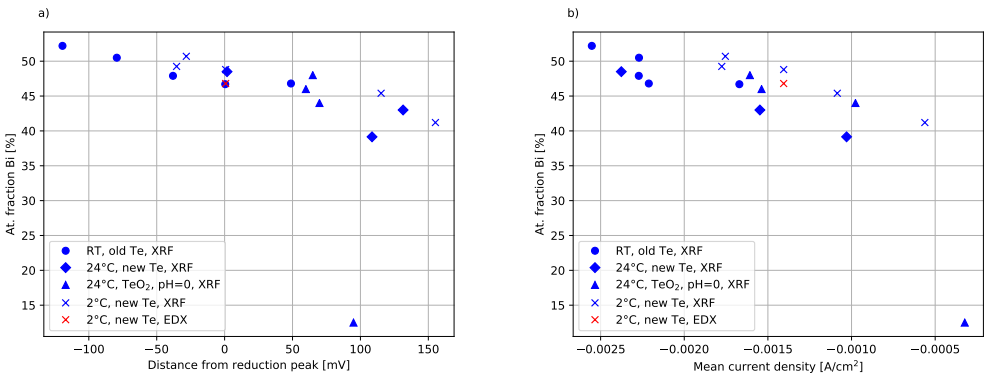

Figure 4.1: The composition of the obtained deposits mainly according to XRF is presented as a function of applied potential (a) and current density (b)

Also at more cathodic potentials the current density increases. At potentials below 0 this causes the morphology of deposits to become increasingly dendritic.

The temperature has a small impact on the composition.

One other observation made is that there is a gradient in the thickness of the deposits based on XRF measurements and SEM cross sections of the deposits. In all cases the films are thicker at the lower end. A selection of the obtained profiles is presented in Figure 4.2. The errorbars in the figure indicate the rms roughness. More cathodic potentials seem to correspond to higher gradients. In the case that cathode and anode are mounted horizontally, this gradient is not observed, as expected, instead ridges arranged in a symmetrical pattern develop. Both observations are explained by the facts that firstly at the low concentrations used the deposition is largely limited by diffusion and secondly natural convection occurs, which can be induced by a change in density of the electrolyte due to depletion of ions and also by gas evolution. Both effects are enhanced at more cathodic potentials due to higher currents and this explains the increase in the gradients.

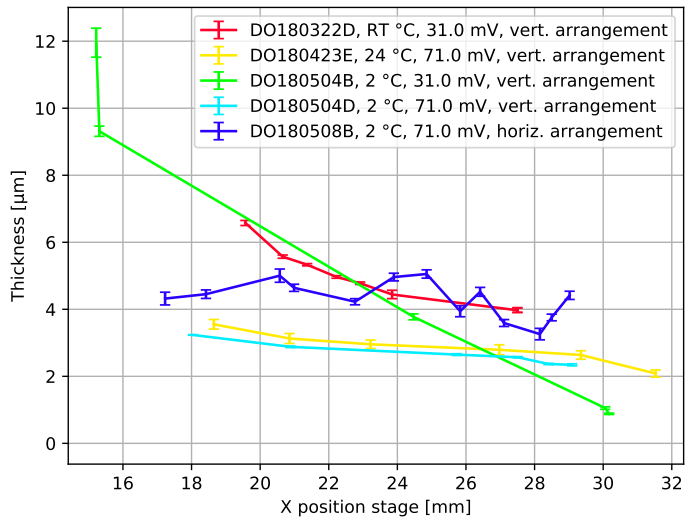

Figure 4.2: Presented are thickness profiles, derived from series of SEM images, of a selection of samples deposited at different potentials, temperatures and in horizontal or vertical electrode configuration.

The current efficiency can be estimated by integrating surface profiles like those in Figure 4.2. The current efficiency for is usually near 100 %, for instance in case of DO180322D, which can be considered a representative sample, 99% is determined when comparing to the

expected thickness at a composition of 45 at. % bismuth.

4.2 Structural analysis by x-ray diffraction

Deposits were further characterized by x-ray diffraction (XRD). X-ray diffractograms of the Bi_2Te_3 reference samples were recorded in the Bragg-Brentano geometry (see Figure 4.5a) using a Bruker D8 Discovery diffractometer. The line width was obtained by fitting Gaussians to the peaks and subtracting the instrumental broadening contribution (obtained from a previous measurement on a corundum sample and also the peak due to the underlying silicon substrate).

The observed peaks were attributed to reflections from bismuth telluride (indicated by dotted gray lines in Figure 4.5), gold, silicon and in case the samples were obtained by galvanic displacement also from Nickel. Fitting Gaussians to the data around peaks, also allows more accurately determining 2θ and the intensity. From the intensities the Harris texture coefficients can be computed, which are a measure of preferred orientation. They are defined as $\mathrm{TC}_{(hkl)} = \frac{I_{(hkl)}/I^0_{(hkl)}}{\frac{1}{N}\Sigma I_{(hkl)}/I^0_{(hkl)}}$, where $I_{(hkl)}$ are the measured intensities and $I^0_{(hkl)}$ those obtained from powder diffraction databases and N the number of peaks considered for the respective sample. Based on the definition the texture coefficient would be equal to 1 for each reflection in a powder sample with no preferred orientation. The maximum value is N in the case that only one of the N considered reflections is observed. The sum of all coefficients always equals N.

One interesting observation with regard to texture is that the (1,1,0) direction is preferential in samples deposited at comparatively high current densities as illustrated in Figure 4.3, which shows the texture coefficient for the (1,1,0) direction as a function of average current density for all electrodeposited samples that were characterized by XRD. All samples deposited at a current density higher than $2\,\mathrm{mA/cm^2}$ have a significant (1,1,0) peak, the only exception is due to a sample deposited under forced convection. The reason is that bismuth telluride is highly anisotropic with regard to electrical and thermal transport. Thus for higher currents orientation in a direction of faster transport is energetically favorable.

Bismuth telluride has a rhombohedral crystal structure with five atoms in one unit cell, the rhombohedral unit cell is however often referred to a hexagonal cell, with lattice parameters

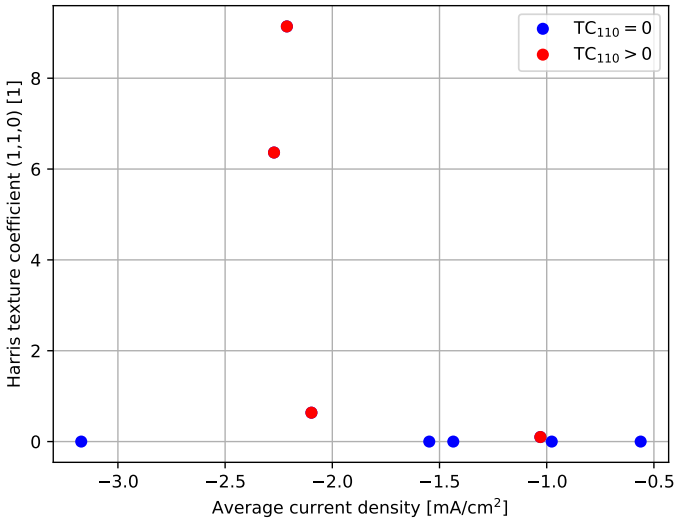

Figure 4.3: Texture Harris coefficient of the (110) reflection as a function of the applied current density. The texture coefficient 0 in spite of a large current density was obtained from a sample deposited under forced convection.

a and c. The angles at which reflections occur are determined only by the unit cell per Bragg's law, their intensity is dependent on the content. Thus a non-linear least squared fit can be carried out to determine the lattice parameters which best match the measurements. In case of hexagonal cells Bragg's law reads $\frac{1}{d} = \sqrt{\frac{4}{3}\left(\frac{h^2+hk+k^2}{a^2}\right) + \frac{l^2}{c^2}} = \frac{2}{\lambda}\sin(\frac{2\theta}{2})$. To avoid unreliable results, cases in which too few or related reflections are present have to be excluded. To avoid only cases of higher order reflections is not sufficient, since $h^2 + hk + k^2$ is invariant under permutation of k and h.

The obtained lattice parameters are shown as a function of the deposition current density in Figure 4.4. The red line indicates the literature values for the lattice constants. A contraction of the c-axis and expansion of the a-axis is expected since $c_{\mathrm{Bi}} < c_{\mathrm{Bi_2Te_3}}$ and $a_{\mathrm{Bi}} > a_{\mathrm{Bi_2Te_3}}$ [65].

From the Scherrer equation $\langle D \rangle = \frac{K\lambda}{\beta\cos(\theta)}$, where $\langle D \rangle$ is the mean domain or crystallite size, K is a constant close to unity, λ is the wavelength, β is the FWHM of the peaks after subtraction of instrumental line broadening and θ is the Bragg angle, an estimation of the minimum crystallite size can be obtained.

The obtained value can only be considered a lower bound of the grain size, since generally line broadening in polycrystalline materials can not only be caused by the limited crystallite

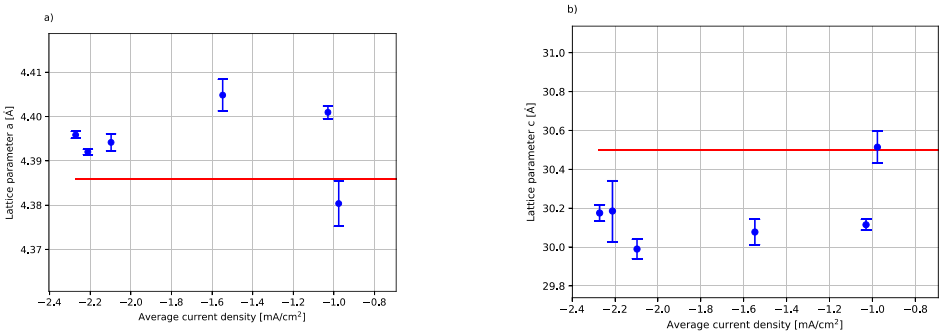

Figure 4.4: Hexagonal lattice parameters obtained from the determined Bragg angles using Bragg's law. (a) shows the a-axis parameter and (b) the c-axis parameter.

size but also non-uniform distortions in the crystal lattice, referred to as microstrain [66, 67]. The Williamson-Hall relation $\beta\cos(\theta) = \frac{\lambda}{\langle D\rangle} + 4\varepsilon\sin(\theta)$ is an expression for line broadening accounting for crystallite size and microstrain, which allows decoupling these contributions. Here β is the line breadth, ε the elastic strain, λ the X-ray wavelength and θ the Bragg angle [67]. So the y-intercept of a plot of $\beta\cos(\theta)$ against $4\sin(\theta)$ should be related to the crystallite size alone. Apparently the grain size is underestimated by a factor of 4 in some cases, i.e. based on single peaks a grain size of 50 nm is determined while it is actually 200 nm. The Williamson-Hall method was applied to study the effect of annealing on the grain size, as discussed in the following.

Indeed significant angular dependence is observed (Figure 4.5b and c), which suggests application of the Williamson-Hall method.

A second observation is the grain growth induced by annealing, in accordance with previous research [68], and a third the difference in grain size between front and back side measurements. The latter refer to spectra obtained on samples after release from the substrate, i.e. in such cases the top surface was in contact with the Au seed layer previously. The CuKα X-rays applied here, with a photon energy of 8.04 keV, have an approximate penetration depth of only 5 µm in Bi_2Te_3 (computed from the X-ray mass attenuation coefficients of the constituent elements), which is not significantly greater than the film thickness (about 2 µm). Therefore inhomogeneities along the growth direction can be expected to cause differences in front and underside spectra. Indeed the spectra from the back side indicate smaller grain sizes, consistent with previous observations on thinner films and SEM cross sections. Based on the weighted linear regression results and the wavelength

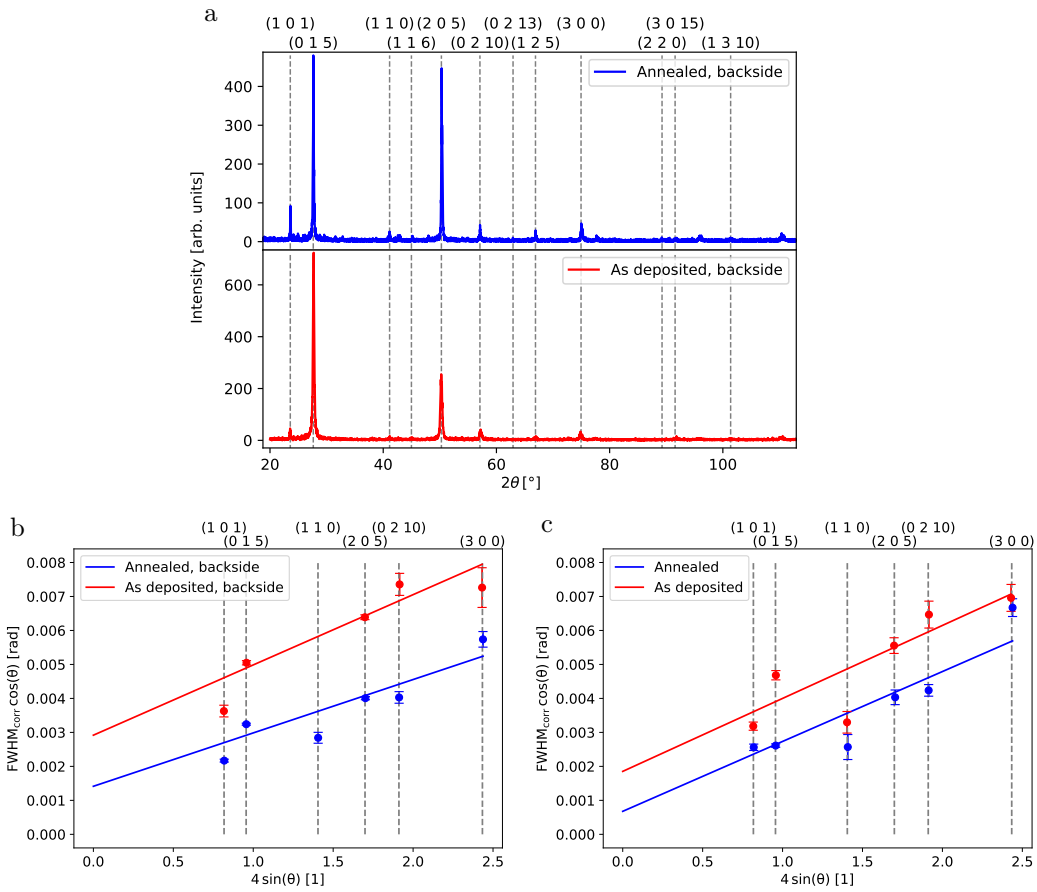

Figure 4.5: The XRD patterns obtained from annealed and as-deposited samples transferred to an electrically insulating substrate (i.e. from the sample's underside) are displayed (a). The Williamson-Hall plots based on XRD patterns of samples transferred to an electrically insulating substrate (b) and untransferred ones (c) both annealed and as deposited. All indices refer to the hexagonal representation of the rhombohedral lattice (based on JCPDS No. 15-0863).

(1.5418 Å) the average domain size can be obtained. For an annealed sample the determined underside and topside grain sizes are 110 ± 46 nm and 228 ± 120 nm respectively and for the as-deposited sample 50 ± 10 nm and 83 ± 40 nm respectively. Thus it can be concluded that the average grain size in the annealed sample lies between 100 and 300 nm.

In conclusion nanocrystalline films of in particular bismuth telluride were routinely deposited from an aqueous electrolyte. At compositions around 40 at. % bismuth a preferred orientation was not observed. Annealing at 215 °C was observed to induce significant grain growth, based on XRD. Effects due to diffusion limited current can be expected, for instance during electroforming or plating on non-planar substrates.

5 Design and improvement of measurement devices for in-plane characterization

5.1 Measurement of the thermoelectric properties by self-heating methods

5.1.1 Feasibility study of in-plane characterization of supported films

With regard to measuring in-plane thermal and potential gradients two cases, namely samples supported by an electrically insulating layer (typically a polymer) and freely suspended samples can be distinguished. Suspended films are usually limited to the microscale due to limited mechanical stability. Supported samples can be advantageous in this regard as millimeter scale samples can be obtained to which structural characterization methods can be applied that are not suitable for microscale samples. The clear disadvantage of a support is that it will contribute to heat transfer, complicating the measurement of the sample's thermal conductivity, particularly in case samples of inherently low thermal conductivity, typical of thermoelectric materials, are studied. To investigate the feasibility of such measurements, the case of supported samples was studied analytically, as explained in the following.

In absence of the thermoelectric effects and external heat sources, the heat equation in steady state reads $\Delta T = -\rho \mathbf{j}^2/\kappa$, at least in an isotropic material. Accounting for the thermoelectric effects one could expect a modification to the equation, however the Peltier effect, manifesting here in changes of the heat flux associated with the electrical current, $ST\mathbf{j}$, is compensated by the Seebeck effect due to which the electric potential changes accordingly. Mathematically $\kappa\Delta T - S\nabla T\mathbf{j} + (\rho\mathbf{j} + S\nabla T)\mathbf{j} = \kappa\Delta T + \rho\mathbf{j}^2 = 0$, provided the Seebeck coefficient is constant. While the steady state heat equation is the same, the thermoelectric effects are accounted for by the boundary conditions.

The case of a thin film (not to scale) attached to an insulating layer supported in turn by a conductive substrate (heat sink) is depicted in Figure 5.1. The problem is treated as two-dimensional, potential and temperature are independent of y. Moreover in case the sample is thin and therefore of high aspect ratio the temperature changes in z-direction within the sample can be ignored. Defining $\theta = T(x, z) - T_0$ as the temperature excursion, where T_0 is the temperature of the heat sink and $\gamma = \frac{\kappa_p}{\kappa\delta}$, the steady state heat equation

then is

$$\begin{aligned} \partial_x^2\theta + \gamma\, \partial_z\theta|_{z=0} &= -\rho \mathbf{j}^2/\kappa \qquad z=0 \\ (\partial_x^2 + \partial_z^2)\theta &= 0 \qquad\qquad z>0. \end{aligned} \tag{4}$$

Here δ and κ_p denote the thickness and thermal conductivity of the supporting layer respectively. The solution was obtained by first determining the solution for $z > 0$ by separation of variables and then exploiting linearity to satisfy the equation for $z = 0$ (the sample plane) by superposition of the solutions for $z > 0$, i.e. the complete solution is a Fourier series. As usual the general solution is obtained by adding to the particular solution the homogeneous ones and the constants are used to match the boundary conditions. The equation for $z > 0$ is solved by linear combinations of $\sinh(\frac{2n\pi}{L}(z-\delta_p))\cos(\frac{2n\pi}{L}x)$ and $\sinh(\frac{2n+1}{L}\pi(z-\delta_p))\sin(\frac{2n+1}{L}\pi x)$, where n is an integer and the sample boundaries are located at $x = \pm L/2$. This ensures that $\partial_x\theta = 0$ at $x = \pm L/2$ and $\theta(x, z = \delta_p) = 0$, i.e. the heat flux out of the left and right boundaries is zero and so is the temperature excursion at the bottom of the insulator. Linear combinations of the first expression can describe symmetric temperature profiles and the latter asymmetric ones. The right-hand side of the equation for $z = 0$ is a constant. A Fourier series approximating a constant $-C$ can be obtained by computing the Fourier coefficients for the function $\frac{LC}{2}(\delta(x-L/2)+\delta(x+L/2))$, where δ here is the Dirac delta distribution. The average of this function over the interval $[-L/2, L/2]$, C, is the first Fourier coefficient and so $C+\sum_{n=1}^{\infty} 2C(-1)^n\cos(\frac{2\pi}{L}nx) = \frac{LC}{2}(\delta(x-L/2)+\delta(x+L/2)) = 0$ nearly everywhere. By inserting $\sum A_n \sinh(\frac{2n\pi}{L}(z-\delta_p))\cos(\frac{2n\pi}{L}x)$ into the equation for $z = 0$ and equating to the Fourier series for the r.h.s. one obtains the particular solution $\theta_p(x,z) = \sum_{n=1}^{\infty} \frac{\frac{2\rho \mathbf{j}^2(-1)^n}{\kappa}\sinh(\frac{2n\pi}{L}(z-\delta_p)\cos(\frac{2n\pi}{L}x)}{\frac{2n\pi}{L}(\frac{2n\pi}{L}\sinh(\frac{2n\pi\delta_p}{L})+\gamma\cosh(\frac{2n\pi\delta_p}{L}))}$. A sanity check can be performed by setting κ_p, the thermal conductivity of the supporting insulator, to 0. In this case the temperature profile for $z = 0$ should be parabolic as it this represents the case of a free-standing sample. Indeed for $z = 0$ and $\kappa_p = 0$ the terms of the series are proportional to $(-1)^n\cos(\frac{2n\pi}{L}x)/n^2$ which is also true for the terms of the Fourier series of x^2, in agreement with expectation. One homogeneous solution immediately follows from the particular one: $\theta_{h,1}(x,z) = \sum_{n=1}^{\infty} \frac{2C(-1)^n\sinh(\frac{2n\pi}{L}(z-\delta_p)\cos(\frac{2n\pi}{L}x)}{\frac{2n\pi}{L}(\frac{2n\pi}{L}\sinh(\frac{2n\pi\delta_p}{L})+\gamma\cosh(\frac{2n\pi\delta_p}{L}))} + \frac{C}{\gamma}(z-\delta_p)$. By a similar approach an other homogeneous solution can be derived based on the asymmetric expression, in this case equating to the Fourier series representing $A(\delta(x-L/2)-\delta(x+L/2))$ produces the second homogeneous solution $\theta_{h,2}(x,z) = \sum_{n=0}^{\infty} \frac{-4A(-1)^n\sinh(\frac{2n+1}{L}\pi(z-\delta_p)\sin(\frac{2n+1}{L}\pi x)}{(2n+1)\kappa\pi(\frac{2n+1}{L}\pi\sinh(\frac{2n+1}{L}\pi\delta_p)+\gamma\cosh(\frac{2n+1}{L}\pi\delta_p))}$ which is

important to account for asymmetries for instance potentially introduced by the Peltier effect. By adjusting these constants arbitrary temperatures at the sample boundaries, θ_l and θ_r, can be achieved. Noting that the boundary temperatures can be expressed as the sum of a symmetric term $\frac{\theta_l+\theta_r}{2}$ and an asymmetric term $\pm\frac{\theta_l-\theta_r}{2}$, the parameter C can be determined as a function of $\theta_l + \theta_r$ and A as one $\theta_l - \theta_r$. The boundary temperatures can be determined by energy balance, considering that the net energy transfer to the sample is zero in steady state and noting that the heat transfer to the heat sink is zero for all the Fourier series, as can be easily shown. The model was validated by comparison to a likewise 2D COMSOL finite element model for a certain set of material and dimensional properties. The analytical and FEM models are in excellent agreement, cf. Figure 5.1b.

The case of a suspended sample that is also supported by a polymer film was also treated by a similar approach as described above. In that case however the second homogeneous solution is simply a constant, as a constant satisfies the zero gradient boundary condition at the lower boundary of the insulator.

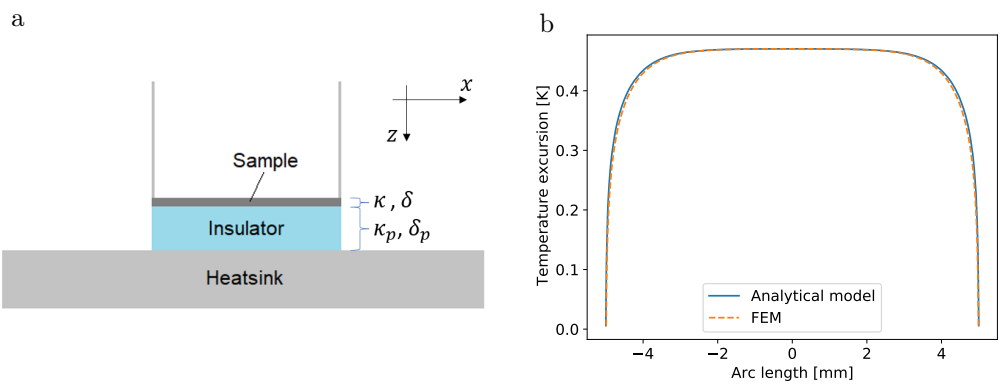

Figure 5.1: Schematic of one of the considered supported sample configurations (a). Comparison of solutions for the temperature profile based on the analytical model and the finite element method for the case of a 0.5 µm thick and 1 cm long sample supported on a 1 mm thick polymer layer (b)

The analytical model can now be used to assess the feasibility of thermal conductivity measurements on supported samples. Assuming an insulating layer of thickness 1 mm and thermal conductivity $0.22\,\mathrm{Wm^{-1}K^{-1}}$, typical of epoxy, the average sample temperature excursion is determined as a function of the sample thermal conductivity. The result for several configuration is displayed in Figure 5.2. In all cases the current through the sample in the model is adjusted such that the temperature excursion for $\kappa_s = 1.5\,\mathrm{Wm^{-1}K^{-1}}$ is

equal to 5 K. For a free-standing sample, $\kappa_p \to 0\,\mathrm{Wm^{-1}K^{-1}}$, the temperature excursion is inversely proportional to the sample thermal conductivity, it is easy to show in this case that $\overline{\Delta T} = \frac{R_s I^2}{12 K_s}$ [57], where R_s and K_s denote the electrical resistance and thermal conductance of the sample respectively, I the applied current and $\overline{\Delta T}$ the average temperature excursion. In all cases a sample of length 1 cm and thickness of 1 µm and a supporting film thickness of 1 mm was assumed. Around $\kappa_s = 1.5\,\mathrm{Wm^{-1}K^{-1}}$ the sensitivity in case of the free-standing sample is $0.31\,\mathrm{K}/0.1\,\mathrm{Wm^{-1}K^{-1}}$. In case of a supported sample with $\kappa_p = 0.22\,\mathrm{Wm^{-1}K^{-1}}$, the sensitivity is only $3\,\mathrm{mK}/0.1\,\mathrm{Wm^{-1}K^{-1}}$. When the supported sample is suspended, the sensitivity considerably increases to $30\,\mathrm{mK}/0.1\,\mathrm{Wm^{-1}K^{-1}}$, but can still be considered insufficient. Obviously deposition of thicker samples or decrease of the supporting film's thickness would result in an increase of the sensitivity, but this at the cost of unreasonable deposition times, particularly in case of nanostructured samples, and a decrease of mechanical stability. These results strongly motivate the measurement of in-plane properties on free-standing samples.

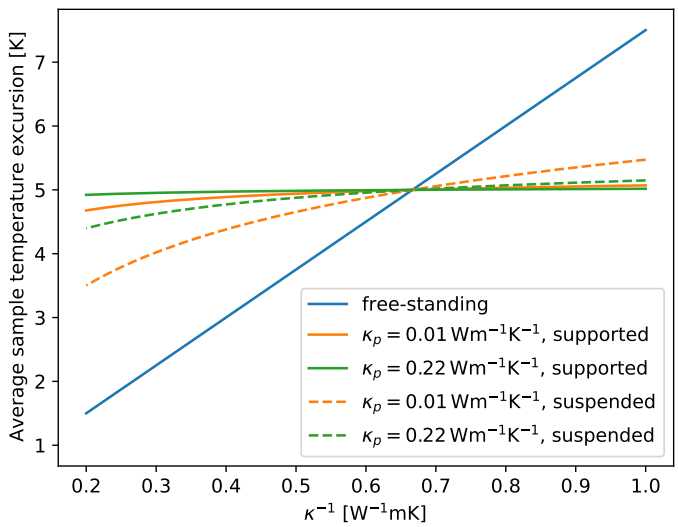

Figure 5.2: The average sample temperature increase is plotted as a function of its inverse thermal conductivity. The slope of this line is related to the sensitivity of the method.

5.1.2 Harman-Cahn measurements

A method of measuring zT was described by Harman and Cahn in 1959 [69]. It relies on the creation of temperature gradients in thermoelectrically inhomogeneous circuits to which a DC current is applied. In homogeneous materials, i.e. a circuit consisting only of a homogeneous semiconductor, one expects the usual symmetric parabolic temperature profile along the conductor caused by Joule heating, assuming that source and sink are at the same temperature, even when the Seebeck coefficient is considerable. This is because the Peltier effect is canceled by the increase in potential due to the Seebeck effect, as was pointed out above. However when the Seebeck coefficient changes significantly between source and sink, the Peltier effect becomes noticeable by a strong dependence of the temperature profile on the direction of the current. The temperature profile within each segment is still parabolic, but the inhomogeneity causes the profile along the sample to be asymmetric. This can be exploited to determine the figure of merit, as discussed in the following. The case of significantly different Seebeck coefficients between sample and probe is the typical one, since metals, which the probe is made of, have Seebeck coefficients on the order of a few μV/K while samples of interest for thermoelectric applications have Seebeck coefficients at least one order of magnitude greater.

Assuming that electrical and thermal transport are one-dimensional, a simple model for the system can be derived by solving the one-dimensional steady state heat transfer equation taking into account the Peltier effect by adjusting the boundary conditions. This assumption is typically incorrect at the junction between lead and sample, as the sample is usually wider than the probe and thus some spreading out of the current has to occur in the sample, which contributes to the electrical and thermal resistance. The shorter the sample the greater the relative error due to this effect. One way to mitigate it is to metallize the top surface of the sample.

Harman and Cahn do not point this out, but one additional condition for the validity of the expression they derive is that the two leads have equal thermal and electrical conductance (see Figure 5.3).

Under this condition the expression

$$I(S_s - S_l)\bar{T} = (K_l/2 + K_s)\Delta T \tag{5}$$

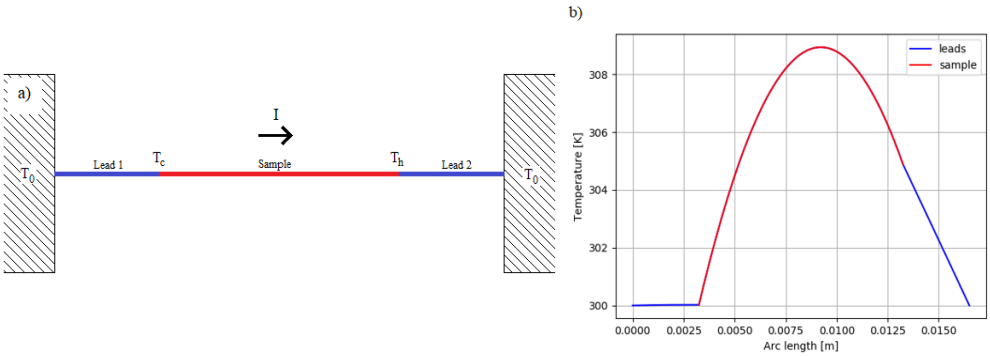

Figure 5.3: (a) Sketch of the setup analyzed by Harman and Cahn. Their results are accurate under the condition that Lead 1 and 2 are thermoelectrically equal. Subscripts c and h represent cold and hot junctions respectively. (b) Exemplary temperature profile that might be observed in case of positive Ss and current direction as in (a), assuming that the leads have a negligible Seebeck coefficient.

holds, where $\bar{T} = \frac{T_h+T_c}{2}$, $\Delta T = T_h - T_c$. From this, ignoring the leads' thermal conductance and Seebeck coefficient one obtains $\Delta T = \frac{S_s I \bar{T}}{K_s}$. The potential difference between the ends of the sample is given by the sum of the typical Ohmic contribution $V_R = -R_s I$ and the Seebeck voltage $V_s = -S_s \Delta T$ and with this $\frac{V_s}{V_R} = \frac{S_s \Delta T}{R_s I} = \frac{S_s^2 \bar{T}}{R_s K_s} = z\bar{T}$. If additionally the temperature at both ends of the sample is determined, the sample is fully characterized under this assumption since $S_s = -V_s/\Delta T$, $R_s = -V_R/I$ and $K_s = \frac{-IV_s\bar{T}}{\Delta T^2}$.

The measurement of the sample's thermopower in this manner can be regarded as accurate, inaccuracies could only be caused by thermal interfacial resistance between the thermometers and the sample. The same is true with regard to R_s. Determining $K_s$in this way can be expected to be more inaccurate however since K_l can be comparable to K_s when samples have microscale thickness. There is however an other way to determine K_s based on using the sample itself as a resistance thermometer, as stated above.

The temperature profile within the sample is parabolic such that it can be expressed as $T_s(x) = \frac{-R_s I^2}{2K_s L_s^2}x^2 + Ax + B$, where A and B depend on the material parameters and L_s is the length of the sample. If one defines the center of the sample as the origin, i.e. the sample ends are located at $x = L_s/2$ and $x = -L_s/2$, A is equal to zero if $S_s = S_l$ assuming again that the leads have equal thermal and electrical conductance. This means that as stated above asymmetry can only be introduced by inhomogeneity of the thermopower. The mean temperature $\langle T_s \rangle$ which the resistance depends on, is equal to $-\frac{R_s I^2}{24K_s} + B$. Since $T_s(L_s/2) + T_s(-L_s/2) = -\frac{R_s I^2}{4K_s} + 2B$ one can show that $\frac{R_s I^2}{12K_s} = \langle T_s \rangle - \frac{T_s(L_s/2)+T_s(-L_s/2)}{2}$

and thus K_s can be determined, as all other quantities are measured.

A third way of determining K_s is to use the the resistance thermometers as heaters simultaneously. This technique was first used to measure the thermal conductance of carbon nanotubes with a suspended microchip device [52].

While suspending samples has the advantage of avoiding the influence of the substrate, heat transfer by radiation can have a significant influence at lower temperatures than one would expect. This happens in case of samples of low conductance that are supported only at both ends. In this case heat transfer by radiation from the heated sample to the surrounding walls of the vacuum chamber at ambient temperature competes with conduction from the ends of the sample leading to significant temperature changes along the sample even when no current is applied through it (see Figure 5.4c). This effect can be avoided by placing a radiation shield thermally anchored to the heated substrate around the sample. In this case the net heat transfer by radiation from the sample is 0, since the surrounding material is at the same temperature.

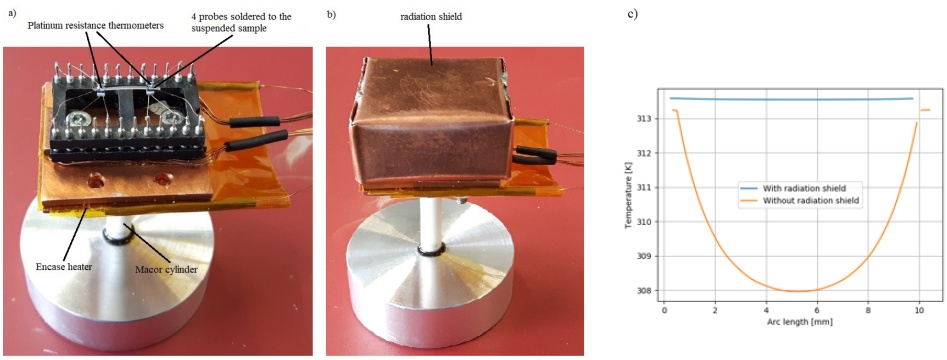

Figure 5.4: (a) Developed measurement setup with a ca. 30 µm thick sample mounted on suspended platinum resistance thermometers. Electrical four point contact to the sample was established by soldering copper wires to the ends. (b) A radiation shield thermally anchored to the heater is designed to avoid the temperature excursions displayed in (c) which are based on FEM results.

Suspending samples was achieved by gluing them to glass slides with nail polish and subsequent mechanical delamination. The nail polish was then dissolved in acetone. Removal of the Si substrate by wet etching with a KOH solution had to be avoided since it affected the samples. A lift-off technique could also be applied, i.e. using a metallized layer of resist as a substrate.

5.1.3 Cross-plane transport

The case outlined above can not easily be achieved in the cross-plane direction. Instead the sketch in Figure 5.5 describes the case that is commonly encountered with samples on the microscale. Instead of being suspended between two leads, the sample is mounted on a grounded heat sink and a probe serves as the lead.

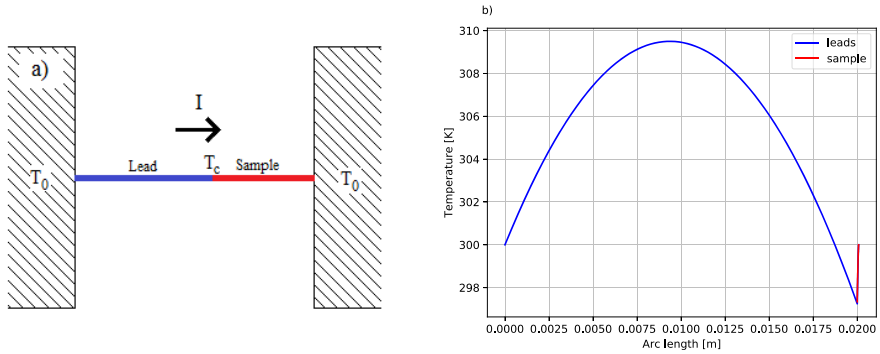

Figure 5.5: Sketch of the case encountered experimentally in the cross-plane case.

In this case Equation 5 is not valid. One can easily see this by noticing that Equation 5 implies that ΔT is zero if $S_s = S_l$ irrespective of the current. This is because in the symmetric case heat transferred to the sample from either lead is equal. In the case illustrated in Figure 5.5 Joule heating alone would cause a temperature difference, even if $S_s = S_l$. This implies that more care has to be taken in obtaining the figure of merit from measurements.

In order to achieve a reliable measurement of the Seebeck voltage, i.e. a large enough signal to noise ratio, the difference in temperature between the ends of the sample should be at least on the order of 0.1 K. Assuming a Seebeck coefficient around 100 μV/K the Seebeck voltage is then around 10 μV. This places certain constraints on the setup. One can show that the temperature difference between the ends of the sample is given by

$$\Delta T(I) = \frac{-I^2(R_l + R_s)/2 + I(S_s - S_l)T_0}{K_l + K_s + I(S_s - S_l)}. \tag{6}$$

The first term of the numerator is caused by Joule heating and if it dominates the second, the figure of merit can not easily be obtained since then $V_s \propto S_s$ and not S_s^2 as required. This means that the electrical resistance of the lead should be minimized. On the other hand K_l, the thermal conductance of the lead is assumed to be negligible compared to that

of K_s. Minimizing simultaneously K_l and R_l requires a trade off since for metals $K_l R_l$ is constant according to the Wiedemann-Franz law.

The upper bound on the current I in turn also places a lower bound on the sample height, since, as the height decreases, higher currents have to be applied to achieve the same ΔT.

If the temperature at the ends of the sample is measured, the constraints mentioned above could be lifted by deliberately making the first term dominate. In this case direct determination of zT from the measured voltages is not possible, however all three properties could be determined independently. To eliminate the terms depending on I and AC current could be applied.

In any case too high heat fluxes through the sample have to be avoided, since the substrate is assumed to be isothermal, and this assumption can be violated as the substrate's thermal conductivity is finite. The schematic Figure 5.6a more accurately depicts the actual situation, the substrate's final th. conductivity is accounted for by a series resistance. The heat flux through the sample is approximately $P \approx K_s(T_h - T_c)$ and thus $T_c - T_0 \approx P\,R_{sub} = \frac{K_s(T_h-T_c)}{4\kappa_{sub} r_s} = \frac{\kappa_s \pi r_s (T_h - T_c)}{4\kappa_{sub} L_s}$, where r_s is the sample radius. Figure 5.6b shows $T_c - T_0$, which is the difference of the temperature directly below the sample and that of the substrate far away from it, as a function of the sample diameter, assuming $T_h - T_c = 2\mathrm{K}$, $\kappa_s = 2\,\mathrm{Wm^{-1}K^{-1}}$, $\kappa_{sub} = 150\,\mathrm{Wm^{-1}K^{-1}}$ and $L_s = 80\,\mu\mathrm{m}$. To keep the relative error in the temperature difference along the sample below 5% a sample diameter less than 1 mm would be required under these conditions, at least in case the temperature T_0 is determined at a significant distance from the sample itself (compared to the diameter).

A final restriction is placed on the diameter of the samples by the requirement that the probe might have to be placed on the sample by bare eye and especially when two probes are used the sample area can not be smaller than the contact area required for two probes. If the temperature of the top surface is to be determined, an accordingly larger area is needed.

It has to also be considered that a deviation in the diameter of the lead and the sample will cause a deviation from the one dimensional model. A layer of high thermal and electrical conductivity deposited on the actual sample can alleviate this effect. In order to study the impact of a deviation from a 1D-geometry, finite element analysis of a rotationally symmetric setup was performed. In the studied case a deviation of only 3 % between the 3D and 1D cases was found.

In case of cross-plane measurements an additional concern is the potentially large influence

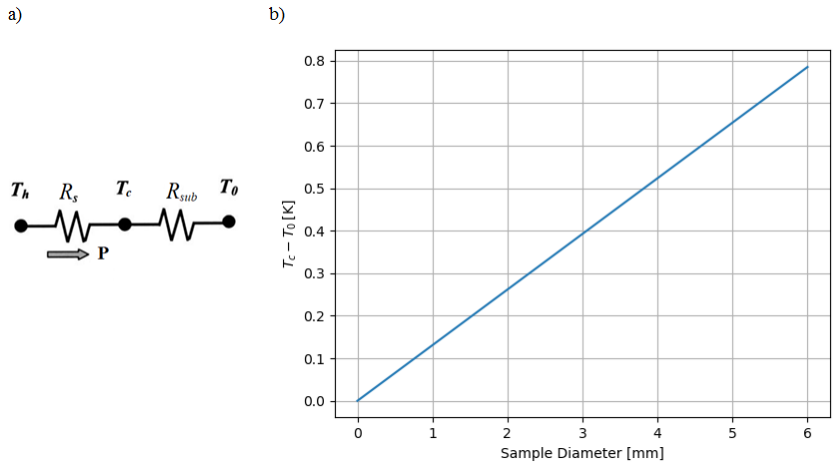

Figure 5.6: (a) Thermal resistance model accounting for the non-zero thermal resistance of the substrate. (b) Temperature excursion from the bulk of the substrate as a function of sample diameter

of spreading resistance, even when the potential is measured close to the sample [70].

This influence of spreading resistance could be countered by using more electrically conductive substrates, but can more effectively be avoided even in case of conventional metallized Si wafers by patterning the metal film as indicated in Figure 5.7. The underlying silicon is at least 4 orders of magnitude less electrically conductive than the gold film. Moreover it is separated from the metal by a thin layer of native oxide. Thus most of the current through the sample will flow through the metal, if it is grounded. By connecting the metal strip supporting the sample to ground at both ends, the current flowing in between the two branches of the sample is negligible. Therefore effectively a pseudo-4-probe measurement of the sample resistance can be carried out. The sample width of 1.5 mm and the gap of equal size between the two branches make the temperature measurement of the top electrode feasible. The additional benefit of using micropillar arrays is that it addresses the need to restrict the sample cross section to avoid the temperature measurement errors mentioned above.

The measurement is carried out by first applying an AC current at frequencies significantly higher than the thermal time constant. In this case the AC voltage is due to the Ohmic contribution, while a DC offset is due to the Seebeck effect according to $V = R_s I - S_s \Delta T$, thus by applying alternating currents both contribution can be decoupled. Apart from this approach thermovoltage and Ohmic contribution can once again also be decoupled by

measuring the transient response, i.e. the voltage after the DC current through the sample is interrupted. It should also be noted that the need to directly measure the temperature by placement of a sensor on the top electrode can be circumvented by again using the sample itself as a resistance thermometer.

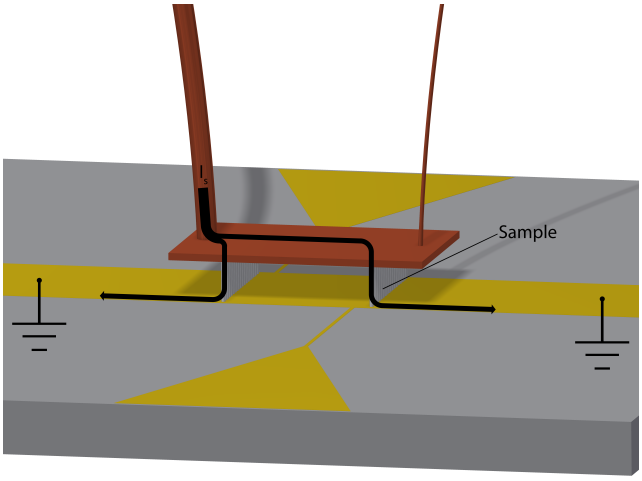

Figure 5.7: Schematic of proposed cross-plane devices for the measurement of thermoelectric properties (a), the thickness of the sample is exaggerated for clarity. Not shown is the thermometer used to measure the temperature of the top side of the electrode.

The accuracy of the method was again verified by mimicking the measurement process using finite element modeling.

5.2 First attempts on large suspended samples

The configuration of a sample suspended between two PRTs is not only interesting because it allows for accurate and comprehensive thermoelectric characterization, as already stated above, but also because various slightly differing methods can be used to determine the measurands. In particular the Seebeck coefficient can be measured firstly by exploiting the Peltier effect, which is the Harman method, and also by using one of the PRTs as a heater while recording the open circuit voltage. The thermal conductivity can be derived from the same measurement, specifically from the temperature increases of both PRTs when one is used as a heater. The other is to use the sample itself as a resistance thermometer to determine the average temperature increase of the sample due to Joule heating. Applying both methods in both cases allows for cross-checking which increases confidence in the

results. As has been discussed above the relative significance of radiative heat transfer increases with the sample length. A radiation shield at the substrate temperature can make radiation negligible in many cases. But at sample lengths of several mm and a thickness of 20 µm, radiation can have an impact even at relatively small temperature excursions of a few degrees. It was indeed found that radiation has to be accounted for even when a radiation shield is used and thus a method to account for it was devised.

The steady state heat transfer equation including radiation is $-\kappa\partial_x^2 T(x) + 2\sigma\epsilon(t^{-1} + w^{-1})(T(x)^4 - T_{env}^4) = P/V$. Since this equation can not be easily solved analytically, the radiation term can be approximated by Taylor expansion to first order assuming small deviation from T_{env}, i.e. $2\sigma\epsilon(t^{-1}+w^{-1})(T(x)^4 - T_{env}^4) \approx 8\sigma\epsilon(t^{-1}+w^{-1})T_{env}^3(T(x) - T_{env})$ [69, 56]. With this approximation and defining again $\theta = T - T_{env}$ and $\gamma^2 = 8\frac{\sigma}{\kappa}\epsilon(t^{-1} + w^{-1})T_{env}^3$, the equation reads $-\partial_x^2\theta + \gamma^2\theta = \frac{P}{\kappa V}$. The solution is $A\sinh(\gamma x) + B\cosh(\gamma x) + \frac{P}{\gamma^2\kappa V}$, where A and B are constants. By enforcing Dirichlet boundary conditions, i.e. the temperatures θ_l and θ_r at the sample boundaries $-L/2$ and $L/2$ respectively, $A = \frac{\theta_r - \theta_l}{2\sinh(\gamma L/2)}$ and $B = \frac{\theta_l + \theta_r - \frac{2P}{\gamma^2\kappa V}}{2\cosh(\gamma L/2)}$. The average temperature can now be computed by integration:

$$\bar{\theta} = \frac{1}{L}\int_{-L/2}^{L/2} \theta(x)\mathrm{d}x = \frac{(\theta_l + \theta_r)/2\tanh(\gamma L/2)}{\gamma L/2} + (1 - \frac{\tanh(\gamma L/2)}{\gamma L/2})\frac{P}{\gamma^2 L^2 K_s} \tag{7}$$

In the limit $\gamma \to 0$, in which radiation is insignificant, $\bar{\theta} = \frac{\theta_l + \theta_r}{2} + \frac{P}{12K_s}$, as expected. Based on Equation (7) the following approach can be taken to account for radiation and retrieve the sample's thermal conductance K_s: First both PRTs can be used as heaters while the electrical resistance change of the sample is monitored without significant Joule heating. In that case $P = 0$ and γL can be obtained from the measured temperatures by solving the transcendental equation $\frac{\tanh(x)}{x} = \frac{2\bar{\theta}}{\theta_l + \theta_r}$ numerically. After this the slope of the temperature - heating power line can be determined from which together with γL the thermal conductance can be derived (see Figure 5.10a).

The thermal conductance can also be obtained by using one of the PRTs as a heater and measuring the temperature increase with both PRTs, as mentioned earlier. One of the assumptions, namely that the combined thermal conductance of the supporting wires is the same for both PRTs, can be avoided by performing two measurements for which the heated sides are alternated. Particularly $K_b^l = \frac{P_a\theta_r^b - P_b\theta_r^a}{\theta_r^b\theta_l^a - \theta_r^a\theta_l^b}$ and $K_b^r = \frac{P_b\theta_l^a - P_a\theta_l^b}{\theta_r^b\theta_l^a - \theta_r^a\theta_l^b}$ where the super- or

subscripts a and b denote the case in which the left and right PRT are heated respectively, and the super- or subscripts l and r denote the left and right PRT respectively. In the case that radiation is insignificant $K_s^a = \frac{K_b^r \theta_r^a}{\theta_l^a - \theta_r^a}$ and if the right PRT is heated $K_s^b = \frac{K_b^l \theta_l^b}{\theta_r^b - \theta_l^b}$. When radiation has to be considered the corrected expression for the sample's thermal conductance can be determined by obtaining the heat flux into the sensing PRT from the derivative of Equation (7) at the sample boundaries. In that case $K_{s,corr}^a = \frac{K_b^r \theta_r^a \sinh(\gamma L)}{\gamma L(\theta_l^a - \theta_r^a \cosh(\gamma L))}$.

Part of the measurement setup is displayed in Figure 5.8. Heating and readout of the PRTs is performed by a National Instruments 4 channel universal analog input module (NI-9219) and an analog 4 channel voltage output module (NI-9263), possessing a 24 bit analog to digital converter (ADC) for varying voltage input ranges and a 16 bit DAC for a range of ±10 V respectively. The NI-9219 allows using a single channel for PRT temperature measurement and this is indeed used to measure the temperature of a third PRT mounted on the sample holder. However the applied current is immutably set to 0.5 mA in this case, which suspended and in vacuum would cause significant self-heating of several degrees K. Instead an external voltage source (the NI-9263) is used as the current source. A 10 kΩ resistor is placed in series with both 1 kΩ PRTs. Measuring the current by measuring the voltage across a large resistance enhances the signal to noise ratio even when currents on the order of 50 µA are applied. Moreover the maximum output current that can be supplied by a single channel of the NI-9263 can still be achieved at this load by applying the maximum voltage (10 V). The larger voltages that need to be applied due to the considerable load further reduce the signal to noise ratio.

Applying a current of 1 mA to the PRT results in a temperature increase of about 5 K. This was only the cases after phosphor-bronze wire (an alloy containing mostly 95 % copper and 5 % tin) of 50 µm were used as the leads. Phosphor-bronze has an about 8 times smaller thermal conductivity than copper, which means that the temperature excursion would be 8 times smaller if copper wires of equal diameter were used, which would make the temperature excursion on the sensing side undetectably small.

The thermal conductance measurement results for the supports and also the sample as a function of temperature are displayed in Figure 5.9. Part of the raw data these values are based on is displayed in Figure 5.10c. The red and green curves are the PRT temperatures as a function of time when the left one (red curve) is used as a heater. The blue curve is the simultaneously measured open circuit voltage across the sample, i.e. the Seebeck voltage.

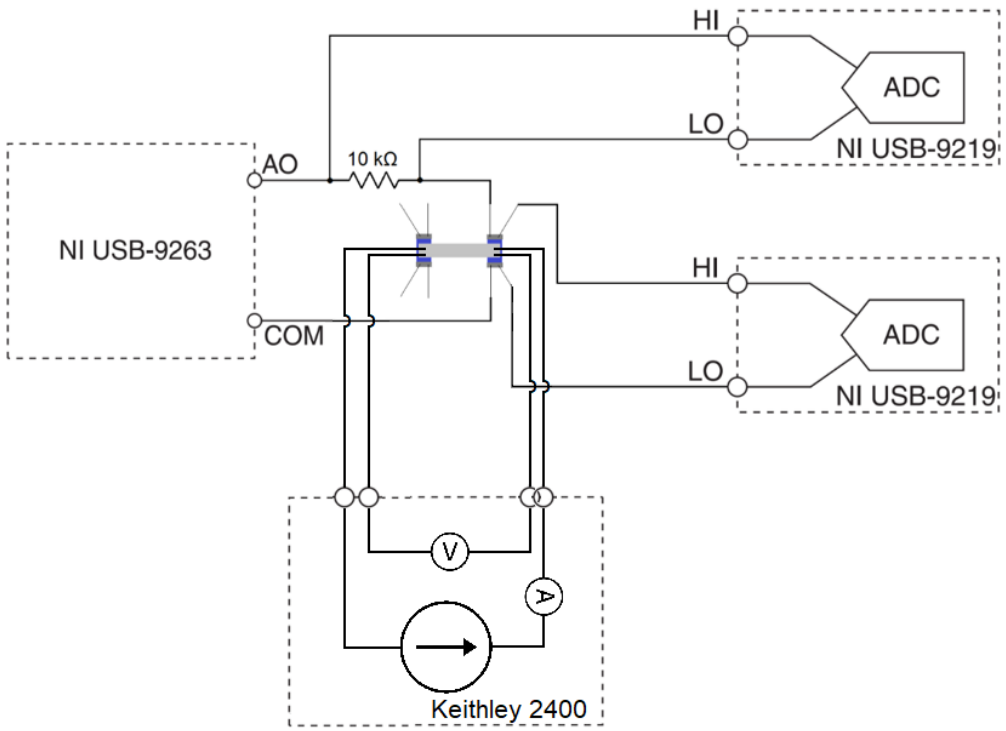

Figure 5.8: Schematic of the measurement setup for samples suspended between PRTs.

The conductance of the supporting wires is nearly two times greater than would be expected based on the calculated thermal conductance of the wires. With a thermal conductivity of Cu95/Sn5 of about 100 $\mathrm{Wm^{-1}K^{-1}}$ at 310 K one can estimate 100 µW/K per PRT, while about 180 µW/K are measured. This can once again be traced to thermal radiation. Based on the dimensions of the used PRT and assuming an emissivity of 1 one obtains 100 µW/K at an environmental temperature of 310 K. This considerable contribution of radiation to heat transfer should not impact the accuracy, provided the linearization of the radiative heat transfer is valid, which is true for sufficiently small temperature excursions. Excursions of 5 K were maintained in the present case.

The electrical resistance is measured by applying alternating currents to avoid a temperature difference due to the Peltier effect. To measure the thermopower a temperature gradient needs to be applied and this was achieved by applying one of the PRTs as a heater (see Figure 5.10c) and also by using the Peltier effect (Figure 5.10b).

Figure 5.10 partially illustrates the other employed measurement methods. The obtained material properties are displayed as a function of temperature in Figure 5.11. It should be

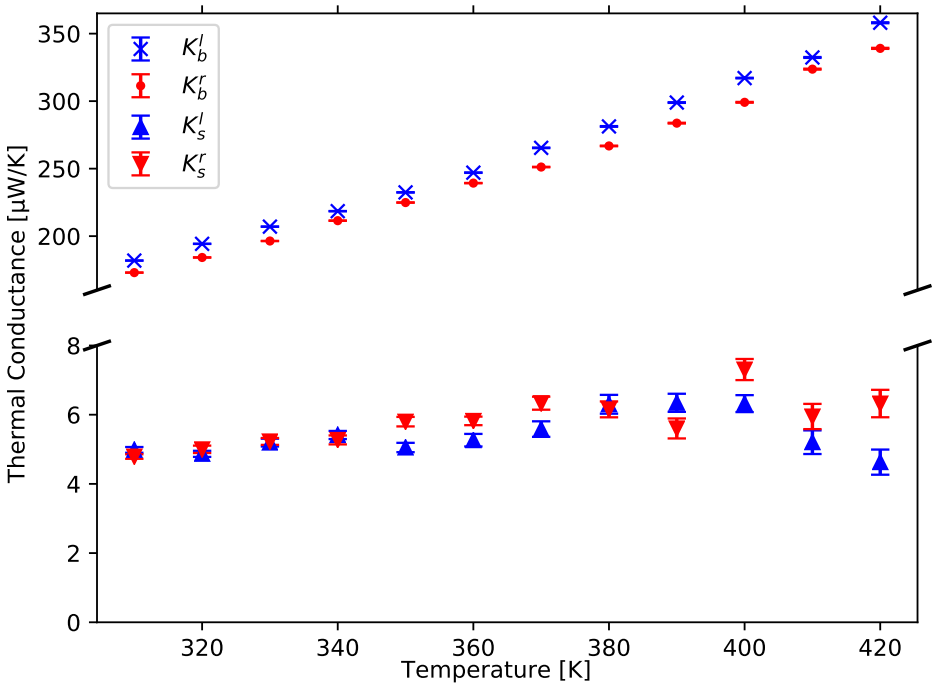

Figure 5.9: Measured thermal conductance of the wires supporting the left and right half of the wires supporting the suspended setup, according to the superscripts, and the thermal conductance of the sample.

noted that most of the presented results are derived from the second set of measurements on the same sample. During the first measurement a more pronounced increase of the electrical conductivity beyond 400 K was observed (see Figure 5.11a). At 300 K the electrical conductivity was 28700 S/m during the first measurement, which indicates that an irreversible increase of the electrical conductivity occurred during the first measurement. This is most likely explained by the onset of annealing effects. It can be considered surprising that a temperature of only 150 °C induces significant changes, but this is in agreement with literature [39]. Remarkably the Seebeck coefficient was barely affected, it increased by about 2 μV/K. The electrical conductivity increase could be caused by an increase of charge carrier mobility or density. The latter is known to be linked with a decrease of the thermopower, while the impact of mobility on the thermopower is not as straightforward. Thus it can be concluded that the observed conductivity increase was mainly caused by an increases of charge carrier mobility. Apparently steady state was not reached during the first

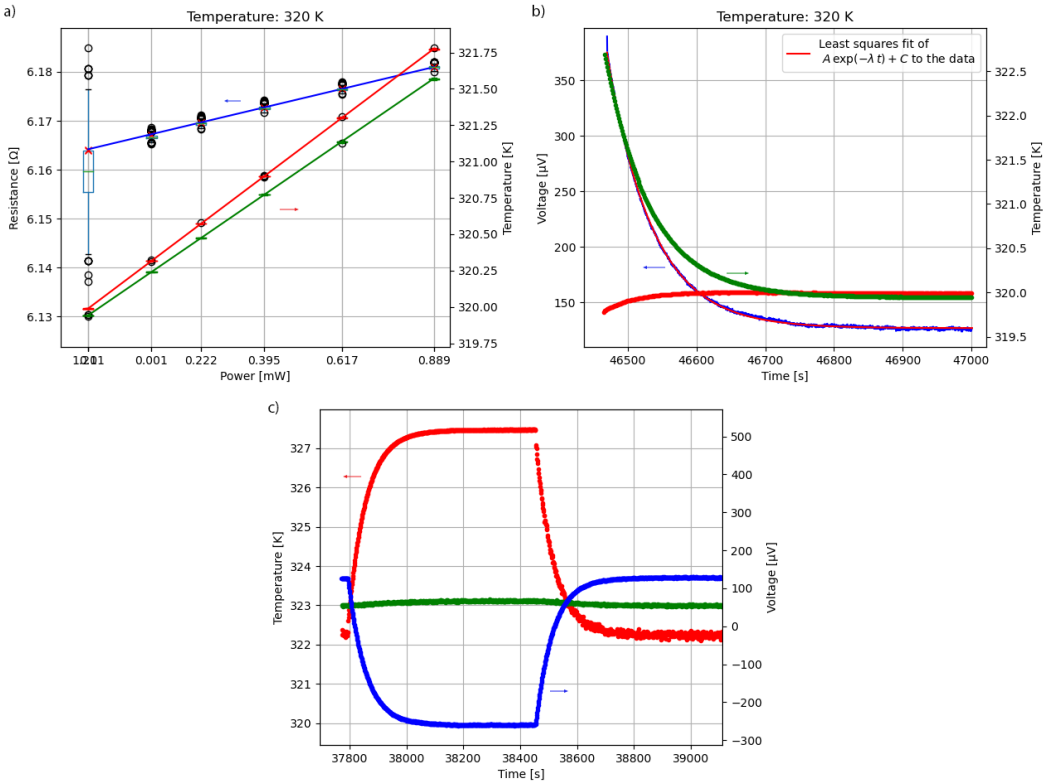

Figure 5.10: a) The measured temperatures and sample resistance as a function of the alternating current applied through the sample. b) The transient response of the system, i.e. again temperatures and voltage, after interrupting the DC-current are plotted. The voltage is related to the temperature by the Seebeck effect, c) The second method of measuring the thermopower is to us one of the PRTs as a heater and measure the induced voltage along the sample (the open circuit potential).

measurement, since further conductivity drift was observed during the second measurement, which is mainly responsible for the enhanced errorbars beyond 400 K.

The thermopower measurements based on either method of generating the temperature gradients, i.e. via the Peltier effect or by simply applying a DC current and using one of the PRTs as a heater are in excellent agreement, which increases confidence in the accuracy. Based on XRF measurements the sample had a bismuth content of 45 at%. Results in literature on the bismuth content at which the transition from n- to p-type conduction occurs are conflicting. Generally investigation of samples obtained by solid state reaction at relatively low temperatures and also by molecular beam epitaxy indicates that the transition occurs at around 60 at% bismuth [65, 71]. Conflicting results are partially attributed to the occurrence of mixed phases.

The relatively low thermopower of $-80\,\mu\mathrm{V/K}$ at room temperature is in agreement with two possible Fermi levels, namely close to the center of the band gap or in the highly degenerate regime [10, 12]. A mid-gap Fermi level is unlikely as an order of magnitude lower conductivity would be expected in this case. The low figure of merit is caused by the low power factor, which is in agreement with results reported for as-deposited samples. Annealing is expected to significantly increase the conversion efficiency.

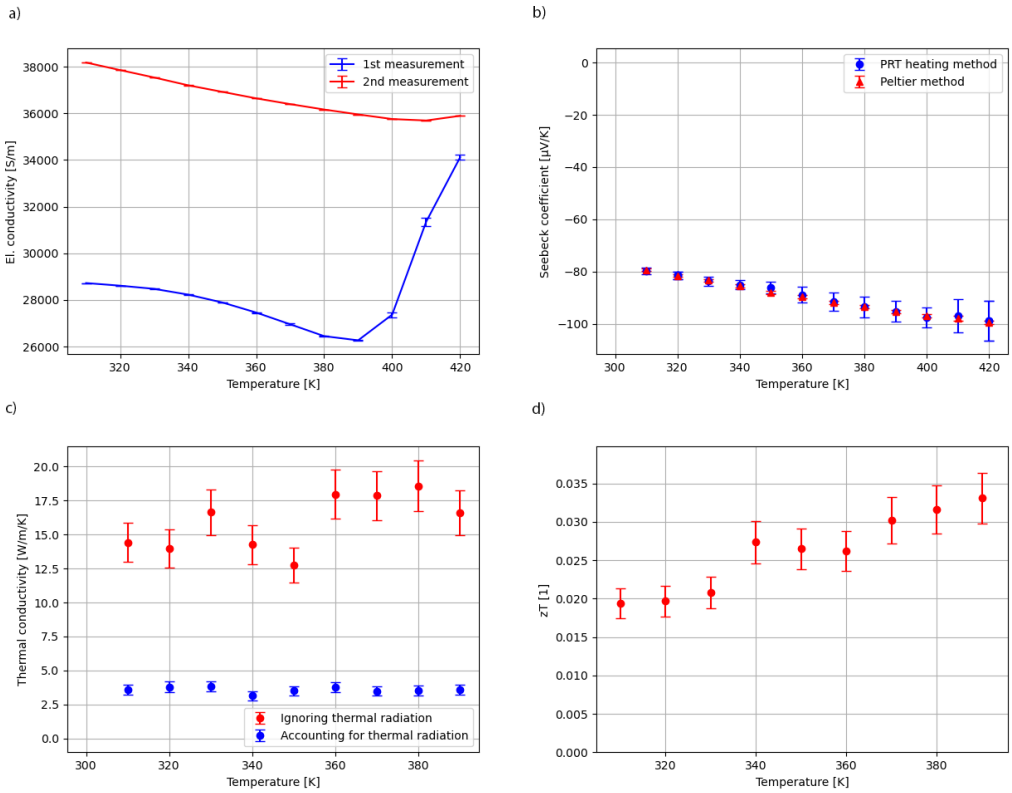

Figure 5.11: a) The measured electrical conductivity is plotted as a function of the substrate temperature. b) The thermopower as a function of temperature by both of the measurement methods. c) The determined thermal conductivity as a function of temperature with and without correction for radiation flux. d) The obtained figure of merit.

5.3 First application of microdevices

The idea of the approach is to expand the self-heating method for measuring not only the thermal and electrical conductance but also the thermopower of suspended samples. This method, briefly described above, exploits the temperature dependence of the sample's electrical resistance. The measurement of thermopower requires generating temperature

differences between electrodes contacting the sample. As depicted in Figure 5.12a, the device

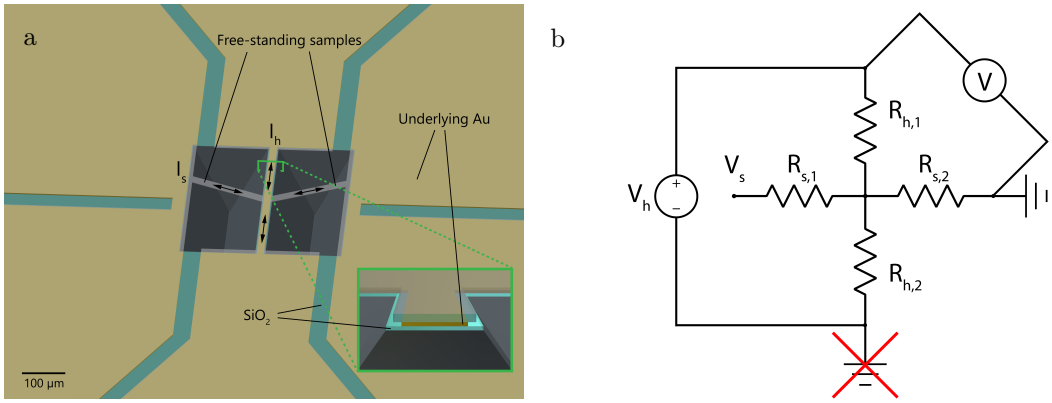

Figure 5.12: Schematic of the device for the in-plane measurement of thermoelectric properties (a). The inset is a close-up of a cross-section view of the supported central electrode. (b) Equivalent circuit of the device modeling the electrical properties including the voltage sources. The heating current source is assumed to be isolated from ground.

consists of a suspended electrodeposited sample supported at its center by an electrode, consisting of gold underlying the electrodeposited film. The electrode itself is supported by a thin film of silicon oxide (about 1 µm thick) and silicon. Anisotropic silicon etching is applied to fabricate this partially suspended and supported structure. Since the central electrode is supported by silicon, acting as a heat sink, even application of currents through the suspended samples that cause its average temperature to increase significantly, has no significant effect on the temperature of the supported central segment. By applying currents at least two orders of magnitude higher than the sample currents through the central electrode, referred to as heating current in the following, temperature excursions in the central segment can be generated. Therefore, by design of the device, the temperature of the central segment can be controlled by the current through the central electrode, irrespective of the sample current. So in a first measurement, applying no heating current to the central electrode, the electrical and thermal conductance are determined as follows.

The electrical conductance is determined by measurement of the differential resistance, i.e. the slope of V-I curves for small sample current excursions to avoid Joule heating. The current range is adjusted based on the sample properties, but generally does not exceed 100 µA.

The thermal conductance is obtained by measuring the static electrical resistance of the sample as a function of the power P dissipated in the sample (the product of the voltage

and the applied DC current). In this case an order of magnitude greater sample currents are applied. In a sample of uniform composition and cross section Joule heating leads to a parabolic temperature profile if conduction is the only mode of heat transfer. If the ends of the sample are connected to a heat sink one can show that $\overline{\Delta T_s} = \frac{P}{12K_s}$ where K_s denotes the thermal conductance of the sample [57] and $\overline{\Delta T_s}$ the average temperature excursion. The average temperature increase in each branch is derived from its electrical resistance increase. This is accomplished by performing measurements at a range of substrate temperatures. A forth order polynomial is fitted to the resistance-temperature data, which is numerically inverted to obtain the average temperature as a function of the electrical resistance.

In a second step the thermopower is determined in the following manner. The central electrode is heated to create a temperature difference between the center and ends of the suspended sample. The thermopower S is the voltage induced by the Seebeck effect divided by this temperature difference, i.e. $S = -\Delta V/\Delta T$. This means that electric potential and temperature differences between the central segment and the ends have to be measured.

The temperature increase of the central supported segment of the sample is again determined by measuring the increase of its electrical resistance due to the heating current. It is denoted by $\Delta T_{s,max}$, since the maximum temperature increase is expected at the Joule heated central electrode (see Figure 3.5b). $\Delta T_{s,max}$ can be inferred from the measured temperature increase averaged over the suspended segments of the sample, $\overline{\Delta T_s}$, by assuming a linear temperature profile in absence of self heating and modes of heat transfer other than conduction: $\Delta T_{s,max} = 2\overline{\Delta T_s}$. Any measurable deviation from a linear profile can be avoided by applying small enough currents through the sample during the resistance measurement.

Clearly a prerequisite to the accuracy of this approach is that the sample resistance can be accurately measured, while a heating current is applied simultaneously. The feasibility is not obvious, since sample and electrode are electrically connected, which means they could interfere. Based on Kirchhoff's current law which is valid in this case of low frequency currents, interferences can be avoided if at least one of the sources has a floating ground, or in other words is isolated from ground. The case of a floating heating current source is depicted in the equivalent circuit of the device, Figure 5.12b. Since charge accumulation can not occur in steady state, the currents flowing out of and into the source V_h must be equal. As no current can be drawn from or flow to ground this implies that $I_{h,1} = I_{h,2}$.

Moreover applying Kirchhoff's current law to the node formed by the junction of all four resistors yields $I_{h,1} - I_{h,2} + I_{s,1} - I_{s,2} = I_{s,1} - I_{s,2} = 0$. Therefore in case of a floating ground the currents do not interfere and the resistance of the sample $R_{s,1} + R_{s,2}$ can be determined irrespective of the heating current. This observation holds true for arbitrary values of the four resistances. In general the voltage read by the meter depicted in Figure 5.12b is

$$V = R_{s,2} I_s + R_{h,1} I_h - S\Delta T_{s,max}. \tag{8}$$

Here it is assumed that the Seebeck coefficient of the supported central electrode is negligible. It should be noted that generally the contribution due to the Seebeck effect is $(S_{\mathrm{el}} - S)\Delta T_{s,max}$, where S_{el} is the Seebeck coefficient of the electrode. S_{el} in turn can be approximated to $S_{\mathrm{el}} \approx S_{\mathrm{Au}} + (S - S_{\mathrm{Au}})\frac{G}{G_{\mathrm{Au}}}$ for small G/G_{Au}, where G is the electrical conductance of the electrodeposited part of the electrode and G_{Au} that of the underlying gold. This takes account of the electrode being a composite of gold and the deposited material. As the Seebeck coefficient of gold is below 2.2 µV/K in the studied range of temperatures [72, 73], S_{el} can be ignored if the conductance of the deposited material is much smaller than the gold's. Particularly when n-type materials are studied, as in the present case, the Seebeck coefficient of the electrode can be close to 0 as the thermopowers of the composites cancel, however the relative nature of the measurement has to be considered especially when materials of low thermopower are studied. There are several ways of extracting from the measured voltage the desired thermovoltage $-S\Delta T_{s,max}$. In the present case the most advantageous is to apply AC heating currents. Since the other voltages are applied and measured by National Instruments data acquisition modules at a sampling rate about 2 Hz, voltages due to the AC heating current are averaged out when the frequency of the heating source is sufficiently high.

Isolation from ground of the AC source is ensured by using the secondary current of a transformer powered in our case by a function generator. This has the additional advantages that constant voltage offsets of the source are eliminated and impedance matching allows achieving increased heating currents.

In practice the Seebeck coefficient is measured by performing linear sample current sweeps of small amplitude while simultaneously increasing the alternating heating current amplitude (see Sec. 5.3.2). The slope of the V-I curves again indicates the sample resistance, since the

last two terms in Equation 8, $R_{h,1}I_h - S\Delta T_{s,max}$, are independent of the sample current I_s. The offset of the curves is the thermovoltage (the second term in Equation 8, $R_{h,1}I_h$, is averaged out).

5.3.1 Finite element modeling

Figure 5.13a is an example of a linear regression of the measured resistance and power. Figure 5.13b displays the deviation of the measured from the set thermal conductivity ($2\,\mathrm{Wm^{-1}K^{-1}}$) as a function of metal and oxide film thickness and Figure 5.13c shows the deviation of the measured from the set electrical conductivity (150 kS/m). Generally the thickness was set to 2 µm, the thermopower to $80\,\mathrm{\mu VK^{-1}}$ and a temperature coefficient of $0.001\,\mathrm{K^{-1}}$. The influence of the relevant parameters on the systematic measurement error is discussed later.

As expected the error in the electrical conductivity measurement does not significantly depend on the thickness of the metal or oxide film.

The error in the thermal conductivity measurement has a clear increasing trend with increasing oxide thickness and decreasing metal film thickness. Increasing the oxide thickness causes the thermal resistance between the sample and the surrounding substrate to increase and for equal power dissipation this causes the temperature difference between the supported segments of the sample and the substrate to increase, which is assumed to be negligible. Thinning the metal film decreases its efficiency of conducting heat and and therefore this also increases the error. Figure 5.14b shows the error in the estimation of ΔT again as a function of metal and oxide film thickness. Here the temperature difference, computed from the resistance increase, was compared with the actual difference of the sample temperature close to the edge of the central electrode and the sample temperature at the edge of the pit. These temperatures were chosen in recognition that temperature excursions within supported segments of the sample do not matter, as arising potential differences are eliminated by the supporting metal film. It can be observed that the error in the temperature measurements accounts to a large degree for the error of the thermopower measurement (see Figure 5.14a). This is even more obvious when variations in the width of the central electrode caused by underetching are ignored, which were accounted for in the presented case. Clearly the error of the temperature decreases with the oxide thickness. The main reason for this is that the heating power has to be increased to maintain the temperature excursion as the oxide film

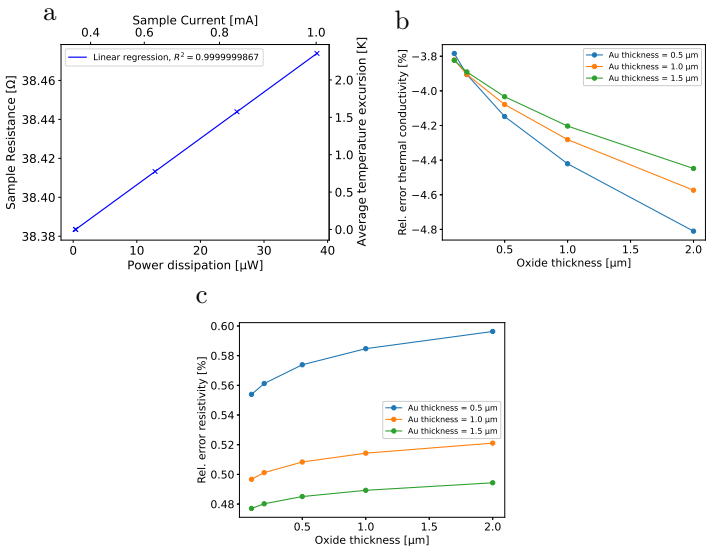

Figure 5.13: The computed sample resistance as a function of the applied power including the line of best fit (a). From the slope and sample dimensions the thermal conductivity can be obtained, the relative error is plotted as a function of oxide and metal film thickness (b). The relative error of the measured resistivity is displayed again as a function of oxide and metal film thickness (c).

thickness decreases. The increased heat flux into the substrate causes the temperature of the substrate around the sample to increase. For the same reason the error increases with the width of the central bridge. The lower heat flux in case of a narrower bridge leads to a more accurate temperature difference measurement, since the accuracy of this measurement rests on the assumption that the temperature at the ends of the sample does not deviate from that of the heat sink.

It should also be noted that significantly improved accuracy can be achieved by suspending samples over through-holes etched into the Si-chips from the back side, but applying the same measurement method, as will be discussed in Section 5.4. The reason is that improved thermal isolation between the ends of the sample can be achieved, as through-holes of arbitrary dimension are feasible. Moreover this limits the exposure of the sample to the wet etchants, as the etching processes can be mostly carried out from the back side and also offers direct observation of the sample's underside to detect residual metal.

Apart from studying the influence of design parameters the range of applicability was also investigated by determining measurement errors as a function of the sample properties. The relative errors were studied for a set of thermal and electrical conductivities, see Figure 5.15 (the measurement errors were found to have a negligible dependence on the thermopower in

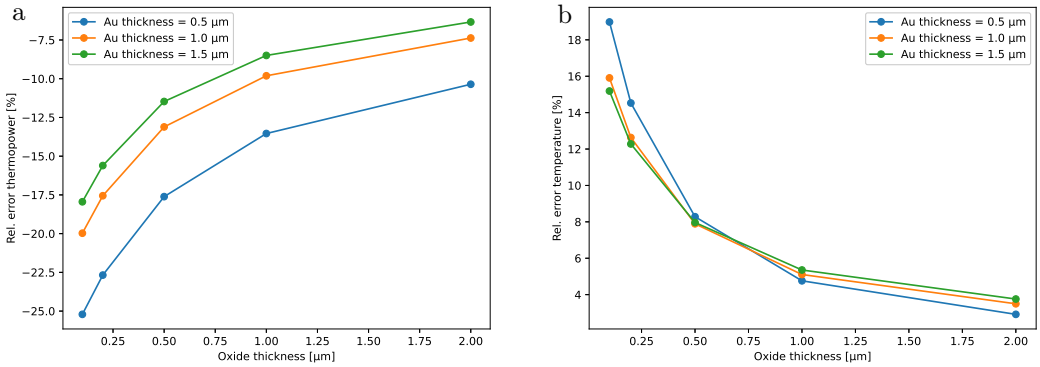

Figure 5.14: Relative error of the thermopower as a function of metal and oxide film thickness (a). Relative deviation of the determined temperature excursion from the average temperature excursion of the supported segment (b).

the range of 10 to 210 μVK^{-1}). All other properties were maintained constant. The thermal conductivity error clearly increases with the sample's thermal conductance. More significant is the dependence of the thermopower measurements on the electrical conductance. A main contribution to this is that the thermoelectric properties of supported areas become more heavily weighted by the deposited material instead of the underlying metal. More thermally and electrically conductive samples have to be compensated for by decreasing the film thickness: To maintain the systematic thermopower error below 10 % the electrical sample conductance should not exceed 0.1 S, which corresponds to a sheet resistance of 1.4 Ω.

To assess their impact on the results, thermal and electrical contact resistances were included. For the thermal interface resistance between the thermoelectric and gold $2 \times 10^{-6}\,m^2KW^{-1}$ were chosen based on the measurement by the photoacoustic method [74] on an interface obtained by electroplating bismuth telluride on nickel. The contact resistance between gold and silicon oxide was determined by oxide layer thickness dependent measurements to be less than $10^{-8}\,m^2KW^{-1}$[75]. The thermal interface resistance between oxide and underlying silicon was ignored as a value less than $10^{-9}\,m^2KW^{-1}$ is expected [76]. Finally based on [77] 5 $\mu\Omega cm^2$ can be considered an upper bound for the electrical contact resistance. With these values the error of the thermal conductivity measurement increases to 5 %, while the thermopower error decreases. These results indicates that contact resistances should be taken into account, for instance by performing sample length dependent measurements, but are expected to have limited impact.

In conclusion of the numerical studies one can observe that the thickness of the metal

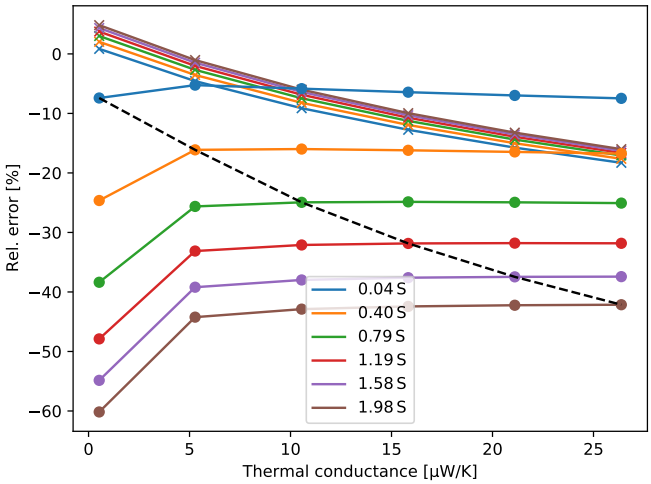

Figure 5.15: Relative error of the thermal conductivity measurement (crosses) and the thermopower measurement (circles) as a function of the sample's thermal and electrical conductance. The dashed black curve connects points for which thermal and electrical conductance are coupled and thus provides an estimate of the film thickness dependence of the error.

film should be maximized since it decreases the systematic error in the measurement of all thermoelectric properties. The thickness of the oxide layer correlates with an increase of the thermal conductivity measurement error, however also with a decrease of the thermopower measurement error. The latter dependence is more significant. Also the error on the thermopower contributes twice as much to the overall error on the figure of merit, since it depends on the square of the thermopower. Therefore a thermal oxide and gold film thickness of 1 µm was chosen as a trade-off.

5.3.2 Device validation by measurements

As mentioned, the electrical sample resistance is determined from sample current sweeps of peak values below 100 µA resulting (for typical sample resistances) in heating power less than 1 µW and therefore temperature excursions on the order of only 1 mK, which is negligible. The thermal conductance is obtained from the static resistance as a function of power. The sample dimensions are obtained from SEM micrographs and based on these thermal and electrical conductivity can be derived, as displayed in Figure 5.16a and b. The uncertainty in the sample dimensions is the main contribution to the error bars. The Seebeck coefficient is determined by measuring the sample resistance while applying alternating heating currents

of increasing amplitude. The slope and offset of the obtained V-I curves indeed increase with the heating current, as illustrated by Figure 5.16c, indicating the increasing resistance / temperature and the thermovoltage respectively. Since the thermovoltage measurements are most prone to systematic errors based on the numerical modeling, they are compared to measurements on reference samples (Figure 5.16d) that were in each case deposited together with the microdevices and released from the conducting substrate by a lift-off process and etching. In accordance with the numerical modeling the thermopower is always underestimated, however consistently by about 20 %, which is much greater than the expected deviation. Some contributing factors can be identified. Firstly, it was determined by 4 point probe measurements that the resistivity of the underlying gold film is 32 % greater than assumed in the finite element model, and it was demonstrated that increased errors can be expected in this case (cf. Figure 5.14a). Secondly as mentioned above abnormal undercutting occurs, likely due to galvanic coupling between gold and chromium [80], which intensifies the width variation along the central electrode. This can lead to temperature gradients close to the junction and therefore an overestimation of the temperature difference. As mentioned above, based on numerical studies and also preliminary experimental results significant improvements can be expected by fabricating devices over through-holes in the substrate, but employing the same measurement method.

The reference measurement on Bi_2Te_3 was carried out by a Linseis LSR-3, the others were performed on a setup described above. The results of electrical and thermal conductivity measurements are compared to values from literature, at least in case of the pure metal samples. The significantly greater uncertainty in case of the Ni and Bi samples is caused by the uncertainty in the sample dimensions: the bismuth sample has greater relative roughness and this is also true for the nickel sample because less than 100 nm of nickel were deposited. The reason for this choice is that nickel has a significantly greater electrical conductivity and therefore would have an accordingly greater impact on the Seebeck coefficient measurement. Additionally the higher conductivity implies that the sample current would need to be increased beyond hardware imposed limits to achieve sufficient temperature excursions, if the thickness is not reduced. Nonetheless the electrical and thermal conductivities are in good agreement to values from literature. Generally also measurements on both branches are in good agreement. The exception is the nickel sample caused by a tear in the left sample and residual material on the right branch.

The results on bismuth telluride were further analyzed. These samples (reference samples and microdevices) were annealed prior to the thermoelectric characterization, as in case of Bi_2Te_3 electrical resistance drift was observed, particularly at higher temperatures. The drift at constant temperature occurs at a usually increasing rate of about 0.2 Ω/h or 3.5 ‰/h. Further investigation is required, but stabilization could be achieved by annealing at 215 °C for 2 h in air. It is noteworthy that after improving the design (see Section 5.4) drift was more rarely observed and less pronounced in general. This could indicate that the drift is caused in part by defects induced by exposure to the oxide etchant which visibly increases surface roughness. After employing the through-hole devices, exposure to the oxide etchant could be avoided.

Higher temperatures were avoided to prevent significant diffusion of gold into the sample [81]. This had no measurable effect on the composition, determined by energy dispersive X-ray spectroscopy to be 41 at. % bismuth, but induced grain growth (see 4.2).

Using the expressions for the electronic properties described in Section 2.1 based on the Fermi-Dirac integral, their dependence on the Fermi level can be modeled. For the hole-electron mass ratio 1.4 was assumed based on [82] and for the mobility ratio 2/3 [83]. For the conductivity absolute values are required, for electrons a mobility of 150 $\frac{\mathrm{cm}^2}{\mathrm{Vs}}$ [84] and an effective mass of $0.58\,m_0$ is assumed, where m_0 denotes the free electron mass. With these assumptions the results displayed in Figure 5.17 are obtained. The measured Seebeck coefficients between -80 and -100 µV/K would be consistent with intrinsic and strongly n-doped conduction, however the measured electrical resistivity is only consistent with the degenerate case and thus the measured Seebeck coefficient indicates a Fermi level about 70 meV. The electrical resistivity at this value, 9.5 µΩm, is in good agreement with the measured 9.0 µΩm. An other observation in support of this conclusion is the increase of the absolute value of the Seebeck coefficient as the temperature is increased. Typically the Fermi level approaches the center of the band gap as the temperature is increased, as eventually intrinsic conduction dominates. If the Fermi level already lay within the band gap at room temperature, one would expect the thermopower to decrease. Since the opposite is observed, the Fermi level is likely within the conduction band at room temperature.

The lattice contribution of the thermal conductivity κ_l is isolated by subtracting the charge carrier contribution, which is derived from the Wiedemann-Franz law, i.e. $\kappa_l = \kappa_{tot} - L\sigma T$. The Sommerfeld value for degenerate conductors is used as the Lorenz number,

i.e. $2.44 \times 10^{-8}\,\mathrm{W\Omega K^{-2}}$. It is well known that narrow-band gap semiconductors such as Bi_2Te_3 can exhibit bipolar conduction [5, 85] and therefore significantly enhanced Lorenz numbers in the transition region, cf. Figure 5.17, but this can be excluded, as explained above.

At room temperature the value obtained for the lattice thermal conductivity is $0.5\,\mathrm{Wm^{-1}K^{-1}}$, which falls short of the values of 1.5 and $0.7\,\mathrm{Wm^{-1}K^{-1}}$ reported for transport along and across the cleavage planes of single crystals respectively [86, 87, 88, 68]. To a large degree this can be attributed to scattering at grain boundaries. It was determined by X-ray diffraction (XRD) that the grain size is on the order of 100 nm and, although it exceeds the phonon mean free path by orders of magnitude, one can expect a decrease of the lattice thermal conductivity by nearly 50 % at least along the trigonal direction [68, 89], based on modeling for this case. The experimental results are in good agreement with those of Takashiri et al. who studied the lattice thermal conductivity of flash evaporated nanocrystalline Bi_2Te_3 as a function of grain size. The thermal conductivity was measured using a differential 3ω method in this study and various grain sizes were obtained by annealing at 150 and 250 °C. After annealing at 250 °C at a grain size of 60 nm the authors find a lattice thermal conductivity of $0.4\,\mathrm{Wm^{-1}K^{-1}}$. A value of $0.5\,\mathrm{Wm^{-1}K^{-1}}$ at grain sizes between 100 and 300 nm follows well the trend observed by the authors.

The observed significant deviation from measurements on bulk samples in case of Bi_2Te_3 raises the question why similar deviations were not observed in case of the studied Ni and Bi samples. Different reasons apply. In case of nickel the lattice contribution comprises only a few percent of the total thermal conductivity, particularly around room temperature [79]. Changes in the lattice contribution are therefore difficult to observe and boundary scattering typically affects phonons before charge carriers as the length scale is decreased. In case of the bismuth sample the situation is different, charge carriers and phonons contribute approximately equally to the thermal conductance at room temperature. However the grain sizes in this sample are at least one order of magnitude greater compared to the other studied samples, i.e. greater than 1 µm. This was not determined by XRD, but the plating conditions are the same as in Sandnes et al. [63], who report grains of this size, and this is also consistent with the coarse grained appearance of this sample under scanning electron microscopy (SEM) compared to the others. In general the samples appear to be compact and uniform, which is consistent with the typically good agreement between measurements

on either branches.

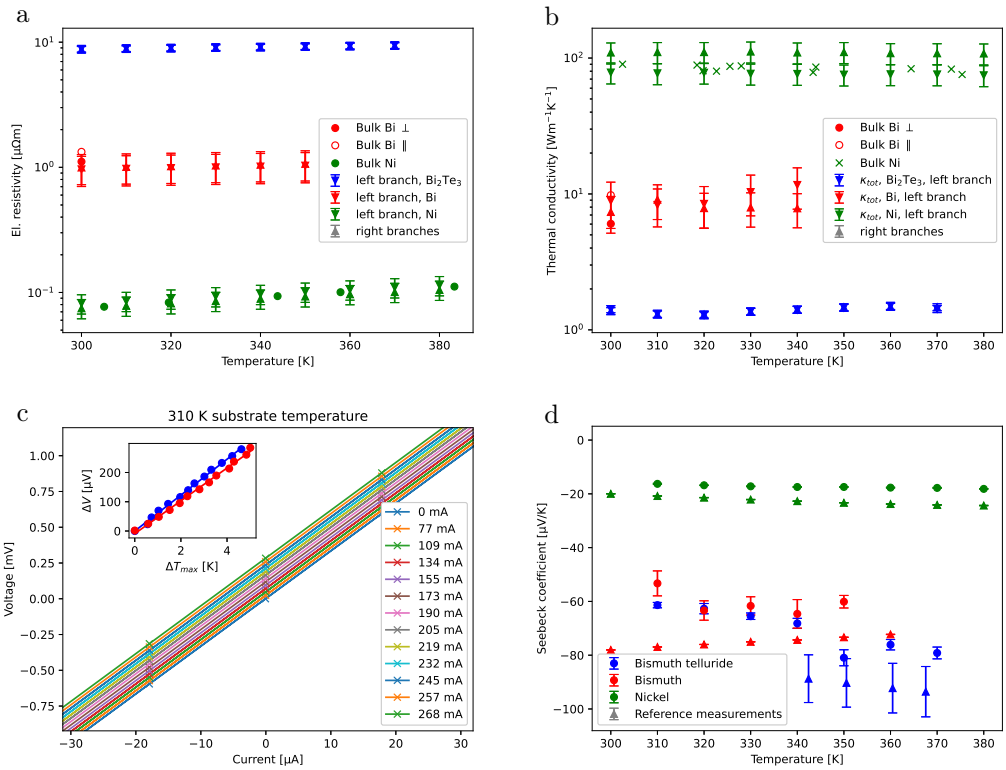

Figure 5.16: (a) Resistivity of the two branches of the Bi, Ni and Bi_2Te_3 samples, measured by the pseudo-4-probe method. Bulk measurements are taken from [78] in case of Bi and [79] in case of Ni. (b) The thermal conductivity is displayed for both branches and all three samples. Reference values are from the same sources as for (a). (c) The voltage drop along the right sample branch is plotted against the current through the sample for increasing AC heating currents (approximate peak values). The increasing offset is equal to the thermovoltage, while the resistance is derived from the slope (the increase of the slope is too small to be noticed by bare eye). The inset is a representative example of a thermovoltage-temperature curve for both branches of the sample, which is the result of analyzing the family of curves. (d) Comparison of the measured thermopower with reference measurements on the Bi, Ni and Bi_2Te_3 samples. For the sake of clarity the thermopower is in each case displayed for one of the two suspended branches only. The reference measurements were obtained with a Linseis LSR-3 device in case of bismuth telluride and a self-built setup for the other samples.

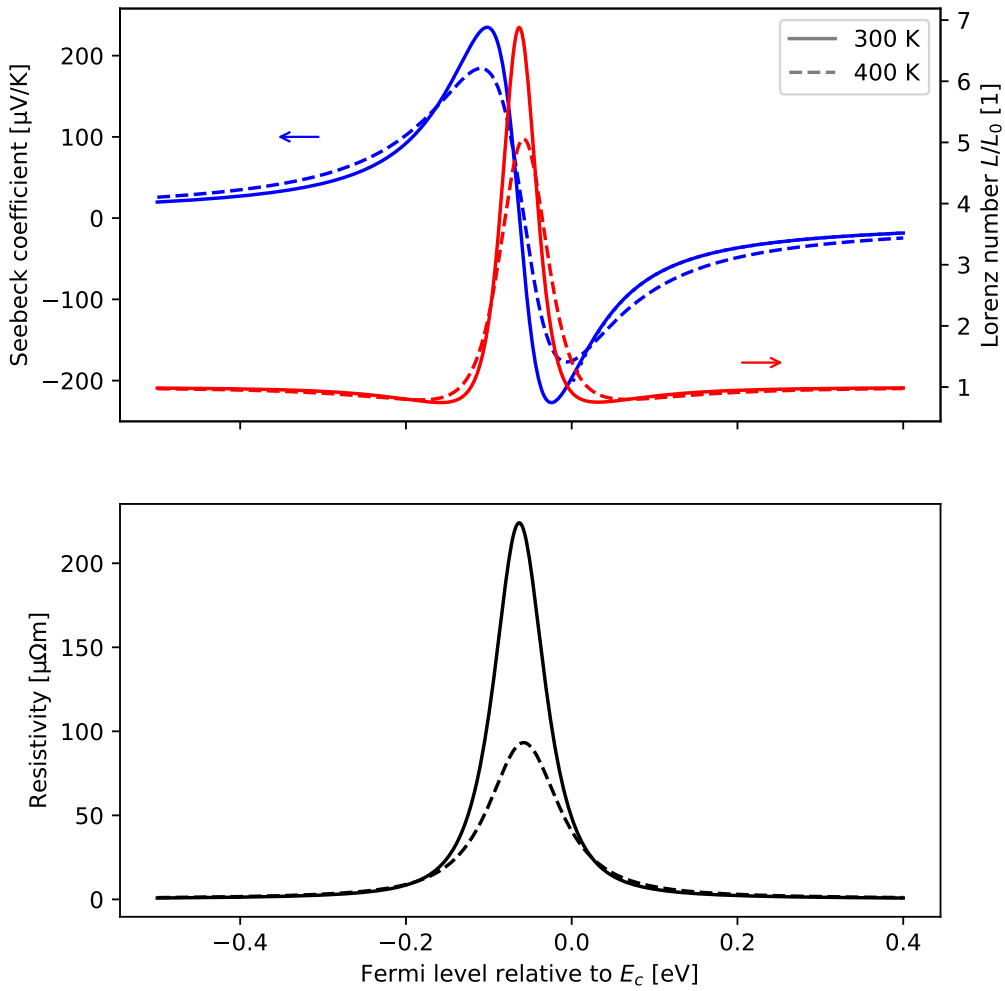

Figure 5.17: The Seebeck coefficient, Lorenz number and electrical resistivity are computed for bismuth telluride as a function of the Fermi level based on a two-band effective mass model, as described in Section 2.1.

5.4 Improvement of measurement devices for thermoelectric characterization

The main reasoning behind the design of the previously described devices was to achieve a relatively thermally isolated heating electrode, to allow for local heating of the heated electrode, required for thermopower measurement. As noted with regard to the previous devices, the measurement mainly affected by systematic error is the Seebeck coefficient. As was previously discussed, some heat conduction to the other ends of the samples can not be prevented, causing the major contribution to the systematic error of the thermopower measurement. It stands to reason that the thermal isolation could be increased and thus the systematic error decreased, if the length of the trenches over which the samples are suspended could be increased. However this would be necessarily be accompanied by an elongation of the heated electrode and a corresponding increase of Joule heating. Thus moving from square shaped designs to ones of greater aspect ratio would not be beneficial.

The substrate below the heated electrode gradually narrows towards the electrode, the full taper angle is approximately $180° - 2 \times 54.74° = 70.52°$. The edges of through-holes etched through the wafer from the back side have a smaller taper of 54.74°. So it should be possible to use heating electrodes placed at the edges of through-holes even more effectively to achieve local heating. The great advantage in this case is moreover that the length of the hole and the heated electrode do not need to be identical. Exploiting this additional degree of freedom, i.e. utilizing through-holes of high aspect ratio, should allow decreasing the systematic error. Indeed, the through-holes were designed to be much longer than the electrodes (700 µm compared to 150 µm, see Figure 5.18e). This design ensures that the temperature of the unheated electrode remains the same even when a heating current is applied to the other.

An other important advantage is that plating onto the heating electrode during sample deposition can be avoided. Thus the Seebeck coefficient is measured relative to gold and not a composite of gold and the sample material, which is particularly important in case films of low sheet resistance compared to gold are deposited. This can also be achieved in case of the earlier design, but would require an additional potentially damaging lithography step onto suspended structures. A further advantage is that the release of the samples which completes the fabrication can be carried out from the back side. This means that

the sample's chemical exposure is limited to the gold etchant (potassium iodide / iodine solution) and the solution for stripping the photoresist. Exposure to the etchants for the other underlying layers, i.e. Cr and silicon dioxide, can be avoided completely. Finally the back sides of the samples can be inspected under a under a microscope. Care was taken to place the die up side down on spacers to prevent damage to the sample. Inspection of the back side is useful for detecting residual gold for instance.

The approach of determining the three thermoelectric properties and thereby the figure of merit is again measuring the sample resistance by the common pseudo 4-probe method, the thermal resistance by measuring the temperature increase in the sample induced by Joule heating, using the sample itself as a resistance thermometer and the thermopower by applying AC heating currents through the electrodes supporting the sample at either end, while simultaneously measuring the induced Seebeck voltage.

The disadvantages are the addition of one photolithography step (three on the whole) to the process flow. Also the sample can be contaminated from the back side, specifically thermal grease, previously used to establish thermal contact to the substrate, can be pressed through the hole and contact the sample.

5.4.1 FEM modeling of the improved design

As in case of the previous design, the performance of the devices was investigated numerically, prior to fabrication. The new design offers more adjustable parameters than the previous one, as was discussed above. Since some dependencies are similar, the discussion is limited to the most relevant parameters. First it can be demonstrated that the accuracy of the Seebeck coefficient measurement increases with the aspect ratio of the through holes, but saturates eventually, thus the length of the holds was set to 700 µm. The dependence on the thickness of the gold film is similar to the one observed in case of the original designs, i.e. the accuracy of all measurands increases with the thickness of gold. Thus instead of the Au layer thickness, the influence of the widths of the two electrodes supporting the sample are presented in Figure 5.18. The resistivity unsurprisingly is again least affected by systematic errors. Also the oxide thickness has negligible influence, as Joule heating at currents no greater than 50 µA is insignificant in this case. The error is greater than for the previous design, mainly because 2.5 times shorter samples were considered (150 µm and 60 µm). The error increases with the electrode width, as the measured voltage is

derived from an average over the electrode width, which slightly, and increasingly with the width, deviates from the potential at the electrode edge. In case of the thermal conductivity the opposite trend is observed. This can be explained by the improved thermal anchoring to the substrate. The Seebeck coefficient displays the most pronounced dependence on the electrode width. Again the error decreases with increasing width. In this case however heating of the substrate is not the cause. In fact the heating power required to maintain a constant temperature excursion is more than proportional to the electrode width, as the simulation results reveal. Thus less power is dissipated into the substrate for the thinner electrodes. The reason is rather the reduced thermal conductance from the electrode to the substrate. Due to this the heat conducted through the sample from the heated side causes a small temperature rise at the other side, violating the assumption that the temperature of the unheated side remains unchanged. Comparing the actual sample boundary temperature difference to the value derived from the average temperature increase (cf. Figure 5.18d) reveals that nearly the entire thermopower measurement error stems from overestimating the temperature difference, not inaccuracy of the voltage measurement.

The numerical results reveal firstly that a significantly improved measurement accuracy can be expected, particularly of the Seebeck coefficient, but also the thermal conductivity. Moreover an increased electrode width is on the whole to be considered desirable. As a trade-off a width of 30 µm was chosen, which can turn out slightly lower in practice due to undercut during the etching processes, as was discussed above. Wider electrodes would be problematic, as the heating current that can be supplied by the function generator is limited, and assuming a constant current amplitude, the power is antiproportional to the electrode width.

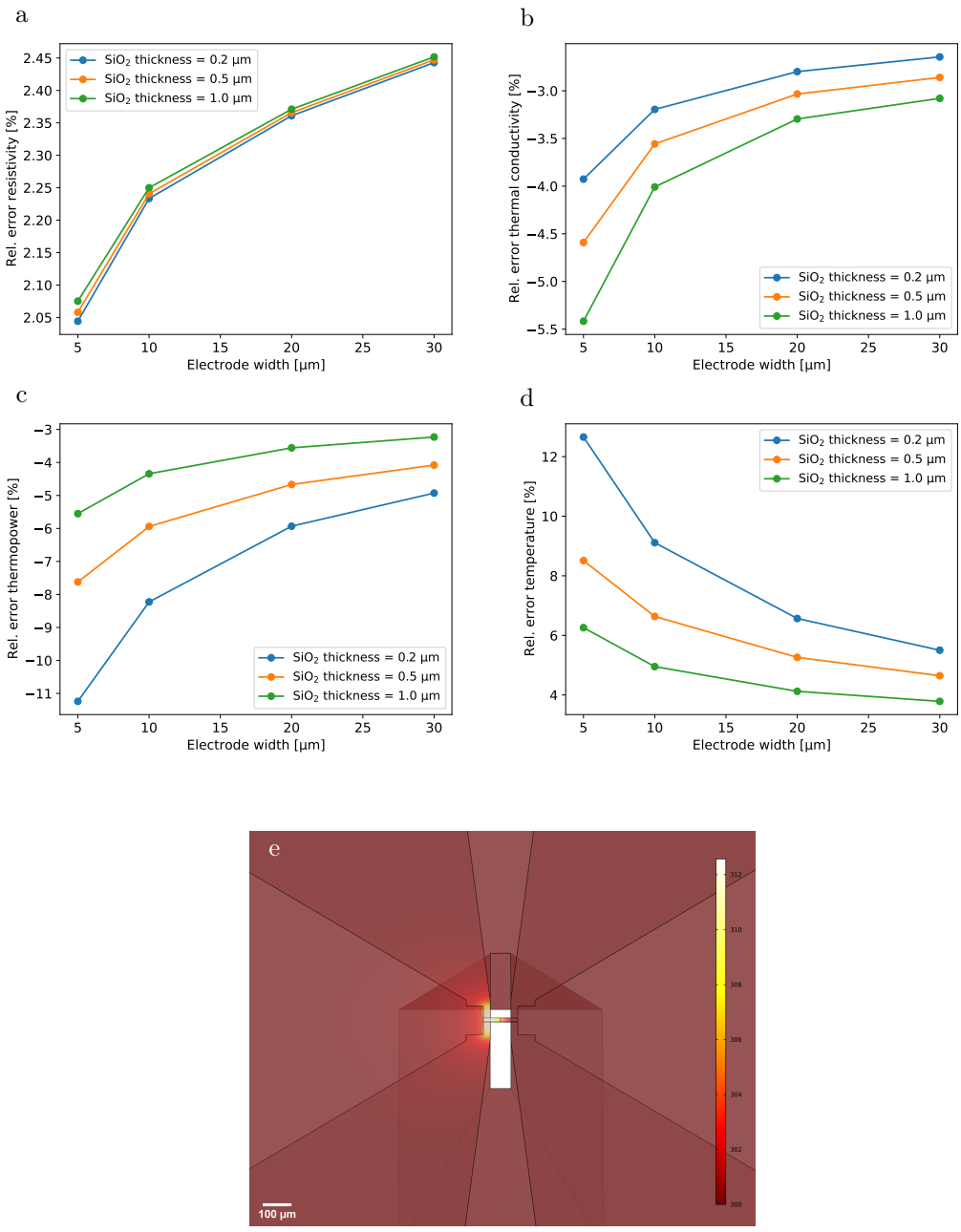

Figure 5.18: As in case of the original design the relative errors of the thermoelectric properties and the temperature difference, (a) to (d), are determined as a function of certain design parameters, namely the width of the electrodes and the thickness of the underlying oxide, by FEM. A graphical representation of one solution indicating temperature by a color map is also shown (e).

5.5 Measurement setup

Figure 5.19 is a schematic illustrating the part of the setup used to perform the electrical measurements. The measurement of the sample resistance is again performed by the pseudo 4-probe method. The DC sample current is applied through the top two electrodes, while the voltage across the sample is measured by the bottom two. Using the bottom two contacts to determine the voltage ensures that Ohmic drop is minimized. The only significant other contribution to the sample voltage could stem from contact resistance. The AC heating current is supplied from a function generator, albeit through a transformer. This has a twofold purpose. First any DC offset to the AC voltage is eliminated by the transformer, as a DC component on the primary side would not induce a changing magnetic flux. Removing this contribution is vital, as one of the signals, the Seebeck voltage, is at most on the order of mV, thus even small offsets would cause significant measurement errors, which was indeed observed.

An electromechanical relay (double pole double throw type) is used to switch between heating the left and right electrode. This provides a cross-check of the measurement method, as the Seebeck coefficient should be inversion symmetric with regard to the temperature gradient, unless there are confounding effects, see for instance [90].

The second effect is impedance matching. The function generator's output has an inbuilt series resistance of 50 Ω and can output a 10 V peak voltage. This results in a peak current of about 200 mA when directly applied to the heating electrodes, which generally have a resistance less than 1 Ω and therefore a power of $RI^2/2 = 20\,\mathrm{mW}$. This limits the achievable temperature difference to about 2 K. Significantly more power could be supplied to a greater load, it can be shown that maximum power output of 250 mW is delivered to a load of 50 Ω. Greater power can still be supplied to a small resistance by using a transformer with a greater than 1 primary to secondary turn ratio. The load is greater by the square of the turn ratio and accordingly, since power is approximately conserved, so is the power supplied to the heating electrode. Indeed with the transformer temperatures in excess of 10 K can be achieved.

Accuracy of the method again requires isolation from ground of at least one of the sources. One concern in this regard is potential capacitive coupling to ground, which is relevant, as an AC source is used. It could cause formation of a ground loop. The impedance is

antiproportional to the frequency and the capacitance. It must greatly exceed the load for capacitive coupling to be negligible. Assuming even a capacitance on the order of one nF and the applied frequency of 131 kHz the impedance would be 300 Ω versus the heating electrode resistance less than 1 Ω. Indeed changes in the measured resistances between the states of a grounded and an isolated DC source were not observed.

5.6 Further modifications for measurement on highly resistive samples

Measurements on samples of low electrical conductivity posed an additional challenge, as usually electrical contact is established between the Au electrodes and the underlying silicon substrate due to the process flow, despite the 1 µm thick oxide film isolating them from each other (consider the equivalent circuit diagram, Figure 5.20a). While the connection to ground can be easily eliminated, the resistance parallel to R_s can not and poses a problem when studying samples of high resistance (on the order of 10 kΩ and above). The two possible reasons identified were the use of a diamond scribe to cleave the chips and the need to break gold bridges connecting the two electrodes after etching gold from the back side. This was caused by gold covering the entire through-holes. Both potential causes were eliminated by etching grooves into the wafer from the back side, which facilitates cleaving and renders the use of a diamond scribe unnecessary and extending the through-holes to ensure removal of all bridging gold by back side etching alone (compare 5.20b and c).

After these modifications indeed electrical isolation between the electrodes was observed after etching in absence of a sample.

In conclusion the goal of developing a method for the in-plane measurement of thermoelectric properties, in particular for deposited samples, can be considered achieved. The method was validated first numerically and also experimentally by measurement on various materials (Bi_2Te_3,bismuth and nickel). Deviations from bulk properties were only observed in case of bismuth telluride, which was attributed to enhanced grain boundary scattering of phonons, in agreement with previous results.

The initial design was significantly improved by employing through-holes but using the same method. The initially designed microdevices are only applicable to samples of limited electrical conductance, namely for sheet resistances greater than 1.4 Ω (see Section 5.3.1) and the thermopower is significantly underestimated in any case. Theses disadvantages are

eliminated by the improved design, which was verified by FEM and experimentally.

Additional improvements are the possibility to inspect both sides of the sample due to the through-holes and the limitation of exposure to etchants. Thus an accurate, comprehensive and transfer free method for measuring thermoelectric properties tailored to deposited samples has been developed. The method would also be applicable to other samples on the microscale, for instance nanowires.

In addition a self heating method for cross-plane characterization was developed, shown numerically to be accurate, based on eliminating the electrical spreading resistance by patterning the underlying metal film.

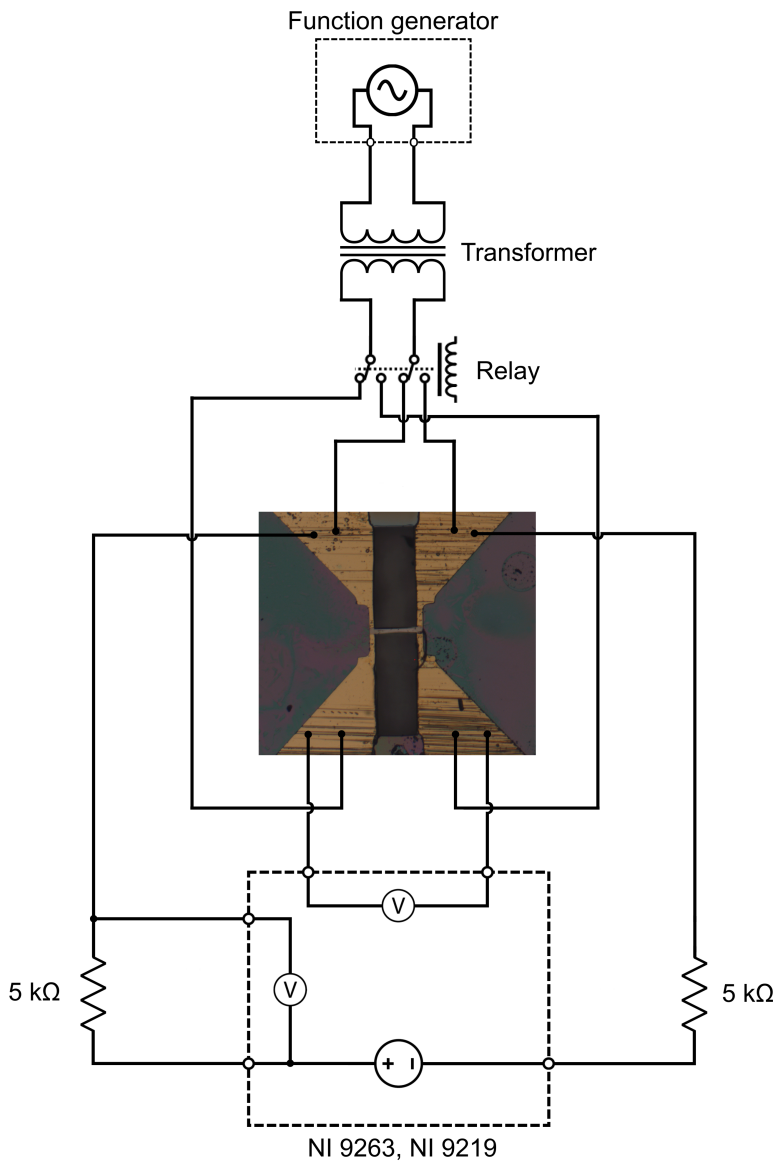

Figure 5.19: Schematic of the measurement setup, except for the temperature control system. The NI 9263 and NI 9219 out- and input modules are used to carry out pseudo-4-point measurements, while the function generator is used to apply heating current to the electrodes. The electromechanical relay allows selecting which electrode is heated.

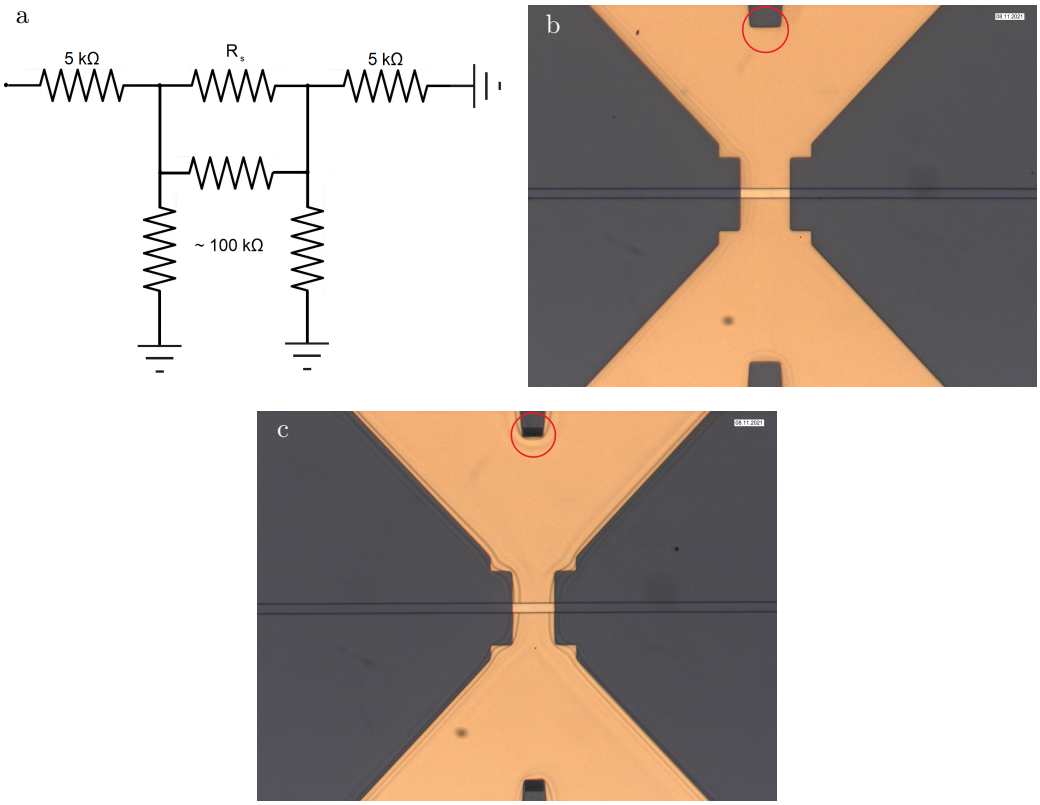

Figure 5.20: Equivalent circuit representing a part of the devices before contact to the substrate of the electrodes was eliminated (a). Resistor R_s represents the sample. (b) is a micrograph of the devices before the discussed design modification. The gold layer covers the entire through-holes. Figure (c) is a micrograph of the templates after the design was changed. After this change back side etching completely isolates the electrodes from each other. Earlier gold bridges remained at the edges of the through-holes that had to be broken manually.

6 Towards nanostructured materials

The measurement devices were again also verified by measurement on a sample of known properties. Nickel is frequently chosen as a reference material as it has been thoroughly characterized and as an elemental thermoelectric material cannot be affected by compositional changes. Moreover due to the small electron mean free path of less than 6 nm, size effects like grain boundary scattering are unlikely and it is also convenient for our application since samples of high purity can be easily electrodeposited. As can be observed in Figure 6.1b the measured Seebeck coefficient is in good agreement with literature results. Accidentally a thin film of just 20 nm thickness was deposited. Due to this and the roughness the thickness can not easily be determined, but the Seebeck coefficient is not directly geometry dependent. At the estimated thickness the resistivity at 300 K is 0.074 Ωm and a thermal conductivity of $96\,\mathrm{Wm^{-1}K^{-1}}$. The determined resistivity only slightly exceeds the literature value of 0.070 Ωm while the thermal conductivity exceeds the bulk value of $91\,\mathrm{Wm^{-1}K^{-1}}$. The determined Lorenz number, which again is geometry independent, in this case is $2.37 \times 10^{-8}\,\mathrm{V^2/K^2}$, which exceeds the literature value for nickel. One potential reason for the slight overestimation of the thermal conductivity, which these observations indicate, is again thermal radiation due to the relatively long and extremely thin sample. Typically later samples of less than half as long were considered.

The most obvious deviation from literature values lies in the temperature dependence of the thermal conductivity and the temperature coefficient of the electrical resistance. In the range between 300 and 370 K the latter lies below $3.2 \times 10^{-3}\,\mathrm{K^{-1}}$ while for pure nickel about $6 \times 10^{-3}\,\mathrm{K^{-1}}$ is expected. Changes to the measured thermal conductivity are barely noticeable while a decrease from 91 to $83\,\mathrm{Wm^{-1}K^{-1}}$ is expected. These observations are linked: The contribution to the thermal conductivity by lattice vibrations is negligible in case of nickel. Thus the derivative with respect to temperature of the thermal conductivity is $\frac{\mathrm{d}\kappa}{\mathrm{d}T} = L\sigma + LT\frac{\mathrm{d}\sigma}{\mathrm{d}T}$ and therefore $\kappa^{-1}\frac{\mathrm{d}\kappa}{\mathrm{d}T} = T^{-1} + \sigma^{-1}\frac{\mathrm{d}\sigma}{\mathrm{d}T} = T^{-1} - \alpha$, where α denotes the temperature coefficient of the electrical resistance. The lower temperature coefficient therefore accounts for the reduced temperature dependence of the thermal conductivity. The decrease of the temperature coefficient is expected in thin films, it can be derived from the Fuchs-Sondheimer function for the electrical conductivity of thin films. However at thicknesses of 3 to 4 electron mean free paths a decrease of the temperature coefficient by

about 10 % is expected, thus this is not the only reason. Indeed a reduced grain size also causes a decrease of the temperature coefficient and this is likely the main factor in case of the studied nanocrystalline sample.

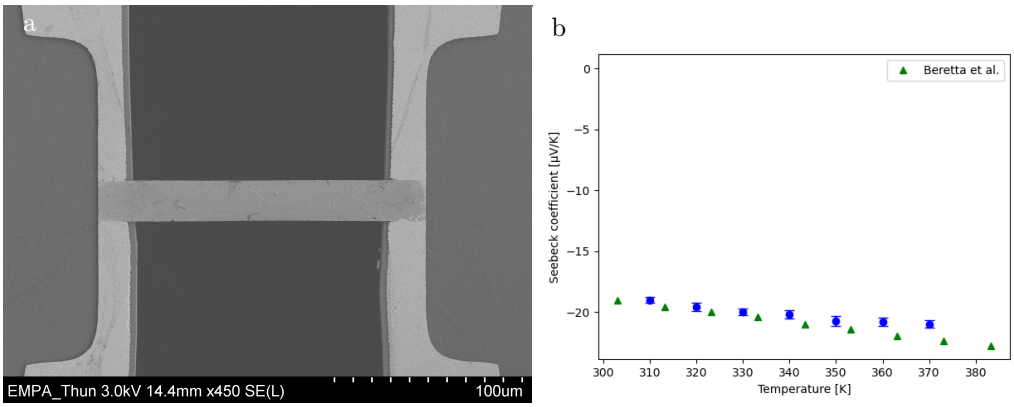

Figure 6.1: SEM image of the nickel sample used to verify the measurement method (a). The measurement results are compared to literature, taken from [2].

6.1 Thermopower of bismuth-rich bismuth telluride

Bismuth telluride is kown to transition from n- to p-type conduction as the bismuth content increases. Fleurial et al. [91] report the transition to occur at the stochiometric composition, i.e. 40 at. % bismuth while later studies observe the change to p-type conduction only at 57 at. % bismuth [65] (in both cases samples were obtained by solid state reaction). Whether this change is also observed in case of electroplated samples remains an open question. So far samples of bismuth content no greater than 50 at. % were found to remain n-type. The question has some relevance, since it can be desirable for the constituent materials in a multilayer to have the same type of conduction to avoid cancellation of the thermopower.

A sample deposited from an electrolyte with a greater molarity of Bi(III) than Te(IV) was characterized. Based on a XRF measurement the sample consisted of 80 at. % bismuth. The measured Seebeck coefficient is depicted in Figure 6.2. The origin of the significant dependence of the thermopower on the direction of the applied temperature gradient is unclear and was not usually observed in case of conductive samples. In any case the material is very likely p-type.

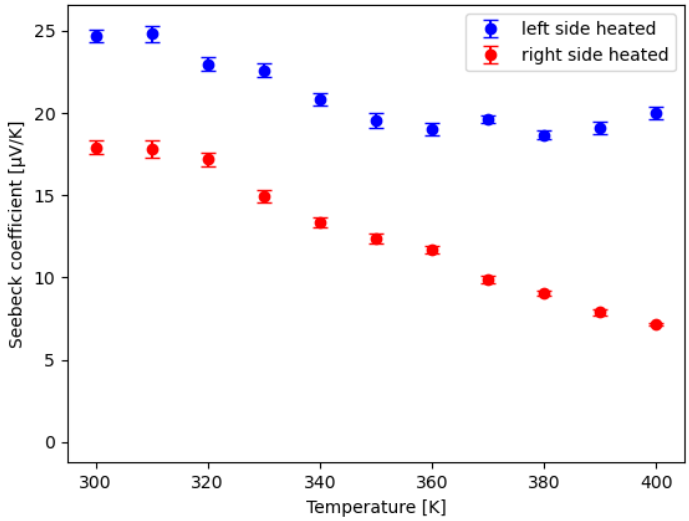

Figure 6.2: Measured Seebeck coefficient of the bismuth rich sample.

6.2 Composition modulated bismuth telluride multilayers

In accordance with the research plan deposition of multilayers, i.e. alternating layers of bismuth telluride with an excess of bismuth and tellurium was attempted by modulating the potential. The samples were deposited from the Bi(III), Te(IV) containing bath described above. In most cases reference samples were deposited together with the microdevices potentiostatically. The templates for the microdevices and the reference samples were short circuited in the process to ensure they are at the same potential. As was stated above nearly pure tellurium can be deposited from the bismuth containing bath by raising the potential to 115 mV vs Ag/AgCl. Bismuth could not be determined by XRF in such deposits. The bismuth telluride layer was deposited at no more than 20 mV vs Ag/AgCl which at least in steady state produces deposits with an excess of bismuth.

Based on the contrast in SEM images of a cross section of the reference sample (obtained by cleaving), see Figure 6.3, the composition indeed changes along the growth direction. Based on the SEM image the bismuth containing layer's thickness appears to exceed the other's. This is consistent with determination of the composition by EDX of the reference sample, which reveals a bismuth content about 27 at. %, which is close to the value expected when a 3:1 thickness ratio and a composition of 42 at. % for the bismuth containing layer is assumed, namely $0.75 \cdot 42\,\text{at.}\,\% = 31.5\,\text{at.}\,\%$. The microscale samples have an at least 5

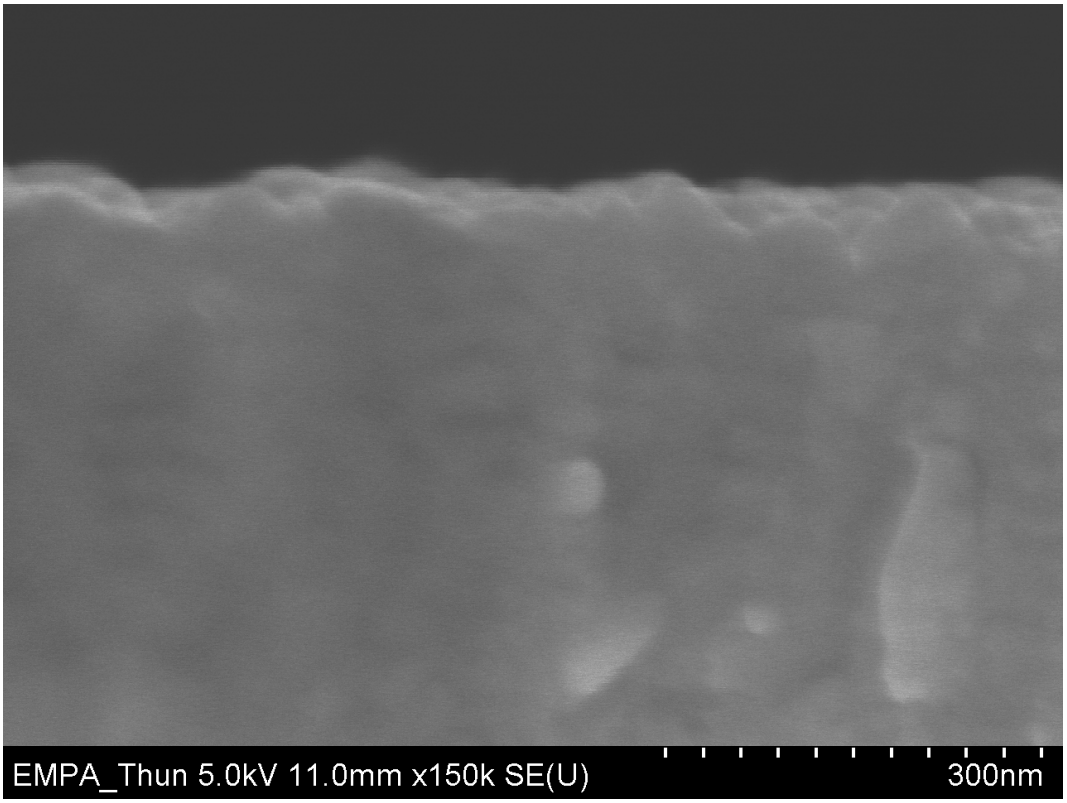

Figure 6.3: Example of an SEM cross section of an electrodeposited multilayered reference sample (a). The layered structure is revealed by a contrast in the secondary electron signal.

at. % higher bismuth content and are also significantly (up to 50%) thinner than reference samples. The higher bismuth content indicates that the deposition rate of tellurium is lower for the microdevices. Due to the low overpotential applied to deposit pure tellurium the deposition was indeed observed to be sensitive to the surface properties even for reference samples.

While certain samples had interesting properties, like a marked peak in the Seebeck coefficient as a function of temperature, these results are not discussed as the measurement could not be verified by applying bidirectional temperature gradients (they were carried out before introduction of bidirectional heating). Also clamping of the samples to the substrate was only introduced later. After these improvements the result could not be reproduced on other samples. Therefore results for a typical sample are presented below. First the resistivity of this sample is significantly greater than previously measured, even when when ignoring annealed samples. An other major difference is the temperature dependence of

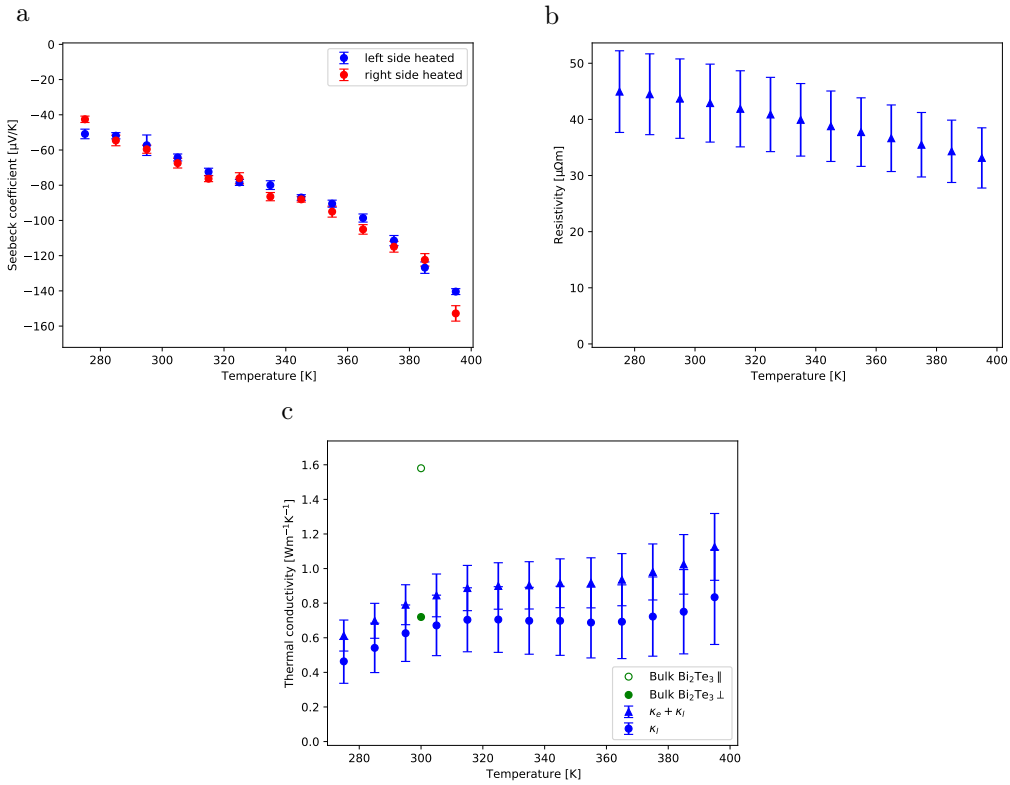

Figure 6.4: The Seebeck coefficient (a) resistivity (b) and thermal conductivity (c) of a multilayer.

the thermal conductivity. At room temperature this value slightly exceeds the previously measured. The main difference however is the significant increase as the sample is heated, the value at 400 K is nearly twice the value at 275 K. The evolution of the Seebeck coefficient also markedly deviates from previous observations. With -60 µV/K at room temperature, the value is significantly lower than the -80 µV/K previously observed. The value then increases until at 400 K with nearly -150 µV/K it markedly exceeds previous measurements limited to about -100 µV/K. The higher resistivity, it's negative temperature coefficient and the increasing thermal conductivity would be consistent with more intrinsic conduction. The low Seebeck coefficient at room temperature however, assuming the band structure of bismuth telluride, would be consistent with a nearly mid-gap Fermi level. This is however neither in keeping with the lower than expected resistivity under these conditions nor the strong increase of the Seebeck coefficient.

The observations indicate changes to the band structure, i.e. the sample likely can not be analyzed as a solid solution. Unusual properties can be expected due to the large difference of

the electron affinities of bismuth telluride and tellurium (4.5 eV and 1.97 eV respectively) and the according work function difference. This can cause type 3 or broken gap heterojunctions in which the band gaps of the materials do not overlap. Moreover the Fermi level difference will cause significant band bending. This alone can significantly alter the temperature dependence of the Seebeck coefficient [12].

At elevated temperatures the figure of merit of the multilayered sample significantly exceeds that of as-deposited samples: Based on the previous measurements on mm scale samples at 400 K a figure of merit about 0.08 was achieved (correcting for the overestimated thermal conductivity). In case of the multilayer the figure of merit is 0.23 at 400 K. This value still falls short of that obtained for annealed samples, i.e. approximately 0.3 at 400 K. It is likely that similar improvements can be achieved in bismuth rich bulk samples, since, as was stated above, the transition to p-type conduction tends to occur at increased bismuth concentrations in case of electrodeposited samples.

In general band bending caused by significant Fermi level offsets can be detrimental to the thermopower [12], thus multilayers composed of materials of a more similar work function are desirable. Thus in the following measures to obtain multilayers composed of bismuth telluride and polypyrrole are described.

6.3 Measurements on thin supported films

The modified devices can also be applied to the measurement of the thermoelectric properties of thin supported films. The electrical conductivity and Seebeck coefficient can be determined in spite of the support in the usual manner, the thermal conductivity can not. The design changes described above to avoid electrical contact of the electrodes to the substrate are essential to these measurements, as the thin films can have an electrical resistance on the order of 1 MΩ. Indeed before the changes discussed in section 5.6, similar resistances and Seebeck coefficients about $-1000\,\mu\mathrm{V/K}$ were measured, even after the sample was destroyed. These measurements were due to the substrate. After the design changes the resistance without a sample was too high to determine.

The sample of a thin film of Bi_2Te_3 (Figure 6.5a) characterized so far seems to have a higher Seebeck coefficient than the bulk samples whose absolute thermopower does not exceed $100\,\mu\mathrm{V/K}$.

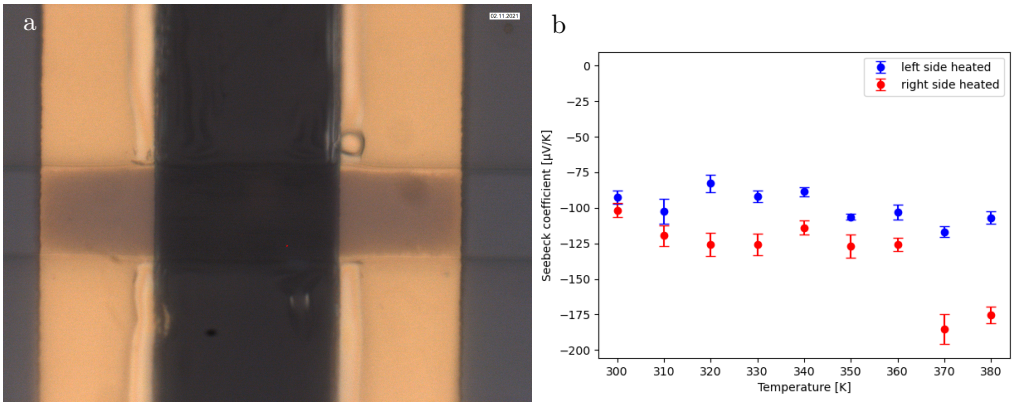

Figure 6.5: Micrograph of a supported Bi_2Te_3 thin film (a). The measured thermopower is displayed in (b).

6.4 Bismuth telluride / polypyrrole multilayers

The thermoelectric properties of layered structures in which one constituent is a polymer are promising. As was demonstrated in Subsection 2.2, firstly the in-plane thermopower can be enhanced, particularly in case of a significant band offset, which several conductive polymers can provide. Secondly polymers compared to inorganic semiconductors, which could also serve as the barrier material, typically have low thermal conductivity. Thirdly a significant acoustic mismatch, which is related to a group velocity mismatch, can be expected which can decrease in-plane thermal conductivity, even in the unlikely case of specular interfacial scattering.

Generally encasing Bi_2Te_3 nanostructures is apparently relevant to observing predicted enhancements, since measurements on suspended single-crystalline Bi_2Te_3 nanoplates point to significant n-type surface band bending in case of samples exposed to oxygen and nitrogen. By fitting to measurement results the degree of band bending was determined to exceed the band gap. This can suppress the Seebeck coefficient due to bipolar conduction. While the conduction band offsets in superlattices can be approximated by the difference of electron affinities according to Anderson's rule, band bending depends on the charge transfer between well and barrier materials. Thus finding a barrier material which matches the work function of the well material will help prevent band bending.

Polypyrrole was considered as an interesting barrier material for the following reasons: Firstly the large band gap (about 2 eV) [92] together with the large electron affinity difference between Bi_2Te_3 and polypyrrole (about 1.7 eV) [3] provides significant conductance and

valence band offsets. The approximate band structure expected at a bismuth telluride / polypyrrole heterojunction is depicted in Figure 6.6.

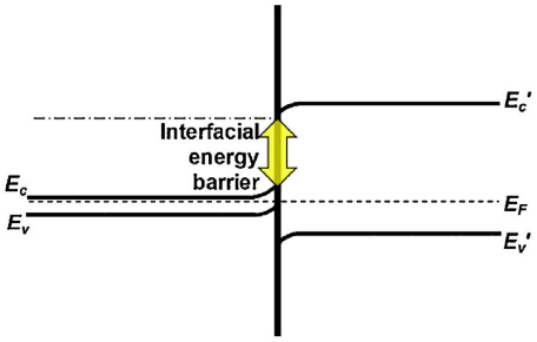

Figure 6.6: Band diagram around a bismuth telluride / polypyrrole heterojunction, taken from [3].

Secondly pyrrole is amenable to electrodeposition as it is soluble in water and electrodeposition from acidic baths has been demonstrated [93]. Moreover pyrrole has one of the lowest oxidation potentials among the electrically conducting polymers [94]. This gives rise to the possibility of depositing bismuth telluride and polypyrrole from the same bath. Coincidentally there has been interest in the thermoelectric properties of bismuth telluride / polypyrrole composits recently [3], in this case however the material was obtained by compaction and spark plasma sintering of polypyrrole / bismuth telluride powder. The crystallites are on the order of microns and amorphous polypyrrole aggregates between the grains. Therefore quantum confinement plays no role in the observed enhancement of thermoelectric properties, caused by a significant reduction of the thermal conductivity and enhancement of the Seebeck coefficient at the cost of an increase in resistivity. The decreased thermal conductivity is in part ascribed to enhanced scattering of phonons at grain boundaries, due to polypyrrole between grains and the enhanced Seebeck coefficient to a decrease of the charge carrier density, since polypyrrole is a p-type material.

One challenge with regard to electrodeposition from a single bath is the possibility of anodic dissolution of bismuth telluride while pyrrole is deposited. Several charge transfer mediators, among them the dihydroxybenzenes, have been investigated by Levine et al. [95]. The authors observed that hydroquinone, among several of the other compounds, significantly lowered the deposition potential on a platinum anode.

The effect of adding various amounts of hydroquinone to an electrolyte containing 50 mM of pyrrole and 0.3 M nitric acid on the deposition of pyrrole on a gold anode was studied by cyclic voltammetry, cf. Figure 6.7a. Apparently adding hydroquinone indeed lowers the deposition potential. It should be noted that hydroquinone is electrochemically active in the studied window and thus some of the current is due to the oxidation of hydroquinone, however deposition of polypyrrole at lower potentials was indeed observed. Also in aqueous solutions of hydroquinone only, the voltamograms are symmetric, see [96] for instance. The observed cathodic peaks at higher concentrations of hydroquinone could be mostly due to reduction of benzoquinone, the oxidation product of hydroquinone. It is smaller than the anodic peaks by an order of magnitude indicating that the anodic current is mostly due to pyrrole oxidation.

The effect of pyrrole and hydroquinone on the deposition of bismuth telluride was also examined, i.e. 50 mM of pyrrole and 100 mM hydroquinone was added to the bath containing 7.5 mM Bi(III) and 10 mM Te(IV) in about 0.3 M nitric acid and cyclic voltammetry carried out, cf. Figure 6.7b. For comparison a voltamogram without the added compounds is also displayed.

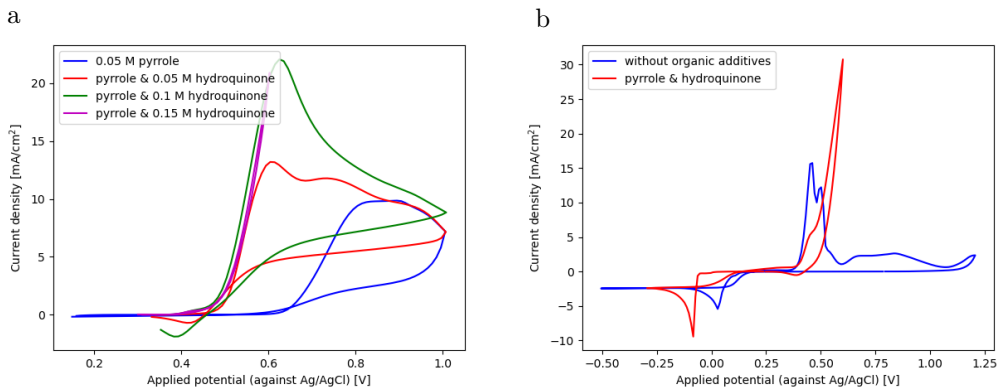

Figure 6.7: Cyclic voltamograms in aqueous solutions of pyrrole at varying concentration of hydroquinone (a). The voltamograms in the bismuth telluride bath and in an electrolyte with added pyrrole and hydroquinone.

Firstly a significant shift of the reduction potential by about 115 mV in the cathodic direction is observed. This is likely caused by deposition of polypyrrole on immersion of the electrode, possibly by chemisorption. A first oxidation wave occurs in both cases at about 450 mV against 3M Ag/AgCl. In case of the pyrrole containing electrolyte the oxidation wave's amplitude is however significantly smaller, likely because of the preceding deposition

of polypyrrole at less anodic potentials on the bismuth telluride, which is indicated by the greater anodic current compared to the pyrrole-free bath. The voltamograms indicate that the deposition of bismuth telluride and polypyrrole from the same bath is feasible.

The result of a first attempt at depositing a layered structure is displayed in Figure 6.8. Electroplating was carried out potentiostatically and each layer deposition was terminated by charge, cf. Figure 6.8b. Based on Equation 3 a thickness of 100 nm of the bismuth telluride film is expected in case of a current efficiency of 100 % (considering the cathode area is $0.25\,\mathrm{cm}^2$ in this case), which is close to the observed thickness. In case of polypyrrole, based on Equation (3), the expected thickness per charge density is $1.738\,\mu\mathrm{m\,cm^2C^{-1}}$, as its molar mass is 67.09 g/mol, 2.5 moles of electrons are released per mole of the product according to [93] and the density of polypyrrole is $1.6\,\mathrm{g\,cm^{-3}}$. Thus, given that 10 mC are deposited, a polypyrrole film of 70 nm is expected. However the measured value lies well below the expected one, indicating a significantly lower current efficiency. This is not unexpected, as one possible side reaction is the oxidation of hydroquinone. When bismuth telluride is deposited on polypyrrole the current remains near zero for several minutes before increasing rapidly, and only when this occurs deposition of bismuth telluride on polypyrrole is observed on the working electrode. In part this can be due to the necessity of charge transfer to first neutralize the polypyrrole film, which is likely oxidized [93]. According to Asavapiriyanont et al. [93] the excess charge constitutes one fifth of the charge required for deposition, which in the present case at most amounts to 2 mC. However due to the significantly lower current efficiency and thus lower than expected film thickness, this is likely not the only reason for the delayed deposition.

Based on Figure 6.8e the multilayer deposits are in some cases affected by protrusions exceeding several times the film thickness. Their origin is still uncertain. However after adding pyrrole to the Bi(III) and Te(IV) containing bath it gradually changes color and eventually turns black and opaque. Since tellurium is present in the precipitate based on XRF, possibly the cations serve as oxidizing agents for pyrrole.

The observed precipitation is not necessarily related to the protrusions since to a lesser degree they were also observed in polypyrrole deposits from hydroquinone containing electrolytes.

Finally electroplating alternating layers by alternating between two different electrolytes was also attempted resulting in smoother deposits, see Figure 6.9, but in this case for the

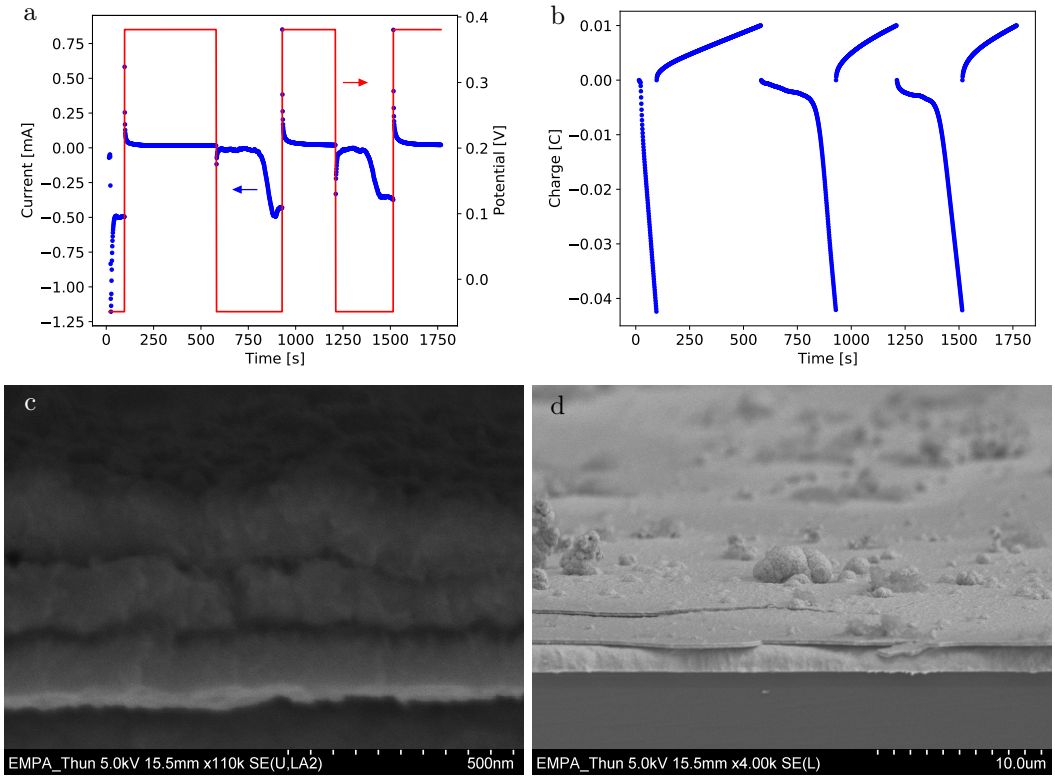

Figure 6.8: The deposition potential applied and the current during electroplating of bismuth telluride / polypyrrole multilayers (a). The deposition steps are charge controlled (b). (c) and (d) are SEM images of the obtained deposits.

applied potentials apparently full coverage during polypyrrole deposition was not achieved, resulting effectively in a porous but interconnected bismuth telluride deposits.

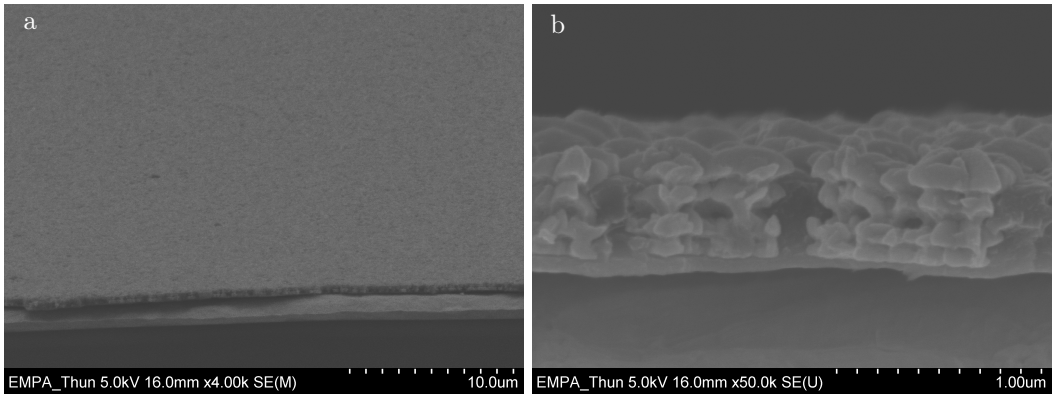

Figure 6.9: Wide shot SEM image (a) of a multilayer from a pyrrole and Bi(III), Te(IV) containing electrolyte and the corresponding close-up (b).

7 Conclusion

In light of the lack of comprehensive thermoelectric characterization methods, in particular for deposited samples, considerable effort was made first to develop measurement methods. The microdevices finally obtained after some iterations were shown by numerical studies and experimentally to allow accurate thermoelectric characterization.

The devices were first applied to measurements on uniform samples. Deviations from literature values in case of bismuth telluride could be ascribed to doping and grain boundary scattering. Also in case of a bismuth rich deposit transition to p-type conduction was demonstrated, which has not been reported so far in case of electrodeposited material.

Finally first attempts at fabricating and characterizing nanostructured samples were made. Some improvement of the thermopower was observed in a thin supported film, whose thermoelectric properties can still be partially measured, namely thermopower and electrical resistivity. Also multilayered samples consisting of alternating layers of bismuth rich bismuth telluride and tellurium were obtained by modulating the deposition potential. These samples have in common an enhanced temperature dependence of the Seebeck coefficient indicating a modulation of the band structure. The figure of merit in some cases exceeds the one of as-deposited bulk samples by a factor of 4, but falls short compared to annealed samples.

It was demonstrated analytically that greater enhancement of thermoelectric properties can be achieved in superlattices with large band offsets, which, if broken-gap superlattices are to be avoided, requires a large band gap barrier material. To avoid excessive band bending additionally approximately matching work functions are desirable. Bismuth

telluride - polypyrrole multilayers are expected to meet these requirements. Therefore first multilayers of this kind were deposited facilitated by the charge transfer mediator hydroquinone. Unfortunately thermoelectric characterizations of these samples could not yet be performed.

While the possibility of bismuth telluride / polypyrrole multilayer deposition from the same electrolyte was demonstrated, the problems of precipitation and rough deposits remain. The latter is likely associated not only with the observed precipitation but the the use of hydroquinone as charge mediator. Further studies could examine other charge mediators and the influence of pyrrole purification by distillation prior to deposition. Refining the method could allow fabrication of truly nanoscale multilayers for which interesting and improved thermoelectric properties are expected.

The developed micro-bridge devices are the first to allow for comprehensive, accurate and transfer-free thermoelectric characterization of deposited samples and thus represent the ideal platform for further thermoelectric materials research.

8 References

[1] Tritt TM, Kanatzidis MG, editors. Thermoelectric Materials - New Directions and Approches. vol. 478; 1997. Available from: https://www.osti.gov/biblio/20014234.

[2] Beretta D, Bruno P, Lanzani G, Caironi M. Reliable measurement of the Seebeck coefficient of organic and inorganic materials between 260 K and 460 K. Review of Scientific Instruments. 2015;86(7). Available from: http://dx.doi.org/10.1063/1.4926885.

[3] Kim C, Baek JY, Lopez DH, Kim DH, Kim H. Decoupling effect of electrical and thermal properties of Bi2Te3-polypyrrole hybrid material causing remarkable enhancement in thermoelectric performance. Journal of Industrial and Engineering Chemistry. 2019;71:119-26. Available from: https://doi.org/10.1016/j.jiec.2018.11.013.

[4] Chen G. Nanoscale Energy Transport and Conversion. Oxford University Press; 2005. Available from: https://global.oup.com/academic/product/nanoscale-energy-transport-and-conversion-9780195159424?cc=us&lang=en&.

[5] Goldsmid HJ. Introduction to Thermoelectricity; 2010. Available from: http://dx.doi.org/10.1007/978-3-642-00716-3.

[6] Callaway J. Model for Lattice Thermal Conductivity at Low Temperatures. Physical Review. 1958;113(4). Available from: https://doi.org/10.1103/PhysRev.113.1046.

[7] Morelli DT, Heremans JP, Slack GA. Estimation of the isotope effect on the lattice thermal conductivity of group IV and group III-V semiconductors. Physical Review B - Condensed Matter and Materials Physics. 2002;66(19):1953041-9. Available from: https://doi.org/10.1103/PhysRevB.66.195304.

[8] Muñoz Rojo M, Abad B, Manzano CV, Torres P, Cartoixà X, Alvarez FX, et al. Thermal conductivity of Bi_2Te_3 nanowires: how size affects phonon scattering. Nanoscale. 2017;9(20):6741-7. Available from: http://xlink.rsc.org/?DOI=C7NR02173A.

[9] Hellman O, Broido Da. Phonon thermal transport in Bi_2Te_3 from first principles. Physical Review B. 2014;90(13):134309. Available from: https://link.aps.org/doi/10.1103/PhysRevB.90.134309.

[10] Mavrokefalos A, Moore AL, Pettes MT, Shi L, Wang W, Li X. Thermoelectric and structural characterizations of individual electrodeposited bismuth telluride nanowires. Journal of Applied Physics. 2009;105(10). Available from: https://doi.org/10.1063/1.3133145.

[11] Damodara Das V, Soundararajan N. Size and temperature effects on the thermoelectric power and electrical resistivity of bismuth telluride thin films. Physical Review B. 1988;37(9):4552-9. Available from: https://doi.org/10.1103/PhysRevB.37.4552.

[12] Pettes MT, Maassen J, Jo I, Lundstrom MS, Shi L. Effects of surface band bending and scattering on thermoelectric transport in suspended bismuth telluride nanoplates. Nano Letters. 2013;13(11):5316-22. Available from: http://dx.doi.org/10.1021/nl402828s.

[13] Hicks LD, Dresselhaus MS. Effect of quantum-well structures on the thermoelectric figure of merit. Physical Review B. 1993;47(19):12727-31. Available from: https://doi.org/10.1103/PhysRevB.47.12727.

[14] Chen G. Size and interface effects on thermal conductivity of superlattices and periodic thin-film structures. Journal of Heat Transfer. 1997;119(2):220-9. Available from: https://doi.org/10.1115/1.2824212.

[15] Gayner C, Kar KK. Recent advances in thermoelectric materials. Progress in Materials Science. 2016;83:330-82. Available from: http://dx.doi.org/10.1016/j.pmatsci.2016.07.002.

[16] Martín-González M, Caballero-Calero O, Díaz-Chao P. Nanoengineering thermoelectrics for 21st century: Energy harvesting and other trends in the field. Renewable and Sustainable Energy Reviews. 2013;24:288-305. Available from: https://doi.org/10.1016/j.rser.2013.03.008.

[17] Heremans JP, Wiendlocha B, Chamoire AM. Resonant levels in bulk thermoelectric semiconductors. Energy and Environmental Science. 2012;5(2):5510-30. Available from: https://doi.org/10.1039/C1EE02612G.

[18] Kim J, Bahk JH, Hwang J, Kim H, Park H, Kim W. Thermoelectricity in semiconductor nanowires. Physica Status Solidi - Rapid Research Letters. 2013;7(10):767-80. Available from: https://doi.org/10.1002/pssr.201307239.

[19] Bergman DJ, Levy O. Thermoelectric properties of a composite medium. Journal of Applied Physics. 1991;70(11):6821-33. Available from: https://doi.org/10.1063/1.349830.

[20] Zou J, Balandin A. Phonon heat conduction in a semiconductor nanowire. Journal of Applied Physics. 2001;89(5):2932-8. Available from: https://doi.org/10.1063/1.1345515.

[21] Wagner MFP, Völklein F, Reith H, Trautmann C, Toimil-Molares ME. Fabrication and thermoelectrical characterization of three-dimensional nanowire networks. Physica Status Solidi (A) Applications and Materials Science. 2016;213(3):610-9. Available from: https://doi.org/10.1002/pssa.201532616.

[22] Rauber M, Alber I, Müller S, Neumann R, Picht O, Roth C, et al. Highly-ordered supportless three-dimensional nanowire networks with tunable complexity and interwire

connectivity for device integration. Nano Letters. 2011;11(6):2304-10. Available from: https://doi.org/10.1021/nl2005516.

[23] Li X, Koukharenko E, Nandhakumar IS, Tudor J, Beeby SP, White NM. High density p-type Bi0.5Sb1.5Te3 nanowires by electrochemical templating through ion-track lithography. Physical chemistry chemical physics : PCCP. 2009;11(18):3584-90. Available from: https://doi.org/10.1039/b818040g.

[24] Reeves RD, Crosser LA, Chester GE, Hill JJ. Thermoelectric property enhancement via pore confinement in template grown bismuth telluride nanowire arrays. Nanotechnology. 2017;28(50). Available from: https://doi.org/10.1088/1361-6528/aa9733.

[25] Jin S, Ziabari A, Koh YR, Saei M, Wang X, Deng B, et al. Enhanced thermoelectric performance of p-type $Bi_xSb_{2-x}Te_3$ nanowires with pulsed laser assisted electrochemical deposition. Extreme Mechanics Letters. 2016;9:386-96. Available from: http://dx.doi.org/10.1016/j.eml.2016.04.010.

[26] Cao YQ, Zhu TJ, Zhao XB, Zhang XB, Tu JP. Nanostructuring and improved performance of ternary Bi-Sb-Te thermoelectric materials. Applied Physics A: Materials Science and Processing. 2008;92(2):321-4. Available from: https://doi.org/10.1007/s00339-008-4518-y.

[27] Zhang G, Kirk B, Jauregui LA, Yang H, Xu X, Chen YP, et al. Rational Synthesis of Ultrathin n-Type Bi_2Te_3 Nanowires with Enhanced Thermoelectric Properties. Nano Letters. 2012;12(1):56-60. Available from: http://pubs.acs.org/doi/10.1021/nl202935k.

[28] See KC, Feser JP, Chen CE, Majumdar A, Urban JJ, Segalman Ra. Water-processable polymer-nanocrystal hybrids for thermoelectrics. Nano Letters. 2010;10(11):4664-7. Available from: https://doi.org/10.1021/nl102880k.

[29] Burton MR, Richardson SJ, Staniec PA, Terrill NJ, Elliott JM, Squires AM, et al. A novel route to nanostructured bismuth telluride films by electrodeposition. Electrochemistry Communications. 2017;76:71-4. Available from: http://dx.doi.org/10.1016/j.elecom.2017.02.004.

[30] Wu M, Ramírez SA, Shafahian E, Guo L, Glorieux C, Binnemans K, et al. Electrodeposition of bismuth telluride thin films containing silica nanoparticles for thermoelectric applications. Electrochimica Acta. 2017;253:554-62. Available from: https://doi.org/10.1016/j.electacta.2017.09.012.

[31] Simkin MV, Mahan GD. Minimum Thermal Conductivity of Superlattices. Physical Review Letters. 2000;84(5):927-30. Available from: https://doi.org/10.1103/PhysRevLett.84.927.

[32] Daly BC, Maris HJ, Imamura K, Tamura S. Molecular dynamics calculation of the thermal conductivity of superlattices. Physical Review B - Condensed Matter and Materials Physics. 2002;66(2):243011-7. Available from: https://doi.org/10.1103/PhysRevB.66.024301.

[33] Hinsche NF, Yavorsky BY, Gradhand M, Czerner M, Winkler M, König J, et al. Thermoelectric transport in Bi_2Te_3/Sb_2Te_3 superlattices. Physical Review B - Condensed Matter and Materials Physics. 2012;86(8):1-13. Available from: https://doi.org/10.1103/PhysRevB.86.085323.

[34] Winkler M, Liu X, Schürmann U, König JD, Kienle L, Bensch W, et al. Current status in fabrication, structural and transport property characterization, and theoretical understanding of Bi2Te3 / Sb2Te3 superlattice systems. Zeitschrift fur Anorganische und Allgemeine Chemie. 2012;638(15):2441-54. Available from: https://doi.org/10.1002/zaac.201200305.

[35] Wu M, Binnemans K, Fransaer J. Electrodeposition of antimony from chloride-free ethylene glycol solutions and fabrication of thermoelectric $Bi_2Te_3/(Bi_{1-x}Sb_x)_2Te_3$ multilayers using pulsed potential electrodeposition. Electrochimica Acta. 2014;147:451-9. Available from: http://dx.doi.org/10.1016/j.electacta.2014.08.111.

[36] Xue FH, Fei GT, Wu B, Gui P, Zhang LD. Direct electrodeposition of highly dense Bi/Sb superlattice nanowire arrays. Journal of the American Chemical Society. 2005;127(44):15348-9. Available from: https://doi.org/10.1021/ja0547073.

[37] Yoo B, Xiao F, Bozhilov KN, Herman J, Ryan MA, Myung NV. Electrodeposition of thermoelectric superlattice nanowires. Advanced Materials. 2007;19(2):296-9. Available from: https://doi.org/10.1002/adma.200600606.

[38] Li S, Soliman HMA, Zhou J, Toprak MS, Muhammed M, Platzek D, et al. Effects of Annealing and Doping on Nanostructured Bismuth Telluride Thick Films. Chemistry of Materials. 2008;(2):4403-10. Available from: https://doi.org/10.1021/cm800696h.

[39] Trung NH, Sakamoto K, Toan NV, Ono T. Synthesis and evaluation of thick films of electrochemically deposited Bi_2Te_3 and Sb_2Te_3 thermoelectric materials. Materials. 2017;10(2). Available from: https://doi.org/10.3390/ma10020154.

[40] Takemori D, Okuhata M, Takashiri M. Thermoelectric Properties of Electrodeposited Bismuth Telluride Thin Films by Thermal Annealing and Homogeneous Electron Beam Irradiation. ECS Transactions. 2017;75(52):123-31. Available from: https://doi.org/10.1149/07552.0123ECST.

[41] Schumacher C, Reinsberg KG, Akinsinde L, Zastrow S, Heiderich S, Toellner W, et al. Optimization of electrodeposited p-doped Sb_2Te_3 thermoelectric films by millisecond potentiostatic pulses. Advanced Energy Materials. 2012;2(3):345-52. Available from: https://doi.org/10.1002/aenm.201100585.

[42] Lee J, Farhangfar S, Lee J, Cagnon L, Scholz R, Gösele U, et al. Tuning the crystallinity of thermoelectric Bi_2Te_3 nanowire arrays grown by pulsed electrodeposition. Nanotechnology. 2008;19(36):365701. Available from: https://doi.org/10.1088/0957-4484/19/36/365701.

[43] Manzano CV, Rojas AA, Decepida M, Abad B, Feliz Y, Caballero-Calero O, et al. Thermoelectric properties of Bi_2Te_3 films by constant and pulsed electrodeposition. Journal of Solid State Electrochemistry. 2013;17(7):2071-8. Available from: https://doi.org/10.1007/s10008-013-2066-7.

[44] Harman TC, Walsh MP, Laforge BE, Turner GW. Nanostructured Thermoelectric Materials. Journal of Electronic Materials. 2005;34(5):L19. Available from: https://doi.org/10.1007/s11664-005-0083-8.

[45] Harman TC, Taylor PJ, Spears DL, Walsh MP. Thermoelectric Quantum-Dot Superlattices with High ZT T.C. Journal of Electronic Materials. 2000;29(1):1-4. Available from: https://doi.org/10.1007/s11664-000-0117-1.

[46] Venkatasubramanian R, Siivola E, Colpitts T, O'Quinn B. Thin-film thermoelectric devices with high room-temperature figures of merit. Nature. 2001;413(6856):597-602. Available from: https://doi.org/10.1038/35098012.

[47] Manzano CV, Abad B, Muñoz Rojo M, Koh YR, Hodson SL, Lopez Martinez AM, et al. Anisotropic Effects on the Thermoelectric Properties of Highly Oriented Electrodeposited Bi_2Te_3 Films. Scientific Reports. 2016;6(1):19129. Available from: http://www.nature.com/articles/srep19129.

[48] Wight NM, Acosta E, Vijayaraghavan RK, McNally PJ, Smirnov V, Bennett NS. A universal method for thermal conductivity measurements on micro-/nano-films with and without substrates using micro-Raman spectroscopy. Thermal Science and Engineering Progress. 2017;3:95-101. Available from: http://dx.doi.org/10.1016/j.tsep.2017.06.009.

[49] Cahill DG, Pohl RO. Thermal conductivity of amorphous solids above the plateau. Physical Review B. 1987;35(8):4067-73. Available from: https://doi.org/10.1103/PhysRevB.35.4067.

[50] Cahill DG. Thermal conductivity measurement from 30 to 750 K: The 3ω method. Review of Scientific Instruments. 1990;61(2):802-8. Available from: https://doi.org/10.1063/1.1141498.

[51] Li D, Li L, Liu DW, Li JF. Temperature dependence of the Raman spectra of Bi 2Te 3 and Bi 0.5Sb 1.5Te 3 thermoelectric films. Physica Status Solidi - Rapid Research Letters. 2012;6(6):268-70. Available from: https://doi.org/10.1002/pssr.201206149.

[52] Kim P, Shi L, Majumdar A, McEuen PL. Thermal transport measurements of individual multiwalled nanotubes. Physical Review Letters. 2001;87(21):215502-12155024. Available from: https://doi.org/10.1103/PhysRevLett.87.215502.

[53] Mavrokefalos A, Pettes MT, Zhou F, Shi L. Four-probe measurements of the in-plane thermoelectric properties of nanofilms. Review of Scientific Instruments. 2007;78(3):1-6. Available from: https://doi.org/10.1063/1.2712894.

[54] Seol JH, Moore AL, Shi L, Jo I, Yao Z. Thermal conductivity measurement of graphene exfoliated on silicon dioxide. Journal of Heat Transfer. 2011;133(2):1-7. Available from: https://doi.org/10.1021/nl304060g.

[55] Shi L, Li D, Yu C, Jang W, Kim D, Yao Z, et al. Measuring thermal and thermoelectric properties of one-dimensional nanostructures using a microfabricated device. Journal of Heat Transfer. 2003;125(5):881-8. Available from: https://doi.org/10.1115/1.1597619.

[56] Barati V, Garcia Fernandez J, Geishendorf K, Schnatmann LU, Lammel M, Kunzmann A, et al. Thermoelectric Characterization Platform for Electrochemically Deposited Materials. Advanced Electronic Materials. 2020;1901288:1-8. Available from: https://doi.org/10.1002/aelm.201901288.

[57] Völklein F, Reith H, Cornelius TW, Rauber M, Neumann R. The experimental investigation of thermal conductivity and the Wiedemann-Franz law for single metallic nanowires. Nanotechnology. 2009;20(32):0-8. Available from: http://stacks.iop.org/Nano/20/325706.

[58] Karg S, Mensch P, Gotsmann B, Schmid H, Kanungo PD, Ghoneim H, et al. Measurement of thermoelectric properties of single semiconductor nanowires. Journal of Electronic Materials. 2013;42(7):2409-14. Available from: http://dx.doi.org/10.1007/s11664-012-2409-7.

[59] Shikida M, Sato K, Tokoro K, Uchikawa D. Differences in anisotropic etching properties of KOH and TMAH solutions. Sensors and Actuators, A: Physical. 2000;80(2):179-88. Available from: https://doi.org/10.1016/S0924-4247(99)00264-2.

[60] Biswas K, Kal S. Etch characteristics of KOH, TMAH and dual doped TMAH for bulk micromachining of silicon. Microelectronics Journal. 2006;37(6):519-25. Available from: https://doi.org/10.1016/j.mejo.2005.07.012.

[61] Seidel H, Csepregi L, Heuberger A, Baumgärtel H. Anisotropic Etching of Crystalline Silicon in Alkaline Solutions: I. Influence of Dopants. Journal of The Electrochemical Society. 1990;137(11):3626-32. Available from: https://doi.org/10.1149/1.2086278.

[62] Martín-González MS, Prieto AL, Gronsky R, Sands T, Stacy AM. Insights into the Electrodeposition of Bi_2Te_3. Journal of The Electrochemical Society. 2002;149(11):C546. Available from: https://doi.org/10.1149/1.1509459.

[63] Sandnes E, Williams ME, Bertocci U, Vaudin MD, Stafford GR. Electrodeposition of bismuth from nitric acid electrolyte. Electrochimica Acta. 2007;52(21):6221-8. Available from: http://dx.doi.org/10.1016/j.electacta.2007.04.002.

[64] Baudrand D. Nickel Sulfamate Plating, Its Mystique and Practicality. Metal Finishing. 1996:1996. Available from: https://doi.org/10.1016/0026-0576(96)81353-5.

[65] Bos JWG, Zandbergen HW, Lee M, Ong NP, Cava RJ. Structures and thermoelectric properties of the infinitely adaptive series $(Bi_2)_m(Bi_2Te_3)_n$. Physical Review B. 2007:1-9. Available from: https://doi.org/10.1103/PhysRevB.75.195203.

[66] Augustin A, Rajendra Udupa K, Udaya Bhat K. Crystallite size measurement and micro-strain analysis of electrodeposited copper thin film using Williamson-Hall method. AIP Conference Proceedings. 2016;1728(May). Available from: https://doi.org/10.1063/1.4946543.

[67] Pelleg J, Elish E, Mogilyanski D. Evaluation of average domain size and microstrain in a silicide film by the Williamson-Hall method. Metallurgical and Materials Transactions A: Physical Metallurgy and Materials Science. 2005;36(11):3187-94. Available from: https://doi.org/10.1007/s11661-005-0089-0.

[68] Takashiri M, Miyazaki K, Tanaka S, Kurosaki J, Nagai D, Tsukamoto H. Effect of grain size on thermoelectric properties of n -type nanocrystalline bismuth-telluride based thin films. Journal of Applied Physics. 2008;104(8). Available from: http://dx.doi.org/10.1063/1.2990774.

[69] Harman TC, Cahn JH, Logan MJ. Measurement of thermal conductivity by utilization of the peltier effect. Journal of Applied Physics. 1959;30(9):1351-9. Available from: https://doi.org/10.1063/1.1735334.

[70] Rojo MM, Manzano CV, Granados D, Osorio MR, Borca-Tasciuc T, Martín-González M. High electrical conductivity in out of plane direction of electrodeposited Bi_2Te_3 films. AIP Advances. 2015;5(8). Available from: http://dx.doi.org/10.1063/1.4928863.

[71] Kim Y, Cho S, DiVenere A, Wong GKL, Ketterson JB. Composition-dependent layered structure and transport properties in BiTe thin films. Physical Review B - Condensed Matter and Materials Physics. 2001;63(15):3-7. Available from: https://doi.org/10.1103/PhysRevB.63.155306.

[72] Cusack N, Kendall P. The absolute scale of thermoelectric power at high temperature. Proceedings of the Physical Society. 1958;72(5):898-901. Available from: https://doi.org/10.1088/0370-1328/72/5/429.

[73] Laubitz MJ. Transport properties of pure metals at high temperatures. II. Silver and gold. Canadian Journal of Physics. 1969;47(23):2633-44. Available from: https://doi.org/10.1139/p69-322.

[74] Mishra H, Cola BA, Rawat V, Amama PB, Biswas KG, Xu X, et al. Thermomechanical and thermal contact characteristics of bismuth telluride films electrodeposited on carbon nanotube arrays. Advanced Materials. 2009;21(42):4280-3. Available from: http://dx.doi.org/10.1002/adma.200803705.

[75] Käding OW, Skurk H, Goodson KE. Thermal conduction in metallized silicon-dioxide layers on silicon. Applied Physics Letters. 1994;65(13):1629-31. Available from: http://dx.doi.org/10.1063/1.112933.

[76] Gu H, Wang J, Wei X, Wang H, Li Z. Thermal conductivity and interfacial thermal resistance in the heterostructure of silicon/amorphous silicon dioxide: The strain and temperature effect. Nanotechnology. 2020;31(50):0-12. Available from: http://dx.doi.org/10.1088/1361-6528/abb504.

[77] Sharma PA, Brumbach M, Adams DP, Ihlefeld JF, Lima-Sharma AL, Chou S, et al. Electrical contact uniformity and surface oxidation of ternary chalcogenide alloys. AIP Advances. 2019;9(1). Available from: http://dx.doi.org/10.1063/1.5081818.

[78] Gallo CF, Chandrasekhar BS, Sutter PH. Transport properties of bismuth single crystals. Journal of Applied Physics. 1963;34(1):144-52. Available from: https://doi.org/10.1063/1.1729056.

[79] Powell RW, Tye RP, Hickman MJ. The thermal conductivity of nickel. International Journal of Heat and Mass Transfer. 1965;8(5):679-88. Available from: http://dx.doi.org/10.1016/0017-9310(65)90017-7.

[80] Green TA. Gold etching for microfabrication. Gold Bulletin. 2014;47(3):205-16. Available from: http://dx.doi.org/10.1007/s13404-014-0143-z.

[81] Shaughnessy MC, Bartelt NC, Zimmerman JA, Sugar JD. Energetics and diffusion of gold in bismuth telluride-based thermoelectric compounds. Journal of Applied Physics. 2014;115(6). Available from: https://doi.org/10.1063/1.4865735.

[82] Bejenari I, Kantser V. Thermoelectric properties of bismuth telluride nanowires in the constant relaxation-time approximation. Physical Review B - Condensed Matter and Materials Physics. 2008;78(11):1-12. Available from: https://doi.org/10.1103/PhysRevB.78.115322.

[83] Champness CH, Kipling AL. The Hall and Seebeck effects in nonstochiometric bismuth telluride. Canadian Journal of Physics. 1965;44:769-88. Available from: https://doi.org/10.1139/p66-066.

[84] Rowe DM, editor. CRC Handbook of Thermoelectrics. CRC Press LLC; 1995. Available from: https://www.routledge.com/CRC-Handbook-of-Thermoelectrics/Rowe/p/book/9780849301469.

[85] Kaibe H, Tanaka Y, Sakata M, Nishida I. Anisotropic galvanomagnetic and thermoelectric properties of n-type Bi_2Te_3 single crystal with the composition of a useful thermoelectric cooling material. Journal of Physics and Chemistry of Solids. 1989;50(9):945-50. Available from: https://doi.org/10.1016/0022-3697(89)90045-0.

[86] Goldsmid HJ. The thermal conductivity of bismuth telluride. Proceedings of the Physical Society Section B. 1956;69(2):203-9. Available from: http://dx.doi.org/10.1088/0370-1301/69/2/310.

[87] Goldsmid HJ. Recent studies of bismuth telluride and its alloys. Journal of Applied Physics. 1961;32(10):2198-202. Available from: http://dx.doi.org/10.1063/1.1777042.

[88] Satterthwaite CB, Ure RW. Electrical and Thermal Properties of Bi_2Te_3. Physical Review. 1957;108(5):1164-70. Available from: https://doi.org/10.1103/PhysRev.108.1164.

[89] Al-Alam P, Pernot G, Isaiev M, Lacroix D, De Vos M, Stein N, et al. Lattice thermal conductivity of Bi_2Te_3 and SnSe using Debye-Callaway and Monte Carlo phonon transport modeling: Application to nanofilms and nanowires. Physical Review B. 2019;100(11):1-16. Available from: http://dx.doi.org/10.1103/PhysRevB.100.115304.

[90] Liu Y, Chen J, Deng H, Hu G, Zhu D, Dai N. Anomalous thermoelectricity in strained Bi_2Te_3 films. Scientific Reports. 2016;6(September):2-8. Available from: https://doi.org/10.1038/srep32661.

[91] Fleurial JP, Gailliard L, Triboulet R, Scherrer H, Scherrer S. Thermal properties of high quality single crystals of bismuth telluride-Part I: Experimental characterization. Journal of Physics and Chemistry of Solids. 1988;49(10):1237-47. Available from: https://doi.org/10.1016/0022-3697(88)90182-5.

[92] Hutchison R, Zhao YJ, Delley B, Freeman J, Ratner A, Marks J. Electronic structure of conducting polymers: Limitations of oligomer extrapolation approximations and effects of heteroatoms. Physical Review B - Condensed Matter and Materials Physics. 2003;68(11):1-13. Available from: https://doi.org/10.1103/PhysRevB.68.035204.

[93] Asavapiriyanont S, Chandler GK, Gunawardena GA, Pletcher D. The electrodeposition of polypyrrole films from aqueous solutions. Journal of Electroanalytical Chemistry. 1984;177(1-2):229-44. Available from: https://doi.org/10.1016/0022-0728(84)80225-9.

[94] Waltman RJ, Bargon J. Electrically conducting polymers: A review of the electropolymerization reaction, of the effects of chemical structure on polymer film

properties, and of applications towards technology. Canadian Journal of Chemistry. 1986;64(1):76-95. Available from: https://doi.org/10.1139/v86-015.

[95] Levine KL, Tallman DE, Bierwagen GP. The mediated electrodeposition of poly pyrrole on aluminium alloy. Australian Journal of Chemistry. 2005;58(4):294-301. Available from: https://doi.org/10.1071/CH04289.

[96] Nematollahi D, Hesari H, Salehzadeh H, Hesari M, Momeni S. Electrochemical synthesis of new organic compounds based on the oxidation of 1,4-dihydroxybenzene derivatives in the presence of primary and secondary amines. Comptes Rendus Chimie. 2016;19(3):357-62. Available from: http://dx.doi.org/10.1016/j.crci.2015.11.003.

David Osenberg

Resumé

Education

2018–2023 **Ph.D. Thesis in Materials Science and Engineering**, *EPFL*
Ph.D. Thesis: "Investigation of thermoeletric nanomaterials"

2013–2016 **Master of Science in Micro- and Nanosystems**, *ETH Zurich*
Master Thesis: "Thermal transport in suspended graphene monolayers"

2010–2015 **Bachelor of Science in Physics**, *ETH Zurich*
Bachelor Thesis: "On the development of sensors for scanning gate microscopy based on coaxial tips attached to quartz tuning forks"

2010 **Abitur**, *Theodor-Heuss-Gymnasium Radevormwald, Germany*
Major Subjects: Mathematics, English, Physics, Religious Education

Experience

2018–2023 **Ph.D. Student**, *Empa (Swiss Federal Laboratories for Materials Science and Technology), Thun*

- Electrodeposition of thermoelectric materials
- Design and Fabrication of microdevices for complete thermoelectric characterization of deposited materials, involving FEM modelling, mask design, physical vapor deposition, photolithography and wet etching
- Development of a LabVIEW script and a setup for thermoelectric measurements on the microdevices
- Data Analysis using Python for extraction of the thermeoelectric properties from the raw data
- Scanning Electron Microscopy (Hitachi S-4800 FE-SEM), X-ray diffraction (Bruker D8 Discover) and fluorescence measurements
- Design and fabrication of microdevices for four point probe measurements on 3D printed microstructures in collaboration with Exaddon AG

2016–2017 **Intern**, *R&D Department of Levitronix GmbH in Zurich*

- Creation of Python based scripts for statistical evaluation of ultrasonic flow meter data
- Performing Fluid FEM simulations and comparison with measurement data
- Development and validation of a model for the dependence of the measured waveforms on the piezo-impedance

2015–2016 **Design and Fabrication of MEMS**, *Binnig and Rohrer Nanotechnology Center, Rüschlikon*

- Photoresist processing, physical vapor deposition, patterning of CVD grown graphene, wire bonding in the clean rooms of the institute
- Scanning Electron Microscopy and Micro-Raman spectroscopy
- Conducting cryostat measurements

2013 **Fabrication and Characterisation of quartz tuning fork based Atomic Force Sensors**, *ETH Zurich*

- Epoxy bonding, soldering of the tuning forks, electrochemical etching of tips
- Frequency response analysis, obtaining and evaluating AFM-scans of a test microstructure

Publications

[1] D. Osenberg, C. V. Manzano, M. Martín-González, N. Stein, M. De Vos, S. Mischler, D. Lacroix, G. Pernot, and L. Philippe, "Development of microdevices for the in-plane thermoelectric characterization of deposited films," *Journal of Materials Research and Technology*, vol. 15, pp. 1190–1200, 2021. [Online]. Available: https://doi.org/10.1016/j.jmrt.2021.08.109

[2] P. Al-Alam, G. Pernot, M. Isaiev, D. Lacroix, M. De Vos, N. Stein, D. Osenberg, and L. Philippe, "Lattice thermal conductivity of Bi2Te3 and SnSe using Debye-Callaway and Monte Carlo phonon transport modeling: Application to nanofilms and nanowires," *Physical Review B*, vol. 100, no. 11, pp. 1–16, 2019. [Online]. Available: http://dx.doi.org/10.1103/PhysRevB.100.115304

[3] S. N. Raja, D. Osenberg, K. Choi, H. G. Park, and D. Poulikakos, "Annealing and polycrystallinity effects on the thermal conductivity of supported CVD graphene monolayers," *Nanoscale*, vol. 9, no. 40, pp. 15 515–15 524, 2017. [Online]. Available: https://doi.org/10.1039/C7NR05346K